

位元交錯調變碼之效能分析

研究生：黃亮維

指導教授：沈文和 博士

國立交通大學
電信工程學系碩士班

摘 要

位元交錯調變碼 (BICM) 保有籬笆碼之有效利用頻寬之特性，並擁有更多的分集階數，所以廣泛的應用在瑞雷衰退通道中，在本篇論文中，我們推導了位元交錯調變碼在加成性白色高斯雜訊通道與瑞雷衰退通道的系統效能分析，我們同時考慮了軟式與硬式解碼器。有鑑於灰色編碼的 QAM 調變在位元交錯調變碼擁有最佳的系統效能，我們特別針對它應用在位元交錯調變碼使用隨機標籤位址 (BICM-RLP) 與位元交錯調變碼使用固定標籤位址 (BICM-FLP) 這兩種架構提出一個更精準的分析。在使用軟式解碼器的 BICM-RLP 架構中，我們的分析比前人的精準，另一方面，BICM-FLP 的架構則是全新的分析。

Tight Performance Upper Bounds for Bit Interleaved Coded QAM Modulation with Gray Labeling

Student : Liang-Wei Huang

Advisor : Dr. Wern-Ho Sheen

Institute of Communication Engineering
National Chiao Tung University

Abstract

Bit-interleaved coded modulation (BICM) is a bandwidth-efficient scheme with a *diversity order* higher than the Ungerboeck's trellis-coded modulation over fading channels. In this thesis, we investigate the performance of punctured BICM with soft and hard decoding over additive white Gaussian and Rayleigh fading channels. Tight BER upper bounds are derived for QAM constellation with gray labeling, which is known to have the best performance and constitutes a large portion of the practical applications of BICM systems. Both BICM with random (BICM-RLP) and fixed label position (BICM-FLP) mapping are analyzed. For BICM-RLP with soft decoding, the new upper bound is tighter than the well-known BICM Union and the Expurgated Bound proposed in [4]. The tight upper bounds for hard decision and for BICM-FLP with soft decision are newly derived results.

Index Terms—Bit-interleaved coded modulation (BICM), gray labeling, punctured convolutional code, BER upper bounds, Rayleigh fading channels.

致 謝

本篇論文得以順利完成，首先要特別感謝我的指導教授 沈文和博士，在大四下學期與兩年研究所過程中給予的指導與建議，並教導我進行研究的方法與態度，使我培養獨立研究的能力，沈文和教授的諄諄教誨帶給我對人生的態度及研究精神上相當大的影響。在本篇論文中的許多觀念及推導方式都深深地受到沈教授嚴謹的態度所影響，而使得研究的工作能夠順利地進行。

特別感謝眾多學長與我討論論文的撰寫方向與推導數學的符號及架構對論文提出的建議與修改。亦感謝張家瑋同學頻繁討論、共同驗證模擬平台。此外，我要感謝無線寬頻接取系統實驗室的許正欣博士，博士班學長何建興、李奇芳及傅宜康，碩士班學長游曜駿、方凱易、林敏裕及賴信良，還有同學陳長新，大家在這兩年研究生活中，所給予鼓勵與幫忙，經由不斷的討論與經驗分享使我在專業知識有更多的了解，特此誌謝。

其次，感謝實驗室的所有伙伴。在相處的兩年中，由於有大家的陪伴研究生生活更加充實。最後，感謝我的家人及女友。在求學的過程中，無論遭遇任何挫折你們總是給我最大的支持並陪伴我渡過難關，讓我克服種種困難，論文得以順利完成，特此致上萬分謝意。

民國九十三年六月

研究生黃亮維謹識於交通大學

Contents

摘要.....	i
Abstract.....	ii
誌謝.....	iii
Contents.....	iv
List of Tables.....	vi
List of Figures.....	vii
Chapter 1 Introduction.....	1
Chapter 2 System Model.....	4
2.1 Interleaving and Label-Position Mapping.....	5
2.2 QAM Constellation with Gray Labeling.....	6
2.3 Vector Channel Model.....	8
2.4 Decoding Rule.....	8
Chapter 3 Upper Bounds for BICM with Random Label-Position Mapping (BICM-RLP)....	10
3.1 BICM Union ($BICM_{UN}$) and Expurgated Bounds ($BICM_{EX}$).....	10
3.2 New Tighter Bound for QAM Constellation with Gray Labeling.....	12
3.3 Pair-wise Error Probability.....	19
3.3.1 Pair-wise Error Probability for Soft-decision in AWGN Channel.....	20
3.3.2 Pair-wise Error Probability with Soft-Decision in Rayleigh Fading Channels.....	22
3.4 Numerical Results.....	23
3.4.1 (2,1,6) Convolutional code.....	23
3.4.2 (2,1,2) Convolutional code.....	28
Chapter 4 Upper Bounds for BICM with Fixed Label-Position Mapping (BICM-FLP).....	32
4.1 Modified Error State Diagram and Transfer Function with no Puncturing.....	32
4.1.1 Modified Error State Diagram.....	32
4.1.2 Transfer Function.....	34
4.2 Modified Error State Diagram and Transfer Function with Puncturing.....	36
4.3 New Tighter Bound for QAM Constellation with Gray Labeling.....	42
4.3.1 Pairwise error probability with Soft-decision in AWGN channel...	42
4.3.2 Pair-wise Error Probability with Soft-decision in Rayleigh Fading Channels	43
4.4 Numerical Results.....	44
4.4.1 (2,1,6) Convolutional code.....	44
4.4.2 (2,1,2) Convolutional code.....	48
4.4.3 Comparison of BICM-RLP and BICM-FLP.....	52
Chapter 5 Conclusions.....	55

Appendix A	BER Upper Bounds for BICM with Hard Decision.....	56
A.	System model of BICM with hard decision.....	56
B.	Analytical model of BICM system with hard decision.....	56
C.	Decoding Rule.....	57
D.	Pairwise Error Probability of BICM-SI wit hard-decision.....	57
E.	Numerical Results.....	62
E.1	(2,1,6) Convolutional code.....	62
E.2	(2,1,2) Convolutional code.....	66
References.....		70



List of Tables

Table.1	Puncture pattern systems for $2/3$ -rate and $3/4$ -rate	5
Table.2	Puncture pattern for the $2/3$ -rate and $3/4$ -rate codes with 16-QAM	36
Table.3	Puncture pattern for the $2/3$ -rate and $3/4$ -rate codes with 64-QAM	39
Table.4	Coded bit error probabilities table of 16-QAM modulation.....	60
Table.5	Coded bit error probabilities table of 64-QAM modulation.....	61



List of Figures

Fig.1	A block diagram of general BICM systems.....	4
Fig.2	BICM with random label-position mapping (BICM-RLP).....	6
Fig.3	BICM with fixed label-position mapping. (BICM-FLP).....	6
Fig.4	16-QAM with Gray labeling.....	7
Fig.5	64-QAM with Gray labeling.....	7
Fig.6	Decision boundary of 16-QAM.....	15
Fig.7	Equivalent one dimensional signal set for 16-QAM.....	16
Fig.8	Equivalent one-dimensional signal set for 64-QAM.....	17
Fig.9	Performance of BICM-RLP in AWGN channels ($\kappa = 7, 16\text{QAM}$).....	24
Fig.10	Performance of BICM-RLP in Rayleigh fading channels ($\kappa = 7, 16\text{QAM}$)	25
Fig.11	Performance of BICM-RLP in AWGN channels ($\kappa = 7, 16, 64\text{QAM}$).....	26
Fig.12	Performance of BICM-RLP in Rayleigh fading channels ($\kappa = 7, 64\text{QAM}$).....	27
Fig.13	Performance of BICM-RLP in AWGN channels ($\kappa = 3, 16\text{QAM}$).....	28
Fig.14	Performance of BICM-RLP in Rayleigh fading channels ($\kappa = 3, 16\text{QAM}$)	29
Fig.15	Performance of BICM-RLP in AWGN channels ($k = 3, 16, 64\text{QAM}$).....	30
Fig.16	Performance of BICM-RLP in Rayleigh fading channels ($\kappa = 3, 16, 64\text{QAM}$).....	31
Fig.17	Modified error state diagram of (2,1,2), rate-1/2 code with 16-QAM	33
Fig.18	Modified error state diagram of (2,1,2), rate-2/3 punctured code with 16-QAM.....	37
Fig.19	Modified error state diagram of (2,1,2), rate-3/4 punctured code with 16-QAM.....	38
Fig.20	Modified error state diagram of (2,1,2), rate-1/2 code with 64-QAM	40
Fig.21	Modified error state diagram of (2,1,2), rate-2/3 punctured code with 64-QAM.....	41
Fig.22	Performance of BICM-FLP in AWGN channels ($\kappa = 7, 16\text{QAM}$).....	44
Fig.23	Performance of BICM-FLP in Rayleigh fading channels ($\kappa = 7, 16\text{QAM}$)	45
Fig.24	Performance of BICM-FLP in AWGN channels($\kappa = 7, 16, 64\text{QAM}$).....	46
Fig.25	Performance of BICM-FLP in Rayleigh fading channels ($\kappa = 7, 16, 64\text{QAM}$).....	47
Fig.26	Performance of BICM-FLP in AWGN channels ($\kappa = 3, 16\text{QAM}$).....	48
Fig.27	Performance of BICM-FLP in Rayleigh fading channels ($\kappa = 3, 16\text{QAM}$)	49
Fig.28	Performance of BICM-FLP in AWGN channels ($\kappa = 3, 16, 64 \text{QAM}$).....	50
Fig.29	Performance of BICM-FLP in Rayleigh fading channels ($\kappa = 3, 16, 64\text{QAM}$).....	51

Fig.30	Performance comparison between BICM-RLP and BICM-FLP systems in AWGN channels ($\kappa = 3, 7, 16$ QAM).....	52
Fig.31	Performance comparison between BICM-RLP and BICM-FLP systems in Rayleigh fading channels ($\kappa = 3, 16$ -QAM).....	53
Fig.32	Performance comparison between BICM-RLP and BICM-FLP systems in Rayleigh fading channels ($\kappa = 7, 16$ -QAM).....	54
Fig.33	A block diagram of general BICM systems with hard decoding.....	56
Fig.34	BICM with random label-position mapping with hard decoding.....	57
Fig.35	BICM with fixed label-position mapping with hard decoding.....	57
Fig.36	Performance of BICM-RLP with hard decoding in AWGN channels ($\kappa = 7, 16, 64$ QAM).....	62
Fig.37	Performance of BICM-RLP with hard decoding in Rayleigh fading channels ($\kappa = 7, 16, 64$ QAM).....	63
Fig.38	Performance of BICM-FLP with hard decoding in AWGN channels ($\kappa = 7, 16, 64$ QAM).....	64
Fig.39	Performance of BICM-FLP with hard decoding in Rayleigh fading channels ($\kappa = 7, 16, 64$ QAM).....	65
Fig.40	Performance of BICM-RLP with hard decoding in AWGN channels ($\kappa = 3, 16, 64$ QAM).....	66
Fig.41	Performance of BICM-RLP with hard decoding in Rayleigh fading channels ($\kappa = 3, 16, 64$ QAM).....	67
Fig.42	Performance of BICM-FLP with hard decoding in AWGN channels ($\kappa = 3, 16, 64$ QAM).....	68
Fig.43	Performance of BICM-FLP with hard decoding in Rayleigh fading channels ($\kappa = 3, 16, 64$ QAM).....	69

Chapter 1: Introduction

Trellis-coded modulation (TCM) was proposed by Ungerboeck for bandwidth-efficient communications in the additive white Gaussian noise (AWGN) channels [1]. Through a joint design of coding and high-order modulation, one can achieve a large coding gain without increasing the signal bandwidth. Originally, TCM was designed to maximize the minimum Euclidean distance of the coded systems in order to achieve a high coding gain. For fading channels, however, Divsalar and Simon showed that it is the *diversity order* rather than the minimum Euclidean distance that plays a key role in achieving such an objective [2]. Placing a symbol interleaver after modulator and/or using no parallel transitions are the conventional techniques to increase the diversity order [2]. Nevertheless, they may not be effective due to the fundamental limitation of diversity order to the minimum number of distinct coded symbols along any error event. Zehavi [3] later proposed to add a bit interleaver between channel encoder and modulator so that the diversity order can be increased to the minimum number of distinct *coded bits*, instead of the distinct *coded symbols*. This technique was named bit-interleaved coded modulation (BICM) in [4] and has been known to outperform TCM over fading channels with the same order of decoding complexity [3-6].

After Zehavi's pioneering work in [3], Caire, Taricco, and Biglieri laid a theoretical foundation for BICM from a viewpoint of information theory [4]; Along with new methods for performance analysis, design guidelines were given for efficient design of BICM with random label-position mapping (BICM-RLP). In [7-10], motivated by the concept of turbo decoding, BICM-RLP with iterative decoding was proposed to increase the system performance. Both soft and hard

feedbacks are possible in terms of complexity and performance tradeoffs. In [7, 11], by making the I and Q components of the transmitted signal being independently faded, the diversity order can be increased to twice of the diversity order of the conventional BICM-RLP with iterative decoding.

Most of the previous works on BER (Bit Error Rate) analysis of BICM are based on the BICM Union and Expurgated bounds proposed in [4]; for examples see [7, 12, 13]. Under the assumption of random label-position mapping and constellation symmetrization, a union upper bound, named BICM Union Bound, was derived in [4] for BICM-RLP for any signal constellation. Because this bound is too loose in general, a tighter *expurgated bound* was also obtained in [4] by expurgating the irrelevant error events in the BICM Union Bound. The expurgated bound is considered by the authors in [4] as an upper bound for QAM constellation with gray labeling but is only an approximation for others.

In this thesis, firstly a new tighter upper bound is proposed for BICM with QAM constellation and gray labeling, under the same assumption of random label-position mapping and constellation symmetrization as in [4]. Also, it will be shown that the BICM Expurgated Bound in [4] is actually only an approximation even for QAM constellation with gray labeling. Secondly, a new upper bound is proposed for BICM with fixed label-position mapping (BICM-FLP) [21,22]. BICM-FLP is one other popular form of BICM discussed in the literature. The proposed bound are very tight and applicable to any code rates if punctured convolutional codes is employed [14-16]. Only the QAM constellation with gray labeling will be explicitly treated in this thesis, although the principle leads to the new upper bounds can also be applied to other types of constellations. QAM constellation with gray labeling has the best performance and constitutes a very large portion of practical applications of BICM systems.

The rest of this thesis is organized as follows. Chapter 2 provides a brief overview of BICM, including MICM-RLP and BICM-FLP. We describe the BICM system model, includes interleaving, label-position mappings, channel model, and decoding rule. The proposed analysis methods with soft decoding will be shown in Chapter 3 and Chapter 4 for BICM-RLP and BICM-FLP, respectively. Extensive simulation and analytical results over AWGN and Rayleigh fading channel are also presented in these chapters. Conclusions are given in Chapter 5. Finally, new BER upper bounds for BICM systems with hard decoding are given in Appendix A.



Chapter 2: System Model

A block diagram of a general BICM system is shown in Fig.1. The BICM encoder is a serial concatenation of a (punctured) convolutional encoder C , a bit interleaver π , and a memory-less modulator, which is characterized by the mapping function u and an N -dimensional constellation χ . After encoding, the coded sequence \underline{c} is interleaved first, and a block of m -bits of the interleaved sequence $\pi(\underline{c})$ is mapped to one of $M = 2^m$ signals x in the N -dimensional constellation χ . The modulated signal sequence \underline{x} is then transmitted over the vector channel, characterized by the conditional pdf (probability density function) $p_{\theta}(\underline{y}|\underline{x})$, where \underline{y} is the received signal sequence. The receiver performs just the reverse operations of the transmitter: after demodulation and bit metric calculation, the received code sequence is de-interleaved and decoded, where \underline{L} is the bit metric sequence.

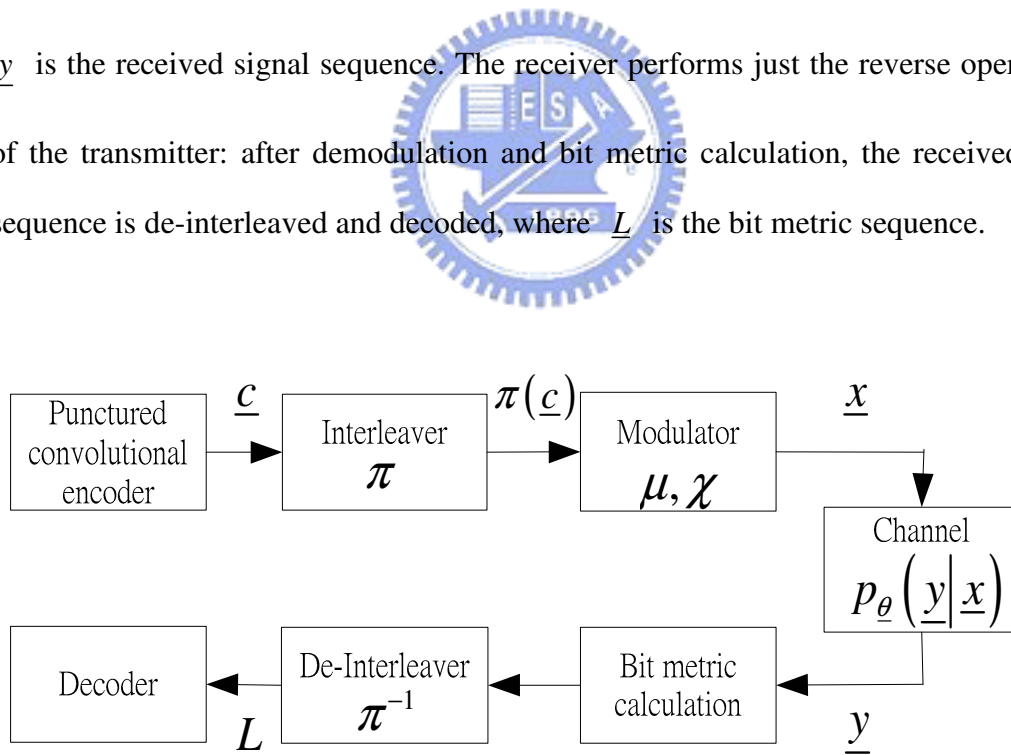


Fig.1 A block diagram of general BICM systems.

A high code rate system can be easily obtained by puncturing some of the coded bits of a low code rate system without increasing the decoding complexity. For example, 2/3-rate and 3/4-rate systems are obtained from a 1/2-rate system by using the puncture pattern, as shown in Table. 1. Both the punctured and un-punctured systems will be investigated.

Code rate	Puncture Pattern
1/2	$\begin{bmatrix} 1 \\ 1 \end{bmatrix}$
2/3	$\begin{bmatrix} 1 & 1 \\ 1 & \times \end{bmatrix}$
3/4	$\begin{bmatrix} 1 & 1 & \times \\ 1 & \times & 1 \end{bmatrix}$

Table.1 Puncture pattern systems for 2/3-rate and 3/4-rate

2.1 Interleaving and Label-Position Mapping

Depending on the design of interleaver, two types of label-position mapping have been discussed in the literature [3, 4, 21, 22]. The first one is *random mapping*, where a coded bit is randomly mapped to any position of the m -bit label of a constellation point [4]. The other is *fixed mapping* that the mapping between a coded bits and a label position follows a fixed pattern [3, 21,22]. For random mapping, the channel can be modeled as a parallel of m binary input channels, randomly selected by the input coded bit, as shown in Fig. 2. For fixed mapping, as is mentioned, the mapping between a coded bit and a label position is fixed, as shown in Fig. 3, where \underline{c}^i is to denote the sequence of coded bit that is mapped to the i^{th} label position of x . Both random and fixed label-position mapping are considered in this study.

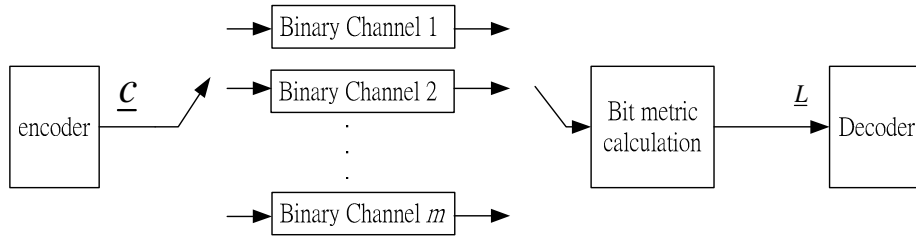


Fig.2 BICM with random label-position mapping (BICM-RLP) .

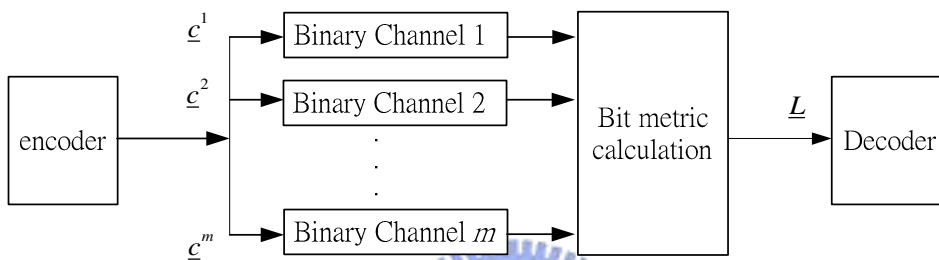


Fig.3 BICM with fixed label-position mapping. (BICM-FLP)

2.2 QAM Constellation with Gray Labeling

Only QAM constellation with gray labeling will be explicitly treated in this study, although the analysis may be extended to some other types of constellation and labeling. QAM constellation with gray labeling gives the best performance for BICM systems and constitutes a very large portion of practical applications of BICM systems. Figs. 4-5 show a gray labeling for 16 and 64 QAM constellations, respectively.

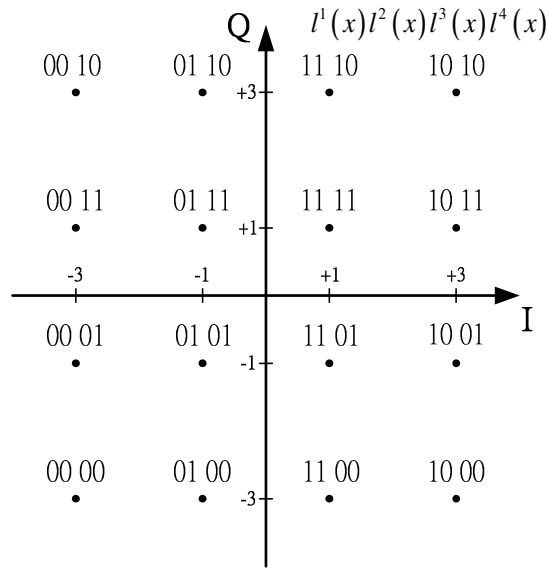


Fig.4 16-QAM with Gray labeling

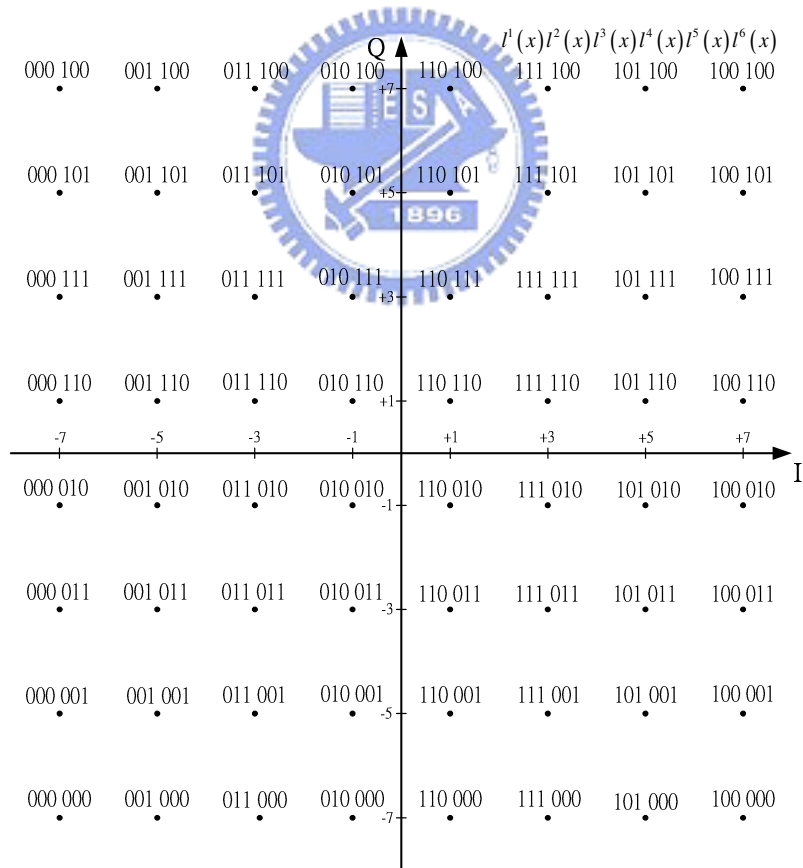


Fig.5 64-QAM w/ith Gray labeling

Note that I and Q may use different forms of gray labeling and that it may be different from those shown in Figs 4-5.

2.3 Vector Channel Model

The vector channel is characterized by the transition pdf,

$$p_{\theta}(y|x): \theta \in \mathbb{C}^{N'}; x, y \in \mathbb{C}^N. \quad (1)$$

where the complex-valued vector θ represents the channel parameter and is independent of the channel input x . Conditioned on the sequence $\underline{\theta}$, the channel is memory-less, i.e.,

$$p_{\underline{\theta}}(\underline{y}|\underline{x}) = \prod_k p_{\theta_k}(y_k|x_k). \quad (2)$$

θ is a constant for AWGN channel and is the multiplicative fading process for frequency nonselective slow-fading channels. For fading channels, assuming that the depth of interleaver is large enough so that $\{\theta_k\}$ are i.i.d. random variables. In addition, it will be assumed that perfect $\underline{\theta}$ is known to the receiver, hence we have ideal channel state information (CSI).

2.4 Decoding Rule [3, 4]

Let $l^i(x)$ denote the i th label bit of x , \mathcal{X}_b^i the subset of signals $x \in \mathcal{X}$ with $l^i(x) = b$, $b \in \{0,1\}$, and \bar{b} the complement of b . Recall that y is the channel output resulting from the transmission of x . From [3, 4], the optimum bit metric with ideal CSI for $l^i(x) = b$ at the time k is given by

$$L_k^i = \log \sum_{z \in \mathcal{X}_b^i} p_{\theta_k}(y_k|z) - \log \sum_{z \in \mathcal{X}_{\bar{b}}^i} p_{\theta_k}(y_k|z). \quad (3)$$

The branch metrics (3) may be computationally too complex for hardware implementation. Therefore, the simplified bit metric

$$\begin{aligned}
L_k^i &= \log \sum_{z \in \mathcal{X}_b^i} p_{\theta_k}(y_k|z) - \log \sum_{z \in \mathcal{X}_b^i} p_{\theta_k}(y_k|z) \\
&\approx \max_{z \in \mathcal{X}_b^i} p_{\theta_k}(y_k|z) - \max_{z \in \mathcal{X}_b^i} p_{\theta_k}(y_k|z) \\
&= -\min_{z \in \mathcal{X}_b^i} \|y_k - \theta_k z\|^2 + \min_{z \in \mathcal{X}_b^i} \|y_k - \theta_k z\|^2 \\
&\triangleq \tilde{L}_k^i
\end{aligned} \tag{4}$$

is often used in practical applications, in which only the largest term in each summation in (3) is selected for computation.

With the bit metric given in (4), the Viterbi algorithm can be employed to search through the code trellis to find the most likely one. The decoding procedure for the punctured systems is almost the same as the un-punctured one, except that a zero bit metric is assigned to the punctured bits.



Chapter 3: Upper Bounds for BICM with Random Label-Position Mapping (BICM-RLP)

The performance of BICM-RLP was first analyzed in [4]. Two BER upper bounds, that is, BICM Union and Expurgated Bound, were proposed. In this chapter, these bounds will be reviewed first, and then a new tighter bound is derived.

3.1 BICM Union (BICM_{UN}) and Expurgated Bounds (BICM_{EX}) [4]

Consider a (k, n) convolutional code, the union bound on BER is given by [4]

$$p_b \leq \frac{1}{k} \sum_{d=d_{\min}}^{\infty} W_l(d) f(d, u, \chi) \quad (5)$$

where $W_l(d)$ is the total weight of error events at Hamming distance d , d_{\min} the minimum Hamming distance of the code, and $f(d, u, \chi)$ the pair-wise error probability (PEP) with Hamming distance d . As is clear, $f(d, u, \chi)$ is also a function of the mapping u and constellation χ . Let d be the Hamming distance between the correct code sequence \underline{c} and error code sequence $\hat{\underline{c}}$. From [4], the PEP is given by

$$f(d, u, \chi) = E_{\underline{S}, \underline{U}} \left[P(\underline{c} \rightarrow \hat{\underline{c}}) \middle| \underline{S}, \underline{U} \right] \quad (6)$$

where $\underline{S} = (\dots, S_{-1}, S_0, S_1, \dots)$ and $\underline{U} = (\dots, U_{-1}, U_0, U_1, \dots)$ are the sequences of random variables to denote the operations of random label-position mapping and symmetrization of the use of the constellation, respectively. $S_k = i$, $i = 1, \dots, m$ denotes that the coded bit c_k is mapped to the i^{th} label position, $U_k = 1$ denotes that the mapping u is used for c_k , and $U_k = 0$, the complement mapping \bar{u} is used instead. S_k and U_k are assumed uniformly distributed, independent of each other

and independent of other random variables. Note that \underline{U} was introduced in [4] for the purpose of easy analysis.

Let

$$\begin{aligned}\mathcal{X}_{\underline{c}}^{\mathcal{S}} &= \mathcal{X}_{c_1}^{i_1} \times \cdots \times \mathcal{X}_{c_k}^{i_k} \times \cdots \times \mathcal{X}_{c_d}^{i_d} \\ \mathcal{X}_{\hat{\underline{c}}}^{\mathcal{S}} &= \mathcal{X}_{\hat{c}_1}^{i_1} \times \cdots \times \mathcal{X}_{\hat{c}_k}^{i_k} \times \cdots \times \mathcal{X}_{\hat{c}_d}^{i_d}\end{aligned}\quad (7)$$

be the Cartesian product of signal subsets $\mathcal{X}_{c_k}^{i_k}$ and $\mathcal{X}_{\hat{c}_k}^{i_k}$, selected by the bits c_k and \hat{c}_k with the label positions $S_k = i_k$, respectively. According to the decoding rule \tilde{L}_k^i in (4), the path metric difference between \underline{c} and $\hat{\underline{c}}$ is

$$\begin{aligned}\delta &= \sum_{k=1}^d \max_{z_k \in \mathcal{X}_{c_k}^{i_k}} \log p_{\theta_k}(y_k | z_k) - \sum_{k=1}^d \max_{z_k \in \mathcal{X}_{\hat{c}_k}^{i_k}} \log p_{\theta_k}(y_k | z_k) \\ &= \max_{\underline{z} \in \mathcal{X}_{\underline{c}}^{\mathcal{S}}} \log p_{\theta}(\underline{y} | \underline{z}) - \max_{\underline{z} \in \mathcal{X}_{\hat{\underline{c}}}^{\mathcal{S}}} \log p_{\theta}(\underline{y} | \underline{z})\end{aligned}\quad (8)$$

That results in

$$\begin{aligned}P(\underline{c} \rightarrow \hat{\underline{c}} | \underline{S}, \underline{U}) &= P(\delta < 0 | \underline{S}, \underline{U}) \\ &= P\left(\max_{\underline{z} \in \mathcal{X}_{\hat{\underline{c}}}^{\mathcal{S}}} p_{\theta}(\underline{y} | \underline{z}) \leq \max_{\underline{z} \in \mathcal{X}_{\underline{c}}^{\mathcal{S}}} p_{\theta}(\underline{y} | \underline{z}) \middle| \underline{S}, \underline{U}\right) \\ &= E_{\underline{x}} \left[P\left(\max_{\underline{z} \in \mathcal{X}_{\hat{\underline{c}}}^{\mathcal{S}}} p_{\theta}(\underline{y} | \underline{z}) \leq \max_{\underline{z} \in \mathcal{X}_{\underline{c}}^{\mathcal{S}}} p_{\theta}(\underline{y} | \underline{z}) \middle| \underline{S}, \underline{U}, \underline{x}\right) \right] \\ &\leq E_{\underline{x}} \left[P\left(p_{\theta}(\underline{y} | \underline{x}) \leq \max_{\underline{z} \in \mathcal{X}_{\hat{\underline{c}}}^{\mathcal{S}}} p_{\theta}(\underline{y} | \underline{z}) \middle| \underline{S}, \underline{U}, \underline{x}\right) \right] \quad (a) \\ &\leq E_{\underline{x}} \left[\sum_{\underline{z} \in \mathcal{X}_{\hat{\underline{c}}}^{\mathcal{S}}} P\left(p_{\theta}(\underline{y} | \underline{x}) \leq p_{\theta}(\underline{y} | \underline{z}) \middle| \underline{S}, \underline{U}, \underline{x}\right) \right] \quad (b)\end{aligned}\quad (9)$$

where \underline{x} is the transmitted signal sequence and \underline{y} the received one. The upper bound (a) is because $p_{\theta}(\underline{y} | \underline{x}) \leq \max_{\underline{z} \in \mathcal{X}_{\hat{\underline{c}}}^{\mathcal{S}}} p_{\theta}(\underline{y} | \underline{z})$ is used in the comparison, and the upper bound (b) is due to the invoking of union bound. By using (5)-(9), the BICM_{UN} in [4] is given by

$$p_b \leq \frac{1}{k} \sum_{d=d_{\min}}^{\infty} W_l(d) f_{ub}(d, u, \mathcal{X}), \quad (10)$$

where

$$f_{ub}(d, u, \mathcal{X}) = m^{-d} \sum_{\underline{s}} 2^{-d} \sum_{\underline{U}} 2^{-d(m-1)} \sum_{\underline{x} \in \mathcal{X}_{\underline{c}}^{\underline{s}}} \sum_{\underline{z} \in \mathcal{X}_{\underline{c}}^{\underline{s}}} P(\underline{x} \rightarrow \underline{z}) . \quad (11)$$

Several observations can be made on BICM_{UN} in (10). Firstly, the bound is quite general and can be applied to any mapping u and constellation \mathcal{X} . Secondly, because of a union bound is invoked in (b), it is quite loose in general, respecially it is much looser than the union bound given in (5) and (6). And, finally, as shown in (11), it is quite difficult to evaluate. In [4], by introducing the symmetrization operation \underline{U} , a much simpler method was proposed in to ease this computation complexity.

BICM Expurgated Bound (BICM_{EX}) was also proposed in [4] in order to remedy the deficiencies associated with (BICM_{UN}). Instead of including all the error signal sequences $\underline{z} \in \mathcal{X}_{\underline{c}}^{\underline{s}}$ as in (11), only the unique nearest neighbor $\hat{\underline{z}}$ of \underline{x} in $\mathcal{X}_{\underline{c}}^{\underline{s}}$ is calculated in BICM_{EX} . With this simplification, BICM_{EX} is obtained as

$$p_b \leq \frac{1}{k} \sum_{d=d_{\min}}^{\infty} W_l(d) f_{ex}(d, u, \mathcal{X}), \quad (12)$$

where

$$f_{ex}(d, u, \mathcal{X}) = m^{-d} \sum_{\underline{s}} 2^{-d} \sum_{\underline{U}} 2^{-d(m-1)} \sum_{\underline{x} \in \mathcal{X}_{\underline{c}}^{\underline{s}}} P(\underline{x} \rightarrow \hat{\underline{z}}) \quad (13)$$

BICM_{EX} is considered as a tighter upper bound for the special case of QAM with gray labeling in [4] and just an accurate approximation for other forms of mappings or constellations. Nevertheless, as is to be shown, it is still an approximation even for QAM constellation with gray labeling.

3.2 New Tighter Bound for QAM Constellation with Gray Labeling

In this section, a new easy-to-calculate, tighter upper bound will be proposed for QAM constellation with gray labeling, which is known to have the best performance and constitutes a very large portion of practical applications of BICM systems. The

rationale that leads to the new upper bound roots on the following observations on the gray labeling of QAM constellations.

Observation 1: The error probability of a transmitted signal $x \in \mathcal{X}_{c_k}^{i_k}$ with decoding rule \tilde{L}_k^i depends only on the I or Q part of its binary label, i.e., all the signals in $\mathcal{X}_{c_k}^{i_k}$ with the same I or Q part of binary label have the same probability. The first and second half $m/2$ bits are arbitrarily to denote the I and Q part of the label, respectively. Fig. 6 shows the example of 16 QAM. According to the decoding rule in (4), the decision boundaries for $x \in \mathcal{X}_{c_k}^{i_k}$, $i_k = 1, 2, 3, 4$ are given in Fig 6 (a)-(d), respectively. As is clear, all the signals in $\mathcal{X}_{c_k}^{i_k}$ with the same I or Q binary label have the same error probability. For example, for $x \in \mathcal{X}_0^1$ with $l^1(x) = 0, l^2(x) = 0$, i.e., the signals with binary labels of 0000, 0001, 0011, and 0010 have the same error probability of $P\{n_{k,I} > 3\}$, where $n_{k,I}$ is the corresponding I part of noise. Likewise, for $x \in \mathcal{X}_1^3$ with $l^3(x) = 1, l^4(x) = 1$, i.e., the signals with binary labels of 0011, 0111, 1111, and 1011 have the error probability of $P\{n_{k,Q} > -1\}$, where $n_{k,Q}$ is the corresponding Q part of noise. Thus, only one out four signals has to be considered in the performance evaluation and the total number of signals that need to be considered is reduced from 16 to 4. In other words, a two-dimensional constellation is reduced to a one-dimensional PAM constellation.

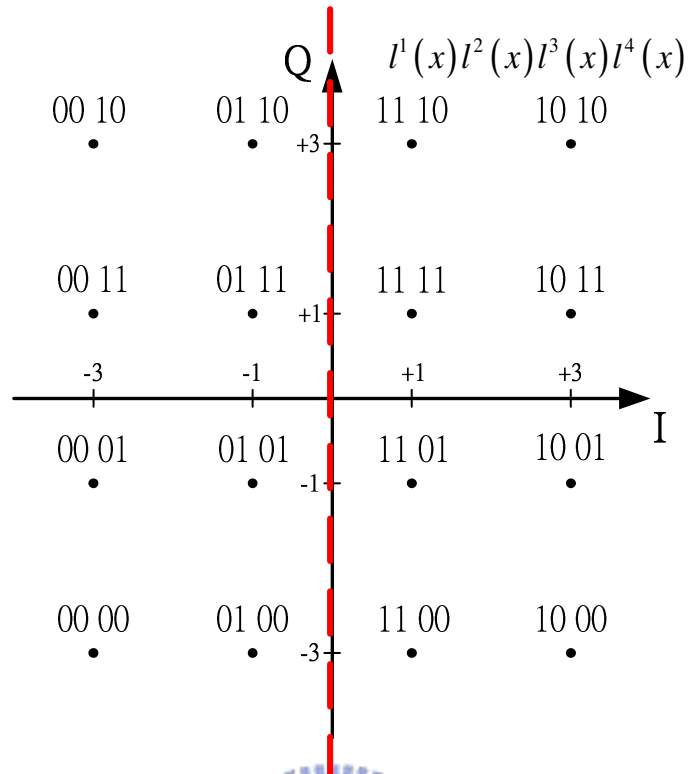


Fig.6 (a) Decision boundary between χ_0^1 and χ_1^1

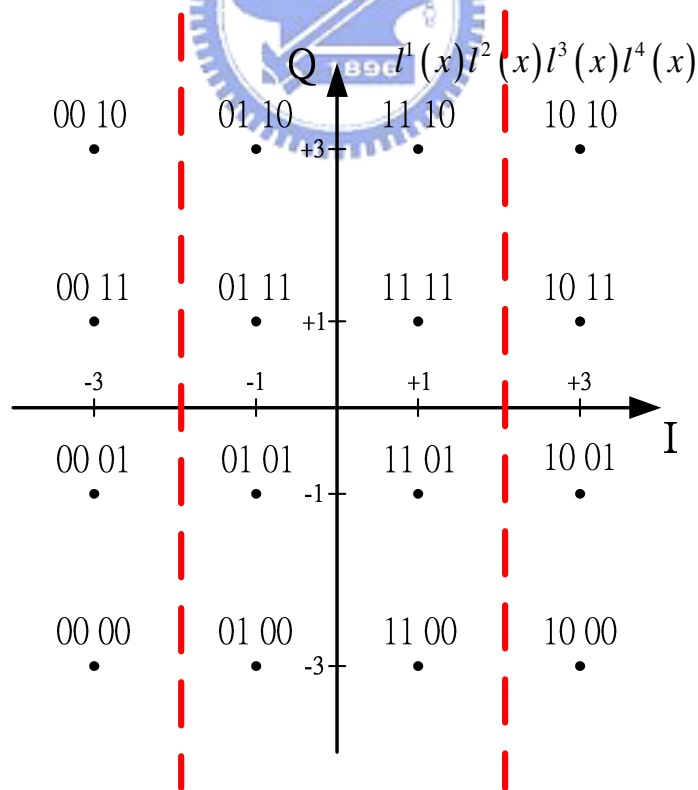


Fig.6 (b) Decision boundary between χ_0^2 and χ_1^2

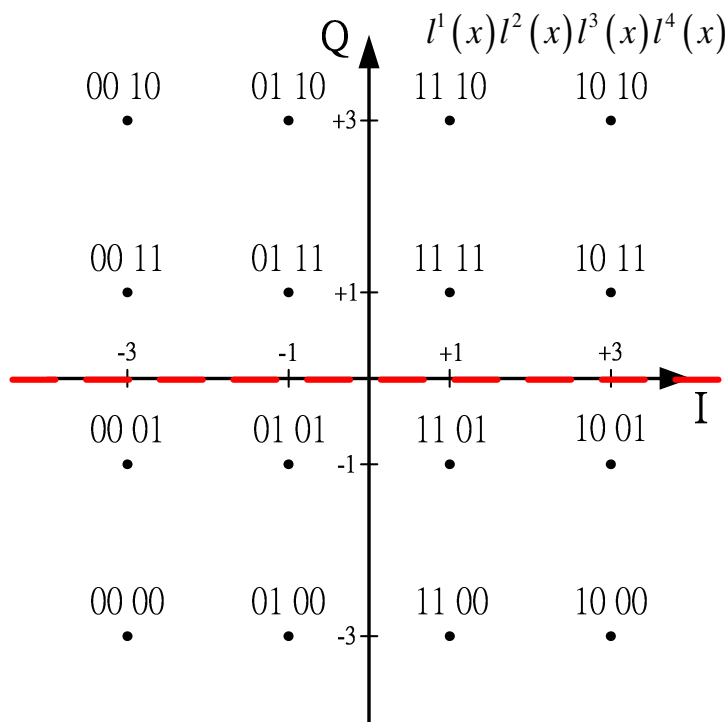


Fig.6 (c) Decision boundary between χ_0^3 and χ_1^3

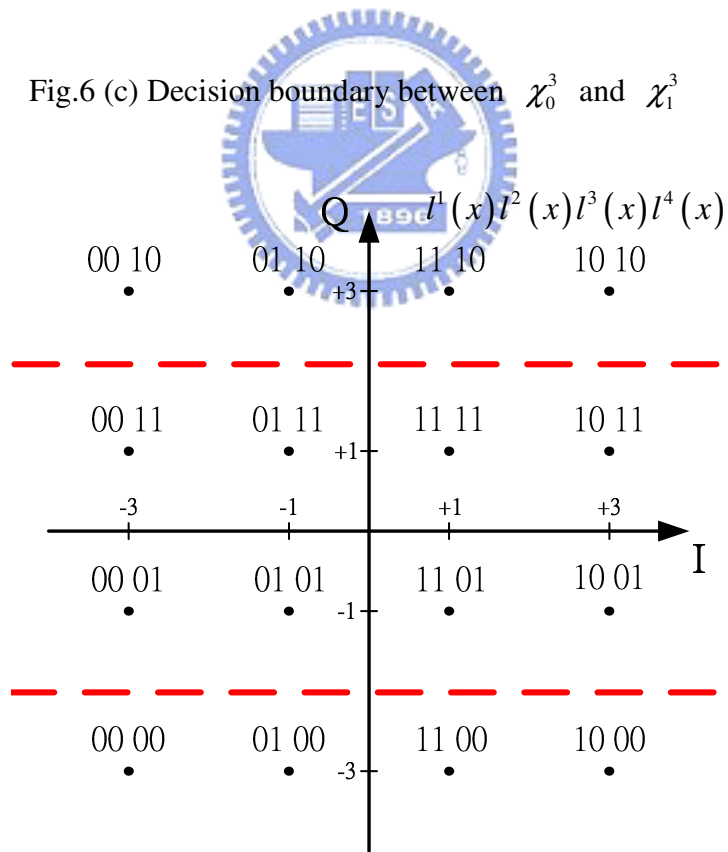
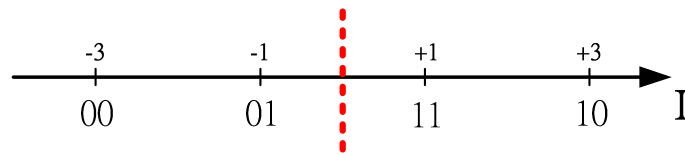


Fig.6 (d) Decision boundary between χ_0^4 and χ_1^4

Let $\psi_{c_k}^i$ be the equivalent one-dimensional signal set of $\chi_{c_k}^i$. Then, the equivalent (one-dimensional) signal sets and their decision boundaries for 16 QAM are shown as in Fig. 7 (a)-(b). Fig. 8 (a)-(c) are those for 64 QAM. This reduction of the number of signals will significantly simplify the performance evaluation, as to be seen. Again, I and Q may use different gray mapping and may be different from those shown above.

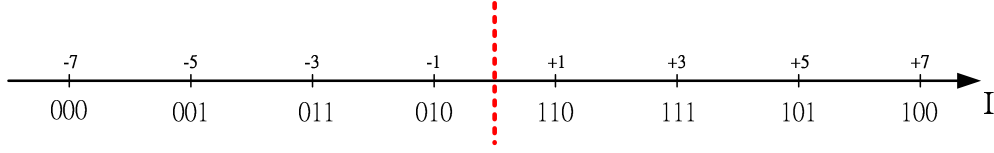


(a) $\psi_{c_k}^1, \psi_{c_k}^3$ with decision boundary

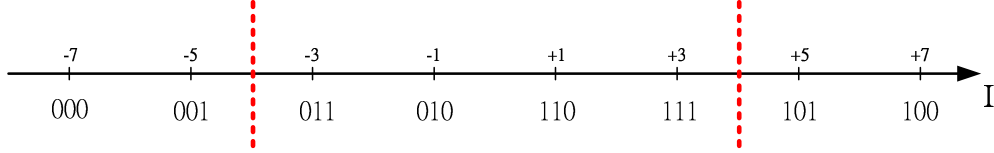


(b) $\psi_{c_k}^2, \psi_{c_k}^4$ with decision boundary

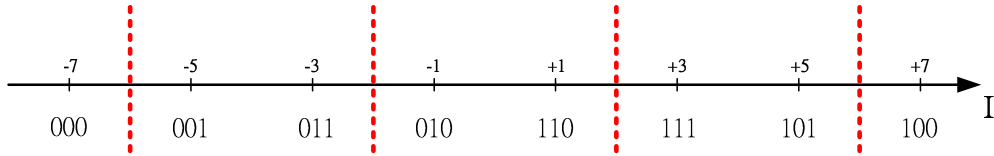
Fig.7 Equivalent one dimensional signal set $\psi_{c_k}^j$ for 16-QAM



(a) $\psi_{c_k}^1, \psi_{c_k}^4$ with decision boundary



(b) $\psi_{c_k}^2, \psi_{c_k}^5$ with decision boundary



(c) $\psi_{c_k}^3, \psi_{c_k}^6$ with decision boundary

Fig.8 Equivalent one-dimensional signal set $\psi_{c_k}^i$ for 64-QAM

Observation 2: Given the decision boundary of $\psi_{c_k}^{i_k}$ and $\psi_{c_k}^{\hat{i}_k}$, the pair-wise error probability $P\{x \rightarrow \hat{x}\}$, where $x \in \psi_{c_k}^{i_k}$ and $\hat{x} \in \psi_{c_k}^{\hat{i}_k}$, can be evaluated by

$P\{p_\theta(y|x) \leq p_\theta(y|w)\}$, with w defined as the *virtual* signal of \hat{x} . More specifically, w is defined in the way that if only the pair of signals x and w are considered, the decision boundary determined by $p_\theta(y|x) = p_\theta(y|w)$ will be coincide with the original boundary so that $P\{x \rightarrow \hat{x}\} = P\{p_\theta(y|x) \leq p_\theta(y|w)\}$.

For example, in Fig. 7(b), if $x = -1$, and $\hat{x} = 3$, then $w = 5$. As will be clear, the definition of w will facilitate in the expression of our upper bound.

Equipped with these observations on gray labeling, we can now proceed to derive the new upper bound. Practically, our job to derive the new upper bound is just

to find a tighter bound for the conditional PEP $P(\underline{c} \rightarrow \hat{\underline{c}} | \underline{S}, \underline{U})$ in (6). Following the notation in (9), we have

$$\begin{aligned}
P(\underline{c} \rightarrow \hat{\underline{c}} | \underline{S}, \underline{U}) &= P(\mathcal{D} < 0 | \underline{S}, \underline{U}) \\
&= P\left(\max_{\underline{z} \in \Psi_{\underline{c}}^{\underline{S}}} p_{\theta}(\underline{y} | \underline{z}) \leq \max_{\underline{z} \in \Psi_{\hat{\underline{c}}}^{\underline{S}}} p_{\theta}(\underline{y} | \underline{z}) \middle| \underline{S}, \underline{U}\right) \\
&= E_{\underline{x}} \left[P\left(\max_{\underline{z} \in \Psi_{\underline{c}}^{\underline{S}}} p_{\theta}(\underline{y} | \underline{z}) \leq \max_{\underline{z} \in \Psi_{\hat{\underline{c}}}^{\underline{S}}} p_{\theta}(\underline{y} | \underline{z}) \middle| \underline{S}, \underline{U}, \underline{x}\right) \right] \quad (14) \\
&\leq E_{\underline{x}} \left[P\left(p_{\theta}(\underline{y} | \underline{x}) \leq \max_{\underline{w} \in \Omega_{\hat{\underline{c}}}^{\underline{S}}} p_{\theta}(\underline{y} | \underline{w}) \middle| \underline{S}, \underline{U}, \underline{x}\right) \right] \quad (a) \\
&\leq E_{\underline{x}} \left[\sum_{\underline{w} \in \Omega_{\hat{\underline{c}}}^{\underline{S}}} P\left(p_{\theta}(\underline{y} | \underline{x}) \leq p_{\theta}(\underline{y} | \underline{w}) \middle| \underline{S}, \underline{U}, \underline{x}\right) \right] \quad (b)
\end{aligned}$$

where

$$\Omega_{\hat{\underline{c}}}^{\underline{S}} = \left\{ \underline{w} = (\dots, w_{-1}, w_0, w_1, \dots) \middle| \begin{array}{l} w_k = \text{virtual signal of } \hat{x} \in \Psi_{\hat{c}_k}^{S_k} \\ \text{with respect to the transmitted signal } x \end{array} \right\} \quad (15)$$

The bound 14 (b) is tighter than (9-b) because of the following two reasons. (i) Fewer terms are included in the union bound. Recall that from *Observation 1*, only \sqrt{M} rather than M signals are needed to be considered in our case. (ii) The true decision boundary is used in 11 (a), and this results in a tighter bound. For example, see Fig. 7(b), if $x = -1$, and $\hat{x} = 3$, then by using (9-b), the decision boundary will be $y = 1$, but in fact the true boundary is $y = 2$.

The upper bound in 11 (b) can be made tighter by removing the irrelevant error events in the union bound. Since we just need to consider the one-dimensional constellation, for a given x , only the nearest signals on both side of x , denoted \hat{x}_l and \hat{x}_r , in the set of $\Omega_k^{S_k}$ required to be included. It is easy to see that the set of y that results in an error signal $\hat{x} \neq \hat{x}_l$ and $\hat{x} \neq \hat{x}_r$ have been accounted for when considering \hat{x}_l or \hat{x}_r . Let $\hat{\Omega}_{\hat{\underline{c}}}^{\underline{S}}$ be the subset of $\Omega_{\hat{\underline{c}}}^{\underline{S}}$ with the \hat{x}_l and \hat{x}_r being

retained in the set of $\psi_{\hat{c}_k}^{S_k}$. Then a tighter bound is obtained for the conditional PEP

$$\begin{aligned}
& P(\underline{c} \rightarrow \hat{\underline{c}} | \underline{S}, \underline{U}) \\
& \leq E_{\underline{x}} \left[\sum_{\underline{w} \in \hat{\Omega}_{\hat{\underline{c}}}^S} P\left(p_{\theta}(\underline{y} | \underline{x}) \leq p_{\theta}(\underline{y} | \underline{w}) | \underline{S}, \underline{U}, \underline{x}\right) \right] \quad (16)
\end{aligned}$$

The idea of expurgating the irrelevant error events in (16) is similar to the one used for BICM_{EX} in [4]. Nevertheless, only one side of the error signals \hat{x}_l or \hat{x}_r is included in BICM_{EX} and that makes it only an approximation even for QAM constellation with gray labeling.

By using (16), the new upper bound BICM_{NEW} is obtained as follows.

$$p_b \leq \frac{1}{k} \sum_{d=d_{\min}}^{\infty} W_l(d) f_{new}(d, u, \chi) \quad (17)$$

where

$$f_{new}(d, u, \chi) = m^{-d} \sum_{\underline{s}} 2^{-d} \sum_{\underline{u}} 2^{-d(m/2-1)} \sum_{\underline{x} \in \mathcal{W}_{\underline{s}}^S} \sum_{\underline{w} \in \hat{\Omega}_{\underline{s}}^S} P(\underline{x} \rightarrow \underline{w}) . \quad (18)$$

Methods for computing the weight distribution $W_l(d)$ for punctured convolutional codes has been well known as in [16], where the original error-state diagram of the convolutional code was modified to account for the effects due to the puncturing. Only the calculation of $f_{new}(d, u, \chi)$ will be discussed in the following.

3.3 Pair-wise Error Probability

Without loss of generality, assume that the same gray labeling is applied to both I and Q components of the signal x . Since the bit error probability is the same for both components, we do not need to differential whether I or Q of a coded bit is mapped to. Only 16 QAM and 64 QAM will be explicitly considered. Other size of constellation can be treated similarly.

3.3.1 Pair-wise Error Probability for Soft-decision in AWGN Channels

In AWGN channels, $P(\underline{x} \rightarrow \underline{w})$ is given by

$$P(\underline{x} \rightarrow \underline{w}) = Q \left(\rho(\underline{x}; \underline{w}) \sqrt{\frac{2m\Delta^2 RE_b}{dN_0}} \right) \quad (19)$$

where

$$Q(\alpha) = \frac{1}{\sqrt{2\pi}} \int_{\alpha}^{\infty} e^{-(y^2/2)} dy,$$

$\rho(\underline{x}; \underline{w}) \triangleq \sum_{k=1}^d \frac{|x_k - w_k|}{2}$ is a half of the Euclidean distance between \underline{w} and \underline{x} , Δ the power normalization factor of M -ary QAM, E_b bit energy, N_0 the one-sided noise density and R code rate. $\Delta = 1/\sqrt{10}$ for 16 QAM, and $\Delta = 1/\sqrt{42}$ for 64 QAM. Using (19), (7) becomes

$$f_{new}(d, u, \chi) = m^{-d} \sum_{\underline{s}} 2^{-d} \sum_{\underline{u}} 2^{-d(m/2-1)} \sum_{x \in \mathcal{W}_{\underline{s}}^{\chi}} \sum_{w \in \mathcal{Q}_{\underline{s}}^{\chi}} Q \left(\rho(\underline{x}; \underline{w}) \sqrt{\frac{2m\Delta^2 RE_b}{dN_0}} \right) \quad (20)$$

The computation of (21) can be further simplified by utilizing symmetrization constellation, which have the symmetric property introduced in [17], of one-dimensional PAM constellation. Consider 16QAM as an example. First define the signal subsets $X_1 \triangleq \{(0,0), (1,0)\}$ and $X_2 \triangleq \{(0,1), (1,1)\}$. From Fig. 8(a) it is observed that for $x \in X_1$ has the same error probability $P(x \rightarrow w)$, and so does for $x \in X_2$, no matter if the MSB (first label position) or the LSB (second label position) is considered. Indeed, this is the case; for MSB $\rho(x; w) = 1$ for $x \in X_2$, and $\rho(x; w) = 3$ for $x \in X_1$. Likewise, for LSB, $\rho(x; w) = 1$ for $x \in X_1$, and $\rho(x; w_1) = 3$ and $\rho(x; w_2) = 1$ for $x \in X_2$. Note that for $x \in X_2$, there are two regions for errors to occur when bit error in LSB is considered. With this symmetry property, (21) can be simplified as follows.

$$f_{new}(d, u, \chi) = 2^{-2d} \sum_{i=0}^d \binom{d}{i} \cdot \sum_{i_1=0}^i \binom{i}{i_1} \sum_{j_1=0}^j \binom{j}{j_1} \sum_{s=0}^{j_2} \binom{j_2}{s} \mathcal{Q} \left(\left\{ 3i_1 + i_2 + j_1 + [(j_2 - s) + 3s] \right\} \sqrt{\frac{4RE_b}{5dN_0}} \right) \quad (21)$$

where

- $d = i + j$ is the total number of bit errors.
- i and j are the number of bit errors in MSB and LSB, respectively.
- $i = i_1 + i_2$.
- i_1 is the number of MSB errors with $x \in X_1$ and i_2 is with $x \in X_2$.
- $j = j_1 + j_2$.
- j_1 is the number of LSB errors with $x \in X_1$ and j_2 is with $x \in X_2$.
- s is the number of LSB errors with $x \in X_2$ and $\rho(x; w_1) = 3$.

Similar idea can be applied to the case 64-QAM. In this case we have $X_1 = \{000, 100\}$, $X_2 = \{001, 101\}$, $X_3 = \{011, 111\}$, and $X_4 = \{010, 110\}$. For any $x \in X_i$, the error probability $P(x \rightarrow w)$ is the same no matter if the MSB, center bit or the LSB is considered. The result is given by

$$\begin{aligned} & f_{new}(d, u, \chi) \\ &= 3^{-d} \sum_{i=0}^d \sum_{j=0}^{d-i} \binom{d}{i} \binom{d-i}{j} \cdot \\ & 4^{-d} \sum_{i_1=0}^i \sum_{i_2=0}^{i-i_1} \sum_{i_3=0}^{i-i_1-i_2} \binom{i}{i_1} \binom{i-i_1}{i_2} \binom{i-i_1-i_2}{i_3} \cdot \\ & \sum_{j_1=0}^j \sum_{j_2=0}^{j-j_1} \sum_{j_3=0}^{j-j_1-j_2} \binom{j}{j_1} \binom{j-j_1}{j_2} \binom{j-j_1-j_2}{j_3} \sum_{t=0}^{j_3} \binom{j_3}{t} \sum_{v=0}^{j_4} \binom{j_4}{v} \cdot \\ & \sum_{r_1=0}^r \sum_{r_2=0}^{r-r_1} \sum_{r_3=0}^{r-r_1-r_2} \binom{r}{r_1} \binom{r-r_1}{r_2} \binom{r-r_1-r_2}{r_3} \sum_{s=0}^{r_2+r_3+r_4} \binom{r_2+r_3+r_4}{s} \cdot \\ & \mathcal{Q} \left(\left\{ \begin{array}{l} 7i_1 + 5i_2 + 3i_3 + i_4 + 3j_1 + j_2 + [(j_3 - t) + 7t] + \\ [3(j_4 - v) + 5v] + [(r - s) + 3s] \end{array} \right\} \sqrt{\frac{2RE_b}{7dN_0}} \right) \end{aligned} \quad (22)$$

where $d = i + j + r$, where i, j , and r are the number of bit errors in MSB, center bit, and LSB, $i = i_1 + i_2 + i_3 + i_4$, $j = j_1 + j_2 + j_3 + j_4$, and $r = r_1 + r_2 + r_3 + r_4$.

3.3.2 Pair-wise Error Probability with Soft-Decision in Rayleigh Fading Channels

In fading channels, we apply the Chernoff bound [18-20] to obtain

$$P(\underline{x} \rightarrow \underline{w}) \leq \frac{1}{2} \prod_{i=1}^d \frac{1}{1 + \text{SNR} \left(\frac{x_i - w_i}{2} \right)^2} \quad (23)$$

Therefore, PEP is upper-bounded by

$$f_{new}(d, u, \chi) \leq m^{-d} \sum_{\underline{s}} 2^{-d} \sum_{\underline{u}} 2^{-d(m/2-1)} \sum_{\underline{x} \in \Psi_{\underline{s}}^d} \sum_{\underline{w} \in \hat{\Omega}_{\underline{x}}^d} \frac{1}{2} \prod_{i=1}^d \frac{1}{1 + \text{SNR} \left(\frac{x_i - w_i}{2} \right)^2} \quad (24)$$

where the average $\text{SNR} = \frac{m\Delta^2 RE_b}{N_0}$.

Again, by using the symmetry property, we have for 16-QAM

$$f_{new}(d, u, \chi) \leq 2^{-2d} \sum_{i=0}^d \binom{d}{i} \sum_{i_1=0}^i \binom{i}{i_1} \sum_{j_1=0}^j \binom{j}{j_1} \sum_{s=0}^{j_2} \binom{j_2}{s} \frac{1}{2} \left(\frac{1}{1+3^2 \text{SNR}} \right)^{i_1+s} \left(\frac{1}{1+\text{SNR}} \right)^{i_2+j_1+j_2-s} \quad (25)$$

where $\text{SNR} = \frac{2RE_b}{5N_0}$. And, for 64-QAM

$$\begin{aligned} & f_{new}(d, u, \chi) \\ & \leq 3^{-d} \sum_{i=0}^d \sum_{j=0}^{d-i} \binom{d}{i} \binom{d-i}{j} 4^{-d} \sum_{i_1=0}^i \sum_{i_2=0}^{i-i_1} \sum_{i_3=0}^{i-i_1-i_2} \binom{i}{i_1} \binom{i-i_1}{i_2} \binom{i-i_1-i_2}{i_3} \\ & \quad \sum_{j_1=0}^j \sum_{j_2=0}^{j-j_1} \sum_{j_3=0}^{j-j_1-j_2} \binom{j}{j_1} \binom{j-j_1}{j_2} \binom{j-j_1-j_2}{j_3} \sum_{t=0}^{j_3} \binom{j_3}{t} \sum_{v=0}^{j_4} \binom{j_4}{v} \\ & \quad \sum_{r_1=0}^r \sum_{r_2=0}^{r-r_1} \sum_{r_3=0}^{r-r_1-r_2} \binom{r}{r_1} \binom{r-r_1}{r_2} \binom{r-r_1-r_2}{r_3} \sum_{s=0}^{r_2+r_3+r_4} \binom{r_2+r_3+r_4}{s} \\ & \quad \frac{1}{2} \left(\frac{1}{1+7^2 \text{SNR}} \right)^{i_1+t} \left(\frac{1}{1+5^2 \text{SNR}} \right)^{i_2+v} \left(\frac{1}{1+3^2 \text{SNR}} \right)^{i_3+j_1+j_4-v+s} \left(\frac{1}{1+\text{SNR}} \right)^{i_4+j_2+j_3-t+r-s} \end{aligned} \quad (26)$$

where $\text{SNR} = \frac{RE_b}{7N_0}$.

3.4 Numerical Results

BICM systems with different punctured convolutional codes and modulation levels are analyzed with BICM_{UB} , BICM_{EX} and the new BICM_{NEW} for both AWGN and fading channels. Simulation results are also given to verify the tightness of the performance upper bounds.

3.4.1 (2,1,6) Convolutional code

Numerical results for BICM-RLP based on (2,1,6) convolutional code (constraint length $\kappa = 7$) with the generator polynomials (133,171) are given in this section. Fig.9 and Fig.10 compare BICM_{UB} , BICM_{EX} and BICM_{NEW} for 16 QAM over AWGN and Rayleigh fading channels, respectively. BICM_{UB} is a quite a loose bound. But, BICM_{EX} does provide an accurate approximation, although theoretically it is not an upper bound. As expected, the new BICM_{NEW} is very tight for BER of practical interest, as compared to the simulated BER. It is interesting to note that BICM_{NEW} and BICM_{EX} almost overlap with each other for the example shown in Fig.10. Fig.11 and Fig.12 give more numerical results, including those with 64QAM. Again, BICM_{NEW} provides a very tight upper bound for all the cases.

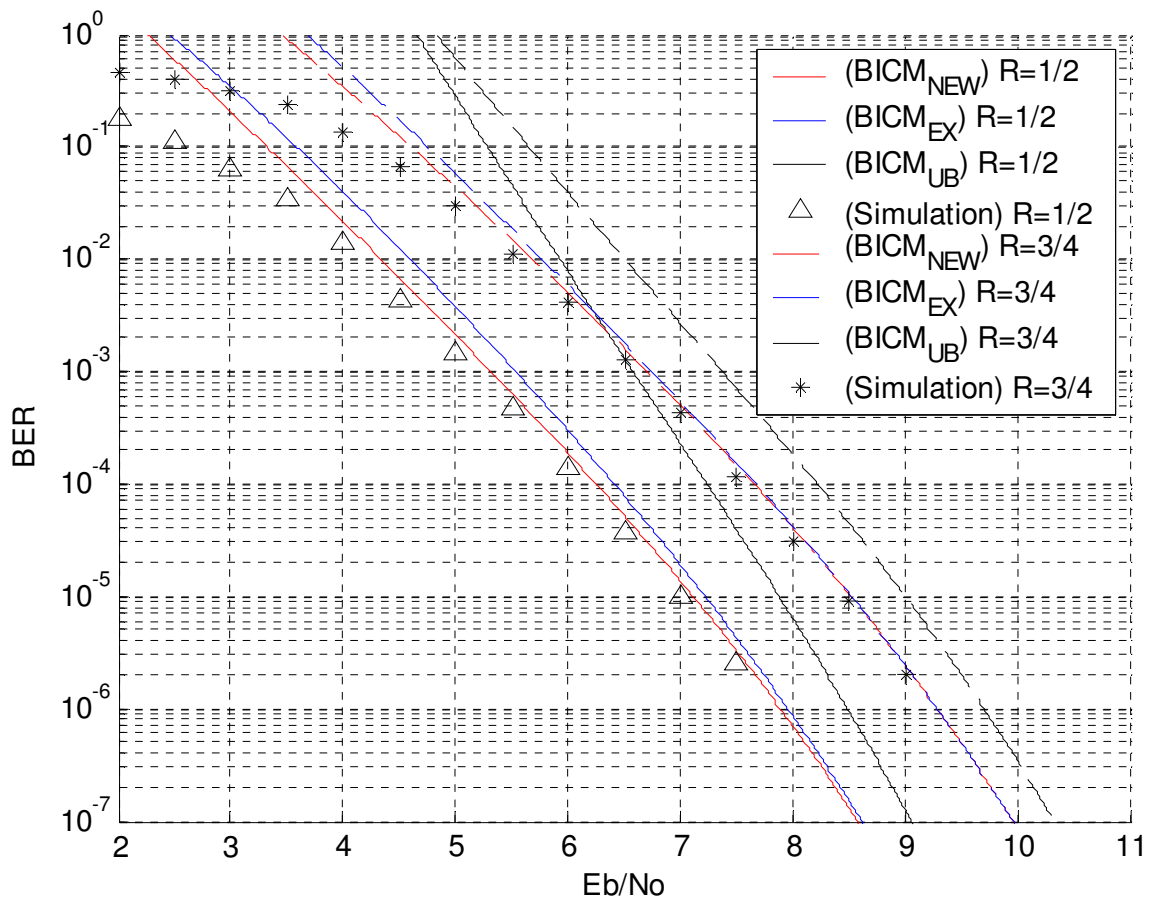


Fig.9 Performance of BICM-RLP in AWGN channels ($\kappa = 7$, 16QAM)

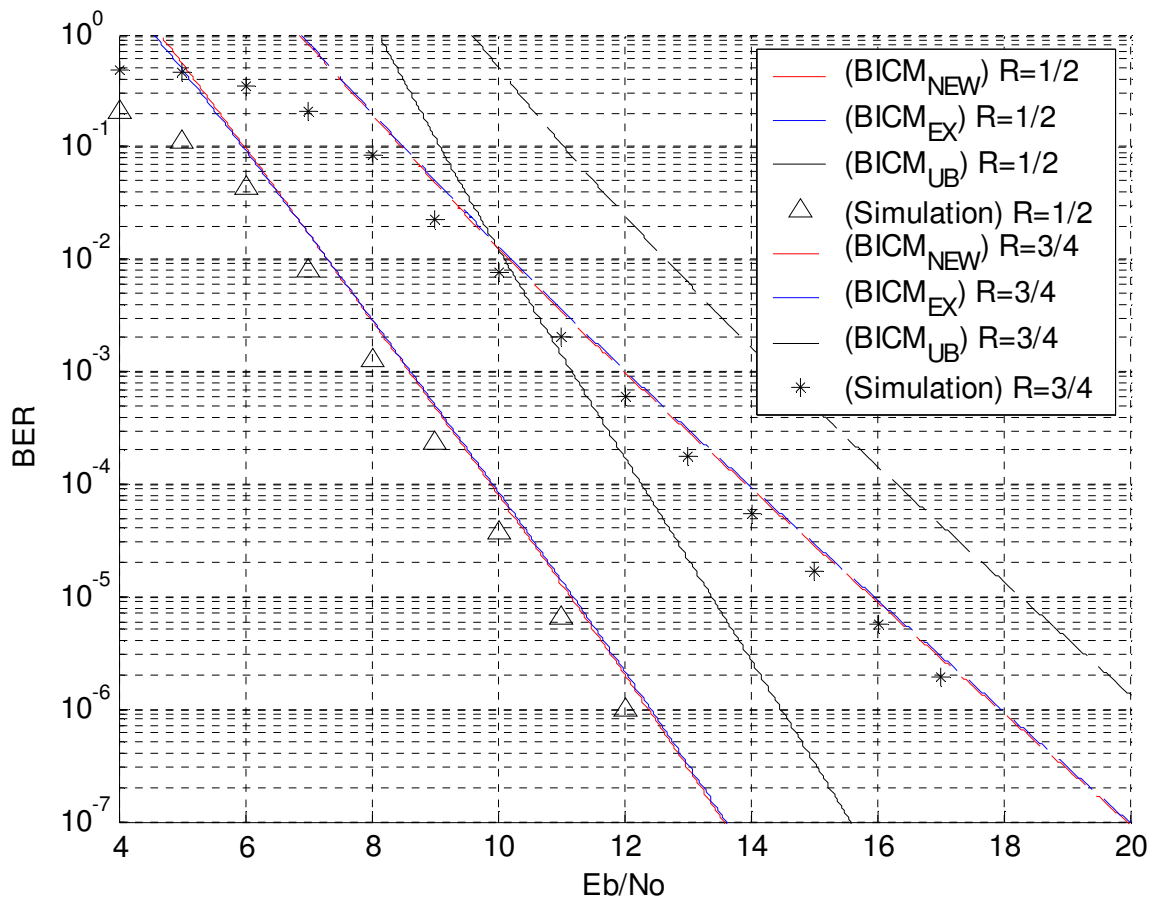


Fig.10 Performance of BICM-RLP in Rayleigh fading channels ($\kappa = 7$, 16QAM)

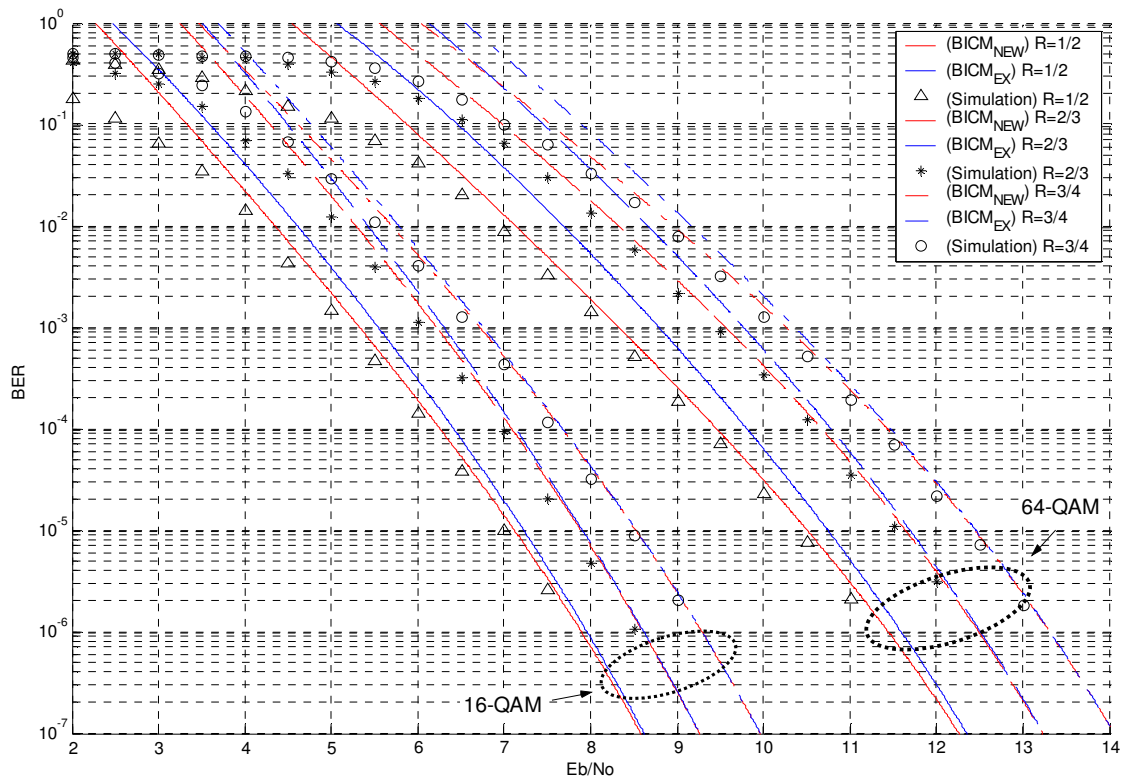


Fig.11 Performance of BICM-RLP in AWGN channels ($\kappa = 7, 16, 64$ QAM)



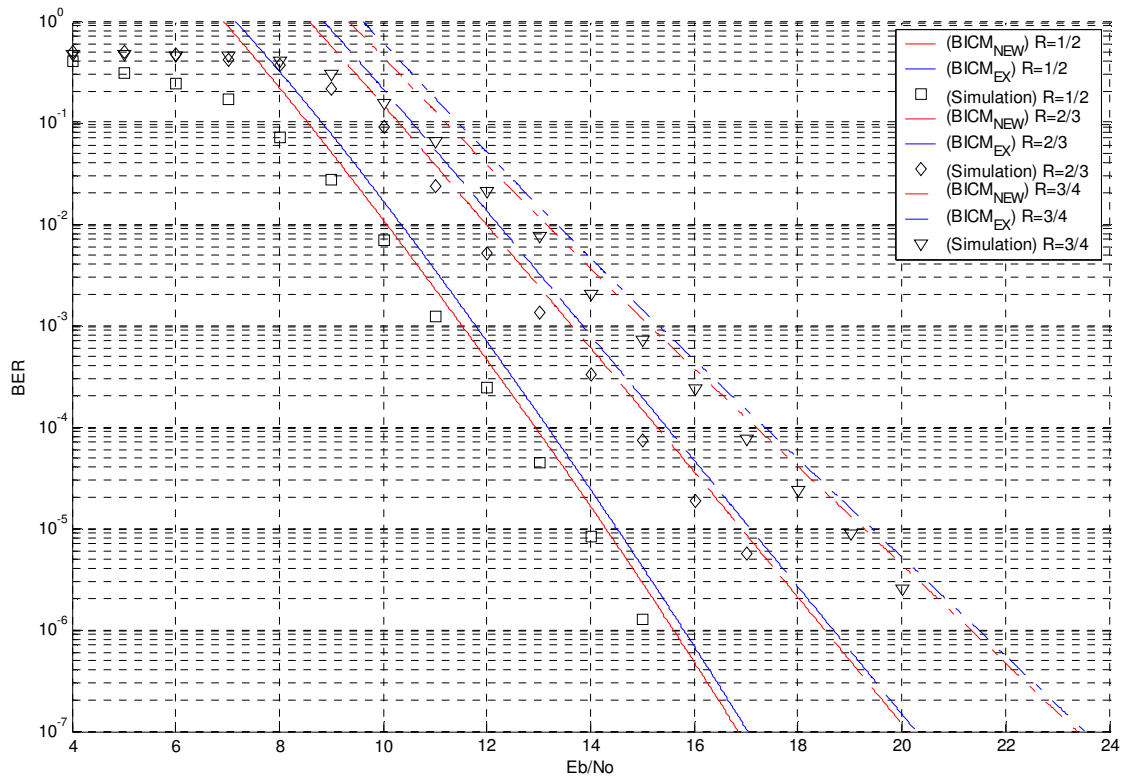


Fig.12 Performance of BICM-RLP in Rayleigh fading channels ($\kappa = 7$, 64QAM)



3.4.2 (2,1,2) Convolutional code

Numerical results for BICM-RLP based on (2,1,2) convolutional code ($\kappa=3$) with the generator polynomials (5,7) are given in this section. Fig.13 and Fig.14 compares BICM_{UB} , BICM_{EX} and BICM_{NEW} for 16QAM systems over AWGN and Rayleigh fading channels, respectively. Similar results are observed: BICM_{UB} is a loose bound, BICM_{EX} provides a good approximation, and BICM_{NEW} is a very tight bound. More numerical results for this case are shown in Fig.15 and Fig.16.

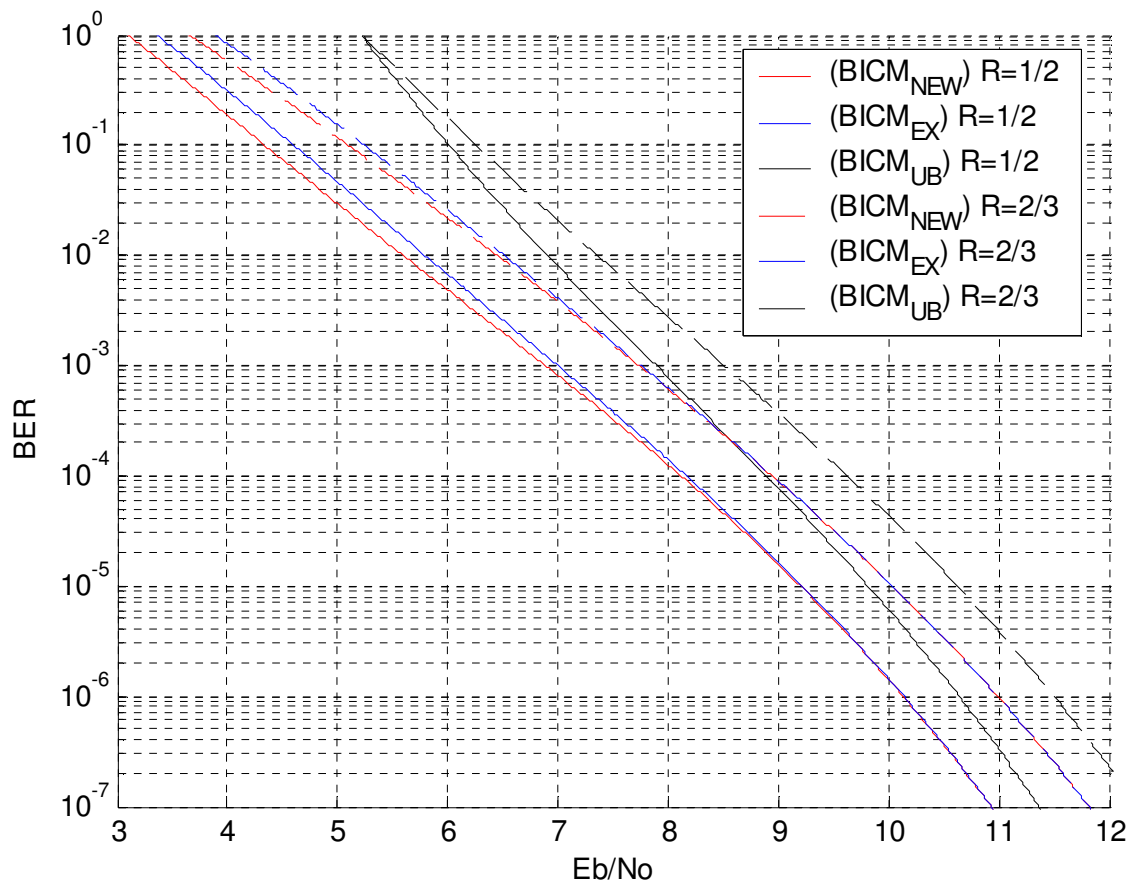


Fig.13 Performance of BICM-RLP in AWGN channels ($\kappa=3$, 16QAM)

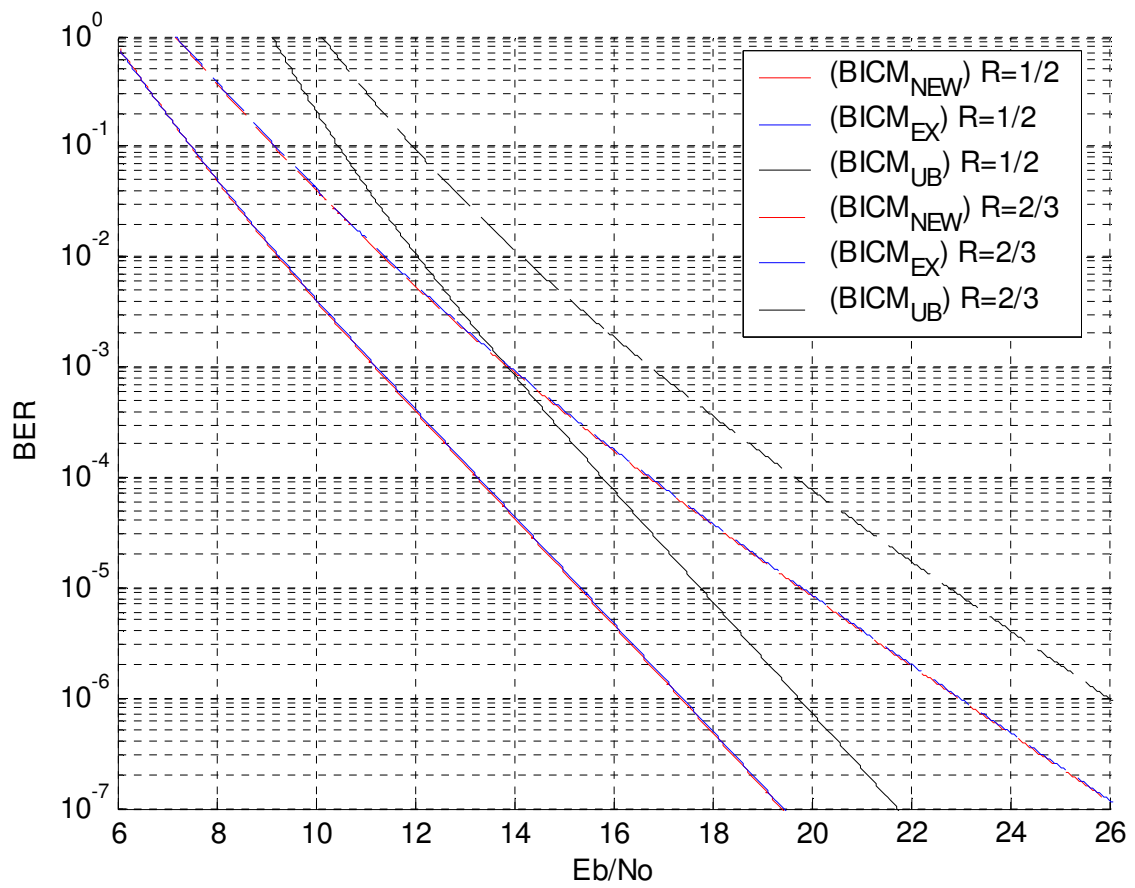


Fig.14 Performance of BICM-RLP in Rayleigh fading channels ($\kappa = 3$, 16QAM)



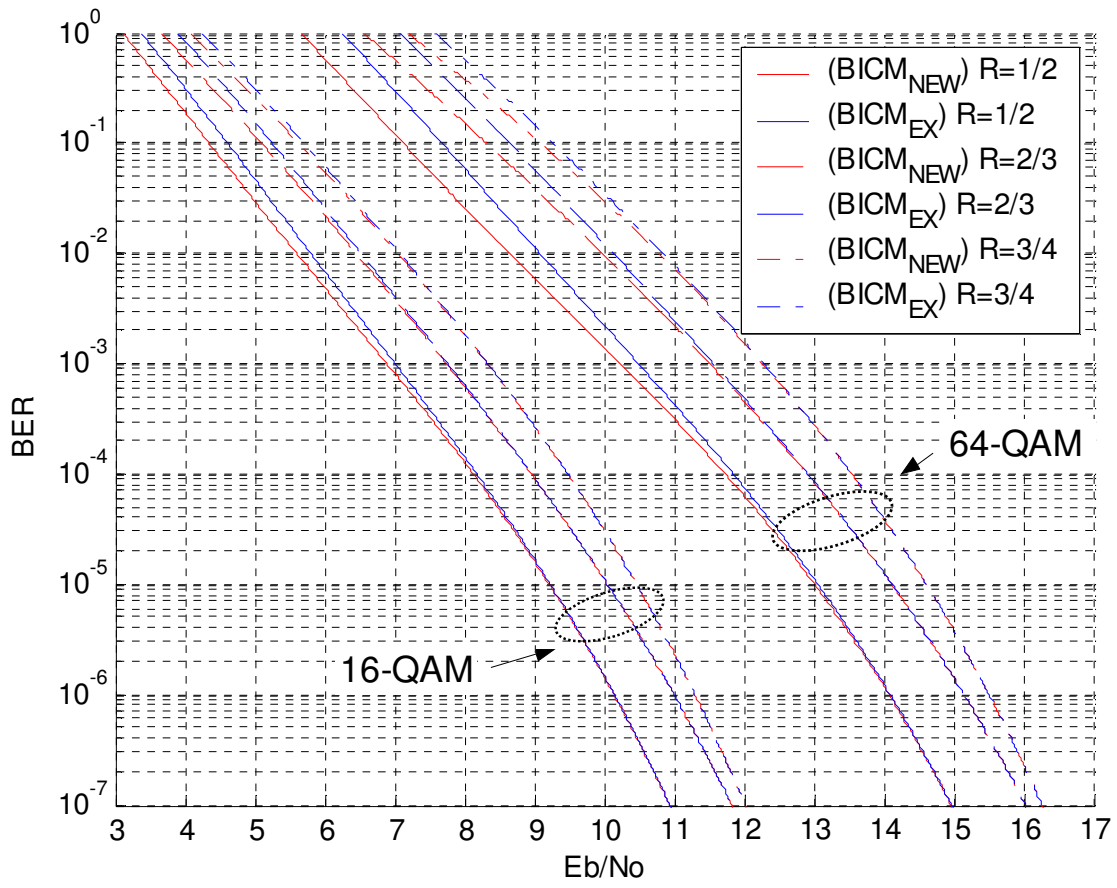


Fig.15 Performance of BICM-RLP in AWGN channels ($k = 3, 16, 64$ QAM)



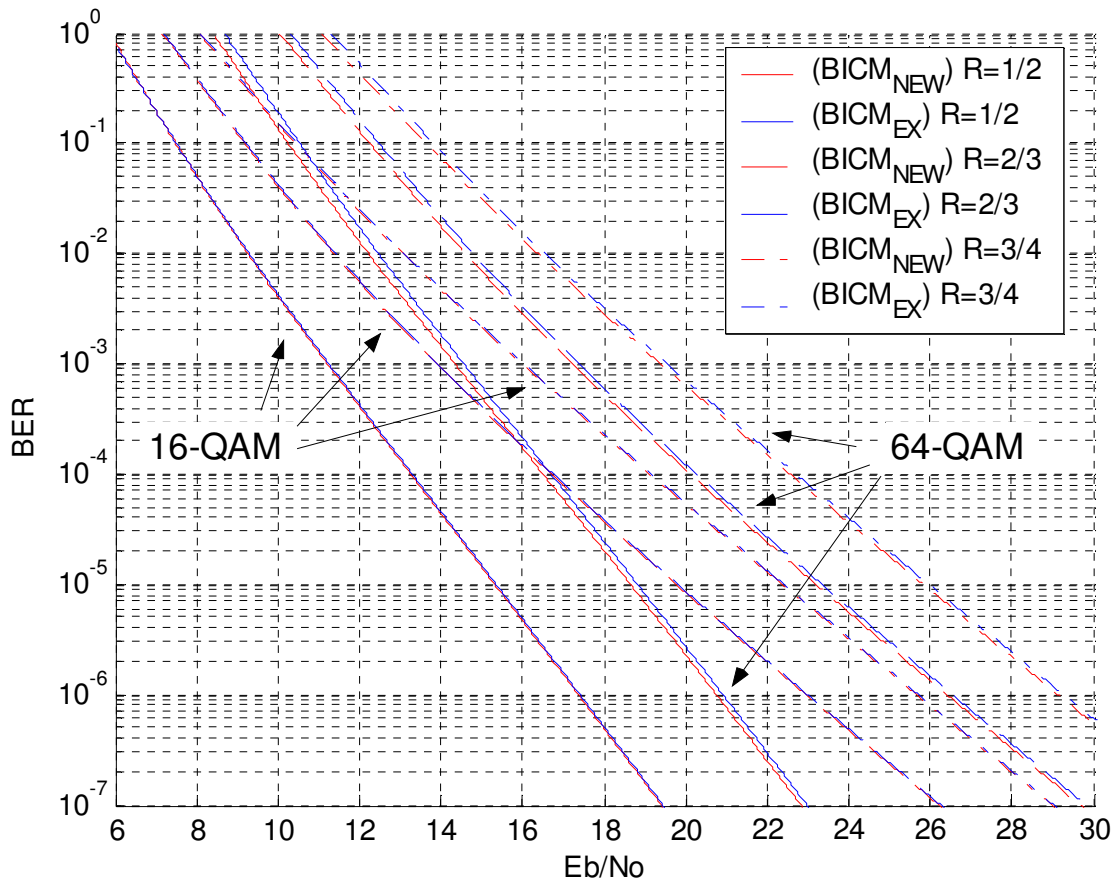


Fig.16 Performance of BICM-RLP in Rayleigh fading channels ($\kappa = 3, 16, 64$ QAM)



Chapter 4: Upper Bounds for BICM with Fixed Label-position Mapping (BICM-FLP)

In BICM-FLP, there is a fixed mapping between a coded bit and label position of signal x . Therefore, the average over \underline{S} in (18) is no longer needed. From (18), the upper bound becomes

$$p_b \leq \frac{1}{k} \sum_{d=d_{\min}}^{\infty} W_I(d) f_{new}(d, u, \chi) \quad (27)$$

where

$$\begin{aligned} f_{new}(d, u, \chi) &\triangleq E[P(\underline{c} \rightarrow \hat{\underline{c}}) | \underline{U}] \\ &= 2^{-d} \sum_{\underline{U}} 2^{-d(m/2-1)} \sum_{\underline{x} \in \Psi_{\underline{c}}^{\underline{S}}} \sum_{\underline{w} \in \hat{\Omega}_{\underline{x}}^{\underline{S}}} P(\underline{x} \rightarrow \underline{w}) \end{aligned} \quad (28)$$

On the other hand, the error probability of an error event depends on the positions where the error occurs. For example, depends on whether the MSB or LSB in errors in the 16QAM case. The error positions in an error event need to be taken into account in the analysis.

4.1 Modified Error State Diagram and Transfer Function with no Puncturing

4.1.1 Modified Error State Diagram

The first step toward the performance analysis of BICM-FLP is to define a *modified* error state diagram that can enumerate the error positions in an error event. For simplicity, a (2,1,2) convolutional code of the generator polynomials (5,7) with 16- and 64-QAM constellations will be used as examples.

For the 16-QAM constellation, the modified state diagram is shown in Fig.17, where a branch with label $M^i L^j Y^l$ is to denote that, associated with this branch, there are i MSB and j LSB and l information bits in errors. The self-loop of state zero is removed by splitting the zero state into two states S_a and S_b . The remaining

states are labeled S_1 , S_2 , and S_3 to represent the state 01, 10, and 11. The transfer function therefore then is expressed as

$$T(M, L, Y) = \sum_{i,j,l} w_{i,j,l} M^i L^j Y^l, \quad (29)$$

where the coefficient $w_{i,j,l}$ denotes the number of paths with i MSB, j LSB and l information bits in error.

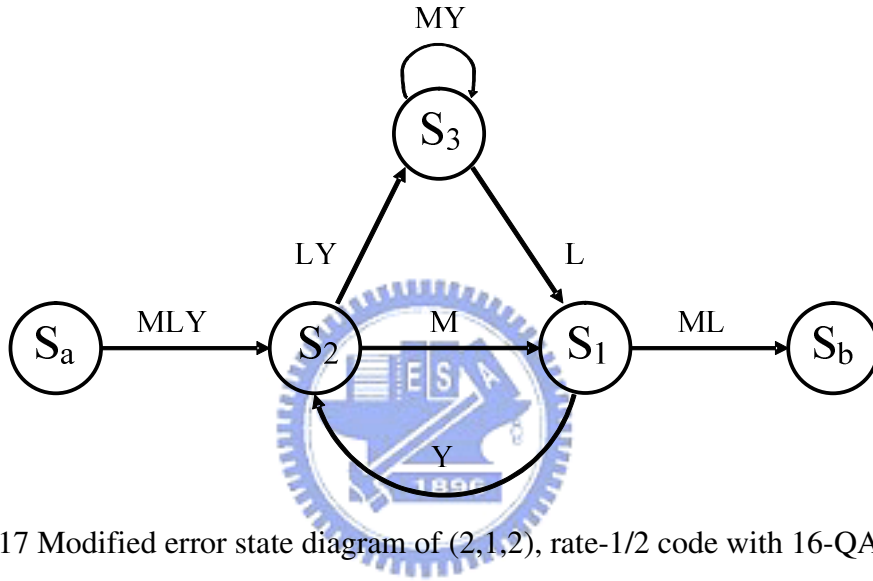


Fig.17 Modified error state diagram of (2,1,2), rate-1/2 code with 16-QAM

The same idea is applicable to 64QAM. Then, we have the transfer function given by

$$T(M, C, L, Y) = \sum_{i,j,r,l} w_{h,i,j,k} M^i C^j L^r Y^l \quad (30)$$

where C is to denote the center label position, and $w_{i,j,r,l}$ is the number of paths with i MSB, j center bit, r LSB, and l information bits in error.

4.1.2 Transfer Function [16]

The procedure in [16] will be used to find the transfer functions in (29) and (30). For

Fig. 17, the modified error state diagram is described by the matrix equation

$$\begin{bmatrix} S_1 \\ S_2 \\ S_3 \end{bmatrix} = \begin{bmatrix} 0 & M & L \\ Y & 0 & 0 \\ 0 & LY & MY \end{bmatrix} \begin{bmatrix} S_1 \\ S_2 \\ S_3 \end{bmatrix} + \begin{bmatrix} 0 \\ MLY \\ 0 \end{bmatrix} S_a \quad (31)$$

or

$$\mathbf{S} = \mathbf{A}\mathbf{S} + \mathbf{B}S_a, \quad (32)$$

where

$$\mathbf{S} \triangleq \begin{bmatrix} S_1 \\ S_2 \\ S_3 \end{bmatrix}, \mathbf{A} \triangleq \begin{bmatrix} 0 & M & L \\ Y & 0 & 0 \\ 0 & LY & MY \end{bmatrix}, \text{ and } \mathbf{B} \triangleq \begin{bmatrix} 0 \\ MLY \\ 0 \end{bmatrix}.$$

It follows that

$$\mathbf{S} = [\mathbf{I} - \mathbf{A}]^{-1} \mathbf{B}S_a \quad (33)$$

In addition,

$$S_b = \mathbf{G}^T \mathbf{S} \quad (34)$$

with $\mathbf{G}^T = [ML \ 0 \ 0]$.

From (33) and (34), we have

$$S_b = \mathbf{G}^T [\mathbf{I} - \mathbf{A}]^{-1} \mathbf{B}S_a \quad (35)$$

and the transfer function is obtained as

$$T(M, L, Y) \triangleq S_b / S_a = \mathbf{G}^T [\mathbf{I} - \mathbf{A}]^{-1} \mathbf{B} \quad (36)$$

By using

$$[\mathbf{I} - \mathbf{A}]^{-1} = \mathbf{I} + \mathbf{A} + \mathbf{A}^2 + \mathbf{A}^3 + \mathbf{A}^4 + \dots \quad (37)$$

we get

$$T(M, L, Y) = G^T B + G^T A^1 B + G^T A^2 B + G^T A^3 B + \dots \quad (38)$$

In particular, for (2,1,2) convolutional code with 16-QAM in Fig. 17,

$T(M, L, Y)$ is given by

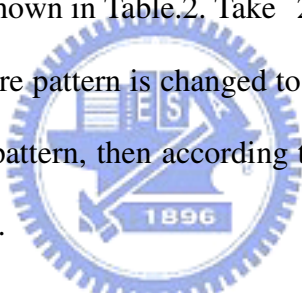
$$\begin{aligned}
T(M, L, Y) = & \\
& M^3 L^2 Y + M^2 L^2 Y^2 (L^2 + M^2) + M^3 L^2 Y^3 (3L^2 + M^2) + \\
& M^2 L^2 Y^4 (L^4 + 6M^2 L^2 + M^4) + M^3 L^2 Y^5 (5L^4 + 10M^2 L^2 + M^4) + \\
& M^2 L^2 Y^6 (L^6 + 15M^2 L^4 + 15M^4 L^2 + M^6) + \\
& M^3 L^2 Y^7 (7L^6 + 35M^2 L^4 + 21M^4 L^2 + M^6) + \\
& M^2 L^2 Y^8 (L^8 + 28M^2 L^6 + 70M^4 L^4 + 28M^6 L^2 + M^8) + \\
& M^3 L^2 Y^9 (9L^8 + 84M^2 L^6 + 126M^4 L^4 + 36M^6 L^2 + M^8) + \\
& M^2 L^2 Y^{10} (L^{10} + 45M^2 L^8 + 210M^4 L^6 + 210M^6 L^4 + 45M^8 L^2 + M^{10}) + \\
& M^3 L^2 Y^{11} (11L^{10} + 165M^2 L^8 + 462M^4 L^6 + 330M^6 L^4 + 55M^8 L^2 + M^{10}) + \\
& M^2 L^2 Y^{12} (L^{12} + 66M^2 L^{10} + 495M^4 L^8 + 924M^6 L^6 + 495M^8 L^4 + 66M^{10} L^2 + M^{12}) + \\
& M^3 L^2 Y^{13} (13L^{12} + 286M^2 L^{10} + 1287M^4 L^8 + 1716M^6 L^6 + 715M^8 L^4 + 78M^{10} L^2 + M^{12}) \dots
\end{aligned} \quad (39)$$

From (39) the total weight coefficients, $W_i(i, j)$ is obtained as

$$\begin{aligned}
\left. \frac{T(M, L, Y)}{dY} \right|_{Y=1} &= \sum_{i,j} W_i(i, j) M^i L^j = \\
& M^3 L^2 + M^2 L^2 (L^2 + M^2) + M^3 L^2 (3L^2 + M^2) + \\
& M^2 L^2 (L^4 + 6M^2 L^2 + M^4) + M^3 L^2 (5L^4 + 10M^2 L^2 + M^4) + \\
& M^2 L^2 (L^6 + 15M^2 L^4 + 15M^4 L^2 + M^6) + \\
& M^3 L^2 (7L^6 + 35M^2 L^4 + 21M^4 L^2 + M^6) + \\
& M^2 L^2 (L^8 + 28M^2 L^6 + 70M^4 L^4 + 28M^6 L^2 + M^8) + \\
& M^3 L^2 (9L^8 + 84M^2 L^6 + 126M^4 L^4 + 36M^6 L^2 + M^8) + \\
& M^2 L^2 (L^{10} + 45M^2 L^8 + 210M^4 L^6 + 210M^6 L^4 + 45M^8 L^2 + M^{10}) + \\
& M^3 L^2 (11L^{10} + 165M^2 L^8 + 462M^4 L^6 + 330M^6 L^4 + 55M^8 L^2 + M^{10}) + \\
& M^2 L^2 (L^{12} + 66M^2 L^{10} + 495M^4 L^8 + 924M^6 L^6 + 495M^8 L^4 + 66M^{10} L^2 + M^{12}) + \\
& M^3 L^2 (13L^{12} + 286M^2 L^{10} + 1287M^4 L^8 + 1716M^6 L^6 + 715M^8 L^4 + 78M^{10} L^2 + M^{12}) \dots
\end{aligned} \quad (40)$$

4.2. Modified Error State Diagram and Transfer Function with Puncturing

The error state diagram for punctured convolutional codes in [16] will be extended to a modified error state diagram that is able to enumerate the error positions in the m -bit labels. For example, with $k/n=1/2$ low rate encoder, the punctured pattern is showed in Fig.1 and it's size is $2 \times k$. The format and size of puncture pattern is the same in BICM-RLP system. But, in BICM-FLP labeling procedure, there are fixed correspondence between the output bits of the encoder and the label positions in turn. Therefore, the size of puncture pattern is changed to $2 \times (k \cdot K)$, where $K = \lceil m/2, n \rceil / n$, and this change causes the elements in the puncture pattern with equal number of different label positions. The puncture pattern with 16-QAM modulation is shown in Table.2. Take $2/3$ code-rate with 16-QAM as an example, the size of puncture pattern is changed to 2×4 and we have three MSB and LSB. With this puncture pattern, then according to [16], the modified error state diagram is shown as in Fig. 18.



Code rate	Puncture Pattern
1/2	$\begin{bmatrix} M \\ L \end{bmatrix}$
2/3	$\begin{bmatrix} M & M & L & L \\ L & \times & M & \times \end{bmatrix}$
3/4	$\begin{bmatrix} M & M & \times \\ L & \times & L \end{bmatrix}$

Table.2 Puncture pattern for the $2/3$ -rate and $3/4$ -rate codes with 16-QAM

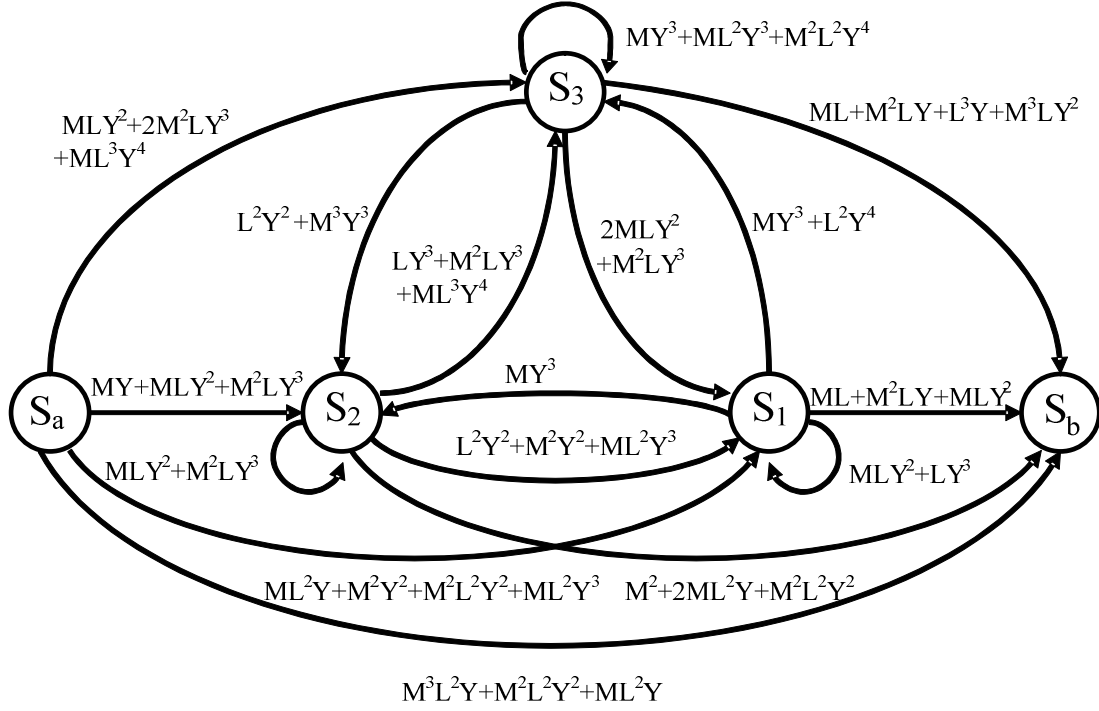


Fig.18 Modified error state diagram of (2,1,2), rate-2/3 punctured code with 16-QAM

Its matrix equations are given by

$$A = \begin{bmatrix} MLY^2 + LY^3 & L^2Y^2 + M^2Y^2 + ML^2Y^3 & 2MLY^2 + M^2LY^3 \\ MY^3 & MLY^2 + M^2LY^3 & L^2Y^2 + M^3Y^3 \\ MY^3 + L^2Y^4 & LY^3 + M^2LY^3 + ML^3Y^4 & MY^3 + ML^2Y^3 + M^2L^2Y^4 \end{bmatrix} \quad (41)$$

$$B = \begin{bmatrix} ML^2Y + M^2Y^2 + M^2L^2Y^2 + ML^2Y^3 \\ MY + MLY^2 + M^2LY^3 \\ MLY^2 + 2M^2LY^3 + ML^3Y^4 \end{bmatrix} \quad (42)$$

$$G^T = \begin{bmatrix} ML + M^2LY + MLY^2 & M^2 + 2ML^2Y + M^2L^2Y^2 & ML + M^2LY + L^3Y + M^3LY^2 \end{bmatrix} \quad (43)$$

$$h = M^3L^2Y + M^2L^2Y^2 + ML^2Y \quad (44)$$

where h is the transition cost directly from S_a to S_b

As adding the parameter h , the transfer function is changed to

$$T(M, L, Y) = S_b / S_a = h + G^T [I - A]^{-1} B \quad (45)$$

and hence

$$T(M, L, Y) = h + G^T B + G^T A^1 B + G^T A^2 B + G^T A^3 B + \dots \quad (46)$$

For (2,1,2)rate-3/4 puncture code with 16-QAM modulation, the state diagram is in Fig.19, and the relative matrices are in following equations.

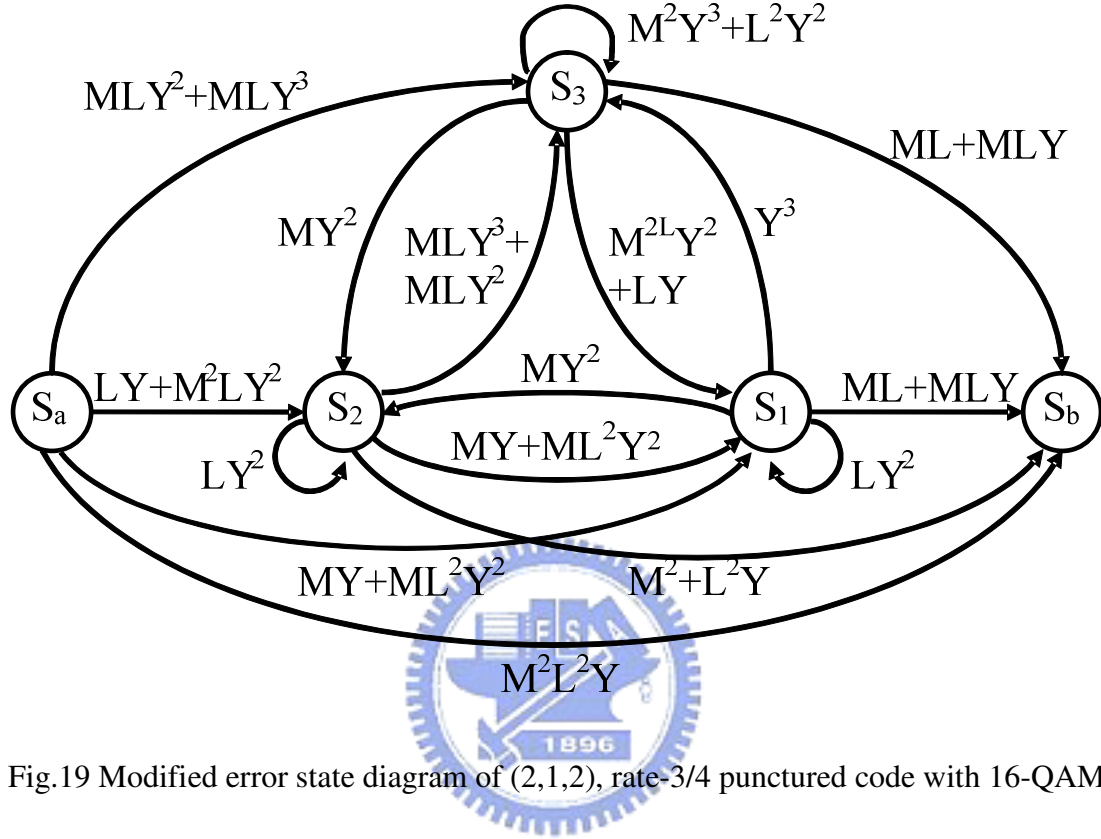


Fig.19 Modified error state diagram of (2,1,2), rate-3/4 punctured code with 16-QAM

$$\mathbf{A} = \begin{bmatrix} LY^2 & MLY^2 + MY & M^2LY^2 + LY \\ MY^2 & LY^2 & MY^2 \\ Y^3 & MLY^3 + MLY^2 & M^2Y^3 + L^2Y^2 \end{bmatrix} \quad (47)$$

$$\mathbf{B} = \begin{bmatrix} MY + ML^2Y^2 \\ LY + M^2LY^2 \\ MLY^2 + MLY^3 \end{bmatrix} \quad (48)$$

$$\mathbf{G}^T = [ML + MLY \quad M^2 + L^2Y \quad ML + MLY] \quad (49)$$

$$h = M^2L^2Y \quad (50)$$

We verify our result for 64-QAM modulation, and the similar calculation has been applied to the (2,1,2) convolutional code. The puncture pattern with 64-QAM modulation is in Table 3. With rate-1/2 code, the state diagram of the code is depicted in Fig.20, and its matrix equation is given by

$$\mathbf{A} = \begin{bmatrix} MLY^2 & CL^2Y^2 + MCY & ML^2Y^2 + C^2Y \\ LY^2 & MCY^2 & M^2Y^2 \\ MCY^3 & C^2LY^3 + MLY^2 & MCLY^3 + CLY^2 \end{bmatrix} \quad (51)$$

$$\mathbf{B} = \begin{bmatrix} MCLY + M^2CLY^2 \\ CLY + MCLY^2 \\ ML^2Y^2 + M^2C^2Y^3 \end{bmatrix} \quad (52)$$

$$\mathbf{G}^T = [MC + CL^2Y \quad M^2L + MC^2LY \quad MCL + M^2CLY] \quad (53)$$

$$h = MC^2L^2Y \quad (54)$$

With 64-QAM modulation, the transfer function is given by

$$T(M, C, L, Y) = S_b / S_a = h + \mathbf{G}^T [\mathbf{I} - \mathbf{A}]^{-1} \mathbf{B} \quad (55)$$

and hence

$$T(M, C, L, Y) = h + \mathbf{G}^T \mathbf{B} + \mathbf{G}^T \mathbf{A}^1 \mathbf{B} + \mathbf{G}^T \mathbf{A}^2 \mathbf{B} + \mathbf{G}^T \mathbf{A}^3 \mathbf{B} + \dots \quad (56)$$

Code rate	Puncture Pattern
1/2	$\begin{bmatrix} M & L & C \\ C & M & L \end{bmatrix}$
2/3	$\begin{bmatrix} M & L \\ C & \times \end{bmatrix}$
3/4	$\begin{bmatrix} M & L & \times & C & M & \times & L & C & \times \\ C & \times & M & L & \times & C & M & \times & L \end{bmatrix}$

Table.3 Puncture pattern for the 2/3-rate and 3/4-rate codes with 64-QAM

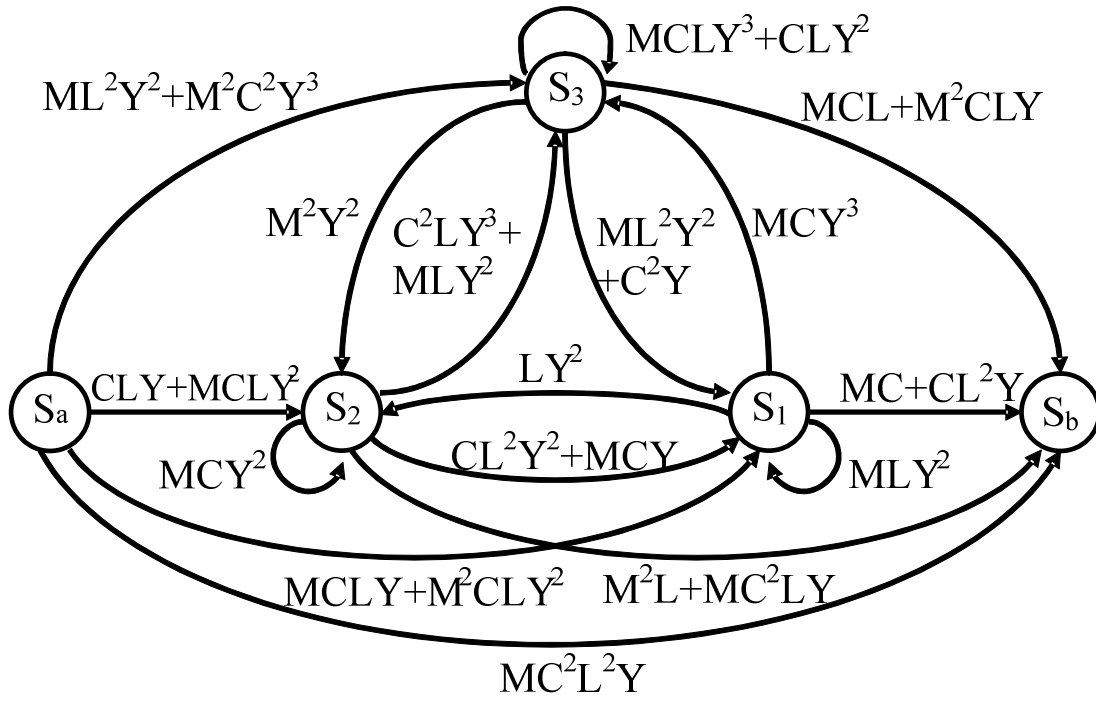
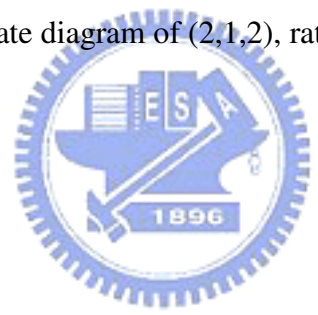


Fig.20 Modified error state diagram of (2,1,2), rate-1/2 code with 64-QAM



For (2,1,2) rate-2/3 puncture code with 64-QAM modulation, the state diagram is in Fig.21, and the relative matrices are in following equations.

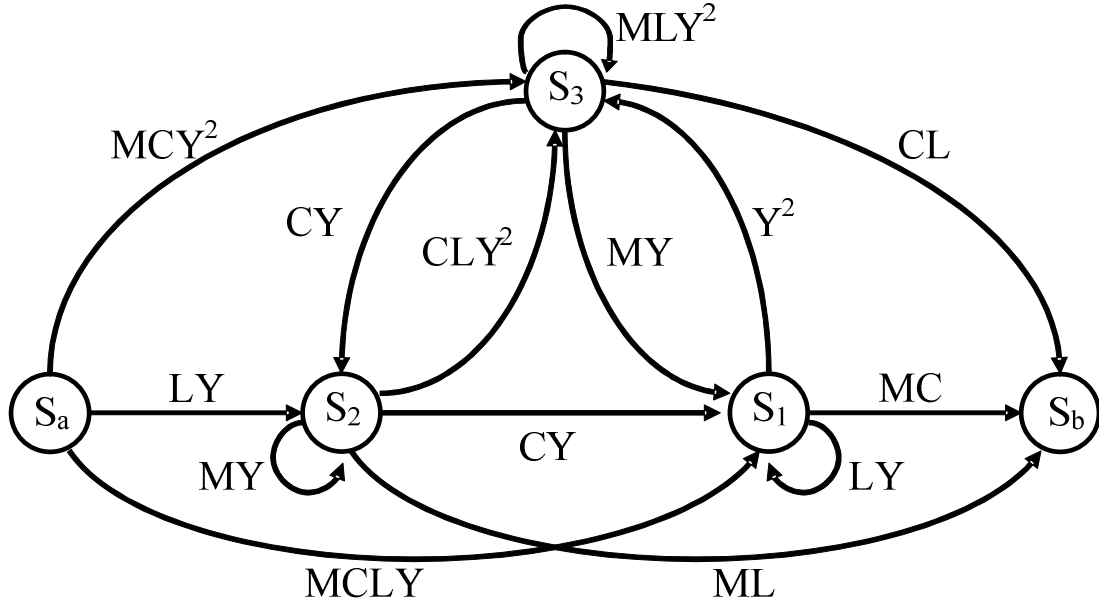


Fig.21 Modified error state diagram of (2,1,2), rate-2/3 punctured code with 64-QAM

$$\mathbf{A} = \begin{bmatrix} LY & CY & MY \\ 0 & MY & CY \\ Y^2 & CLY^2 & MLY^2 \end{bmatrix} \quad (57)$$

$$\mathbf{B} = \begin{bmatrix} MCLY \\ LY \\ MCY^2 \end{bmatrix} \quad (58)$$

$$\mathbf{G}^T = [MC \quad ML \quad CL] \quad (59)$$

It is easy to extend the scale punctured transfer function to higher QAM modulation with gray labeling, such as 256-QAM or 1024-QAM.

4.3 New Tighter Bound for QAM Constellation with Gray Labeling

The upper bound of BICM-FLP with scale transfer function is simpler. Since the sequences of label positions \underline{S} are determined in BICM-FLP system, the union bound of probability of bit error for convolutional codes of rate k/n becomes

$$p_b \leq \frac{1}{k \cdot K} \sum_{i,j,r} W_l(i, j, r) f_{new}(i, j, r, u, \chi) \quad (60)$$

where

$$\begin{aligned} f_{new}(i, j, r, u, \chi) &\triangleq E[P(\underline{c} \rightarrow \hat{\underline{c}})|\underline{U}] \\ &= 2^{-d} \sum_{\underline{U}} 2^{-d(m/2-1)} \sum_{\underline{x} \in \Psi_{\underline{c}}^S} \sum_{\underline{w} \in \Omega_{\underline{x}}^S} P(\underline{x} \rightarrow \underline{w}) \end{aligned} \quad (61)$$

where $W_l(i, j, r)$ is the total weight of error events at Hamming distance $d=i+j+r$ with i MSB, j center bit, and r LSB for 64-QAM and with i MSB, j LSB and $r=0$ for 16-QAM. Then, $k \cdot K$ is the column number in the punctured pattern, which means the number of error events counted at one transition branch on the state diagram.

4.3.1 Pairwise error probability with Soft-decision in AWGN channel

For 16-QAM with gray labeling in soft-decision decoding over AWGN channel, the PEP becomes

$$\begin{aligned} f_{new}(i, j, r, u, \chi) &= 2^{-d} \sum_{i_1=0}^i \binom{i}{i_1} \sum_{j_1=0}^j \binom{j}{j_1} \sum_{s=0}^{j_2} \binom{j_2}{s} \\ &\quad Q\left(\left\{3i_1 + i_2 + j_1 + [(j_2 - s) + 3s]\right\} \sqrt{\frac{4RE_b}{5dN_0}}\right) \end{aligned} \quad (62)$$

where (62) is similar with (22) without countering all possible label position.

For 64-QAM with gray labeling in soft-decision decoding, the PEP becomes

$$\begin{aligned}
& f_{new}(i, j, r, u, \chi) \\
&= 4^{-d} \sum_{i_1=0}^i \sum_{i_2=0}^{i-i_1} \sum_{i_3=0}^{i-i_1-i_2} \binom{i}{i_1} \binom{i-i_1}{i_2} \binom{i-i_1-i_2}{i_3} \\
& \quad \sum_{j_1=0}^j \sum_{j_2=0}^{j-j_1} \sum_{j_3=0}^{j-j_1-j_2} \binom{j}{j_1} \binom{j-j_1}{j_2} \binom{j-j_1-j_2}{j_3} \sum_{t=0}^{j_3} \binom{j_3}{t} \sum_{v=0}^{j_4} \binom{j_4}{v} \\
& \quad \sum_{r_1=0}^r \sum_{r_2=0}^{r-r_1} \sum_{r_3=0}^{r-r_1-r_2} \binom{r}{r_1} \binom{r-r_1}{r_2} \binom{r-r_1-r_2}{r_3} \sum_{s=0}^{r_2+r_3+r_4} \binom{r_2+r_3+r_4}{s} \\
& \quad Q \left(\left\{ \begin{aligned} & 7i_1 + 5i_2 + 3i_3 + i_4 + 3j_1 + j_2 + [(j_3 - t) + 7t] + \\ & [3(j_4 - v) + 5v] + [(r - s) + 3s] \end{aligned} \right\} \cdot \sqrt{\frac{2RE_b}{7dN_0}} \right)
\end{aligned} \tag{63}$$

where (63) is similar with (23) without countering all possible label position.

4.3.2 Pair-wise Error Probability with Soft-decision in Rayleigh Fading Channels

For 16-QAM with soft-decision in Rayleigh fading channel, The PEP is

$$f_{new}(i, j, r, u, \chi) \leq 2^{-d} \sum_{i_1=0}^i \binom{i}{i_1} \sum_{j_1=0}^j \binom{j}{j_1} \sum_{s=0}^{j_2} \binom{j_2}{s} \frac{1}{2} \left(\frac{1}{1+3^2 SNR} \right)^{i_1+s} \left(\frac{1}{1+SNR} \right)^{i_2+j_1+j_2-s} \tag{64}$$

where (64) is similar with (25) without countering all possible label position. And, for

64-QAM with soft-decision in Rayleigh fading channel, The PEP is

$$\begin{aligned}
& f_{new}(d, u, \chi) \\
& \leq 3^{-d} \sum_{i=0}^d \sum_{j=0}^{d-i} \binom{d}{i} \binom{d-i}{j} 4^{-d} \sum_{i_1=0}^i \sum_{i_2=0}^{i-i_1} \sum_{i_3=0}^{i-i_1-i_2} \binom{i}{i_1} \binom{i-i_1}{i_2} \binom{i-i_1-i_2}{i_3} \\
& \quad \sum_{j_1=0}^j \sum_{j_2=0}^{j-j_1} \sum_{j_3=0}^{j-j_1-j_2} \binom{j}{j_1} \binom{j-j_1}{j_2} \binom{j-j_1-j_2}{j_3} \sum_{t=0}^{j_3} \binom{j_3}{t} \sum_{v=0}^{j_4} \binom{j_4}{v} \\
& \quad \sum_{r_1=0}^r \sum_{r_2=0}^{r-r_1} \sum_{r_3=0}^{r-r_1-r_2} \binom{r}{r_1} \binom{r-r_1}{r_2} \binom{r-r_1-r_2}{r_3} \sum_{s=0}^{r_2+r_3+r_4} \binom{r_2+r_3+r_4}{s} \\
& \quad \frac{1}{2} \left(\frac{1}{1+7^2 SNR} \right)^{i_1+t} \left(\frac{1}{1+5^2 SNR} \right)^{i_2+v} \left(\frac{1}{1+3^2 SNR} \right)^{i_3+j_1+j_4-v+s} \left(\frac{1}{1+SNR} \right)^{i_4+j_2+j_3-t+r-s}
\end{aligned} \tag{65}$$

where (65) is similar with (26) without countering all possible label position.

4.4 Numerical Results

Numerical results for BICM-FLP are presented in this section. The BICM-FLP proposed in [3] is investigated specifically. Also, the performance comparison is made of BICM-RLP and BICM-FLP .

4.4.1 (2,1,6) Convolutional code

Numerical results for BICM-FLP based on (2,1,6) convolutional code are given in this section. Fig.22 and Fig.23 compare $BICM_{UB}$, $BICM_{EX}$ and $BICM_{NEW}$ for 16 QAM over AWGN and Rayleigh fading channels, respectively. Again, $BICM_{UB}$ is a quite a loose bound, $BICM_{EX}$ provide an accurate approximation, and the new $BICM_{NEW}$ is very tight, to within 0.5 dB for fading channels, for BER of practical interest. Fig.24 and Fig.25 give more numerical results, including those with 64QAM.

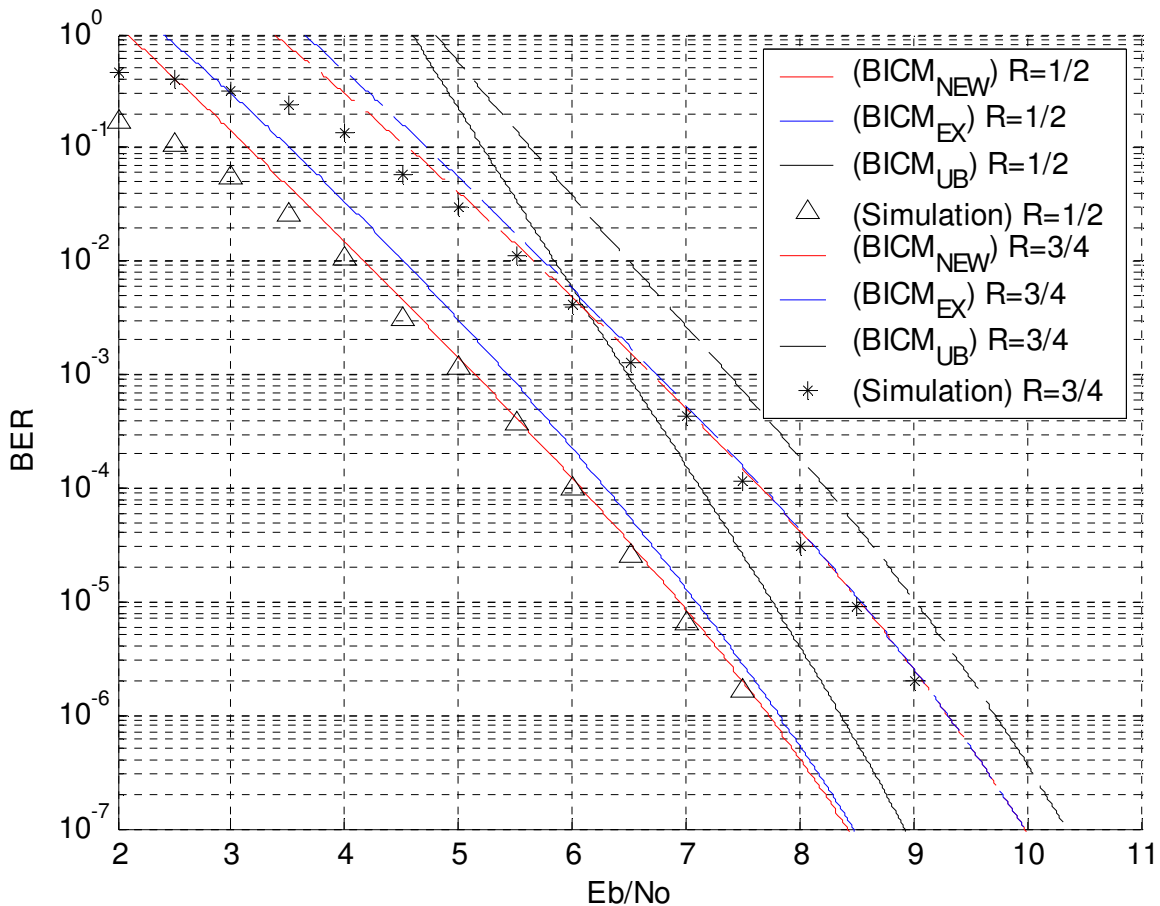


Fig.22 Performance of BICM-FLP in AWGN channels ($\kappa = 7$, 16 QAM)

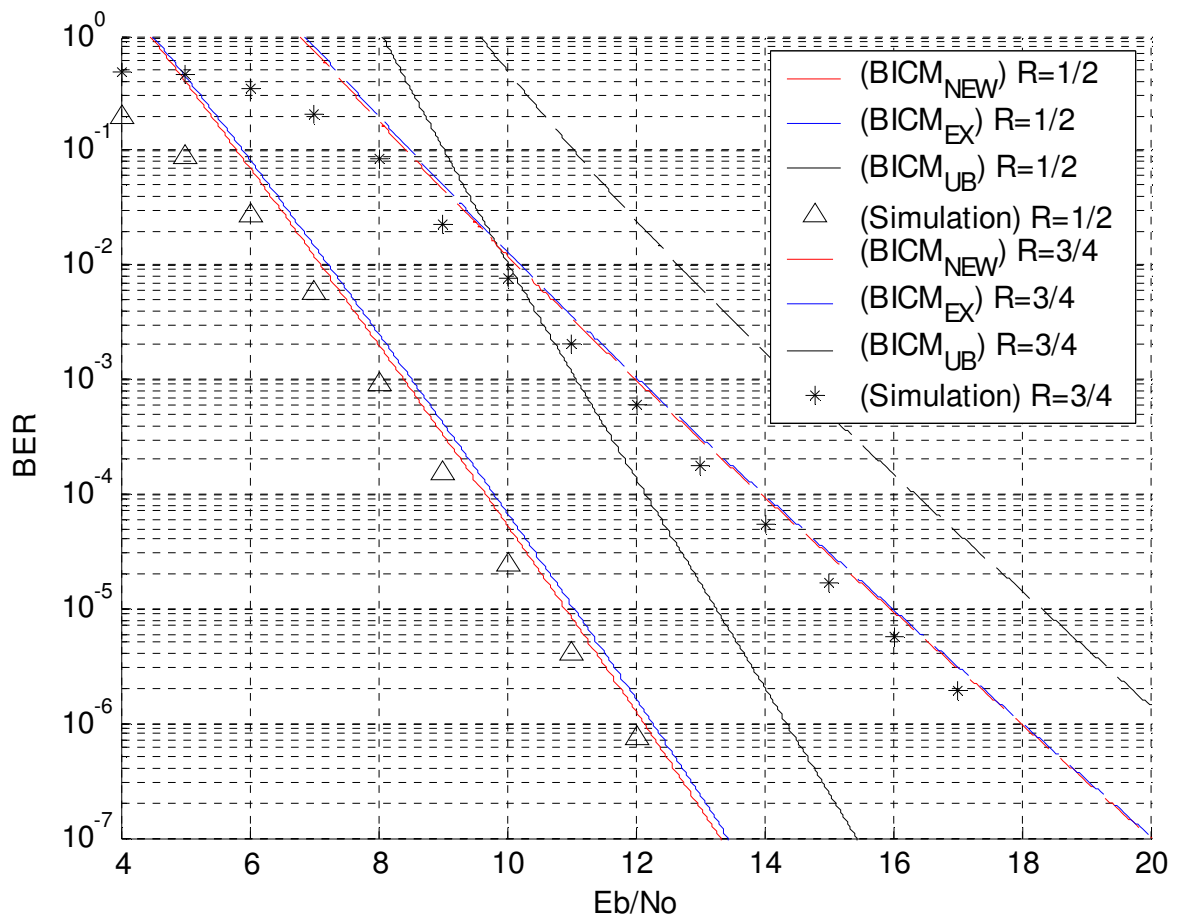


Fig.23 Performance of BICM-FLP in Rayleigh fading channels ($\kappa = 7$, 16 QAM)

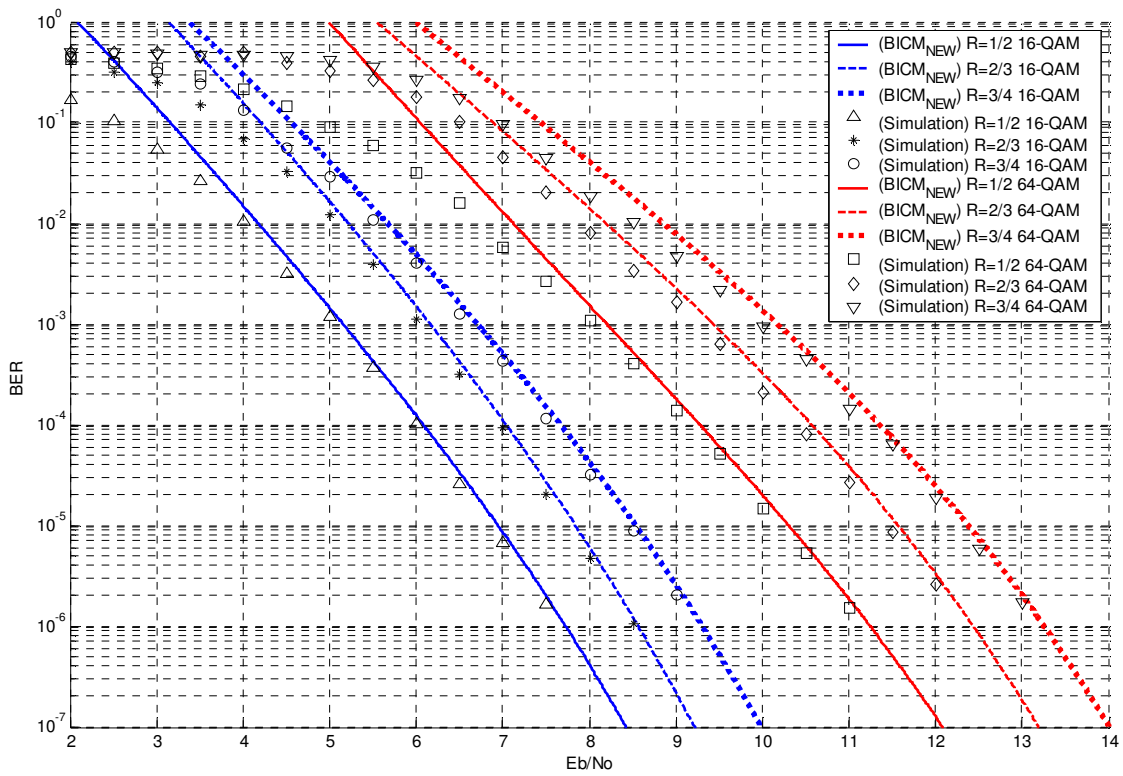


Fig.24 Performance of BICM-FLP in AWGN channels ($\kappa = 7, 16, 64$ QAM)



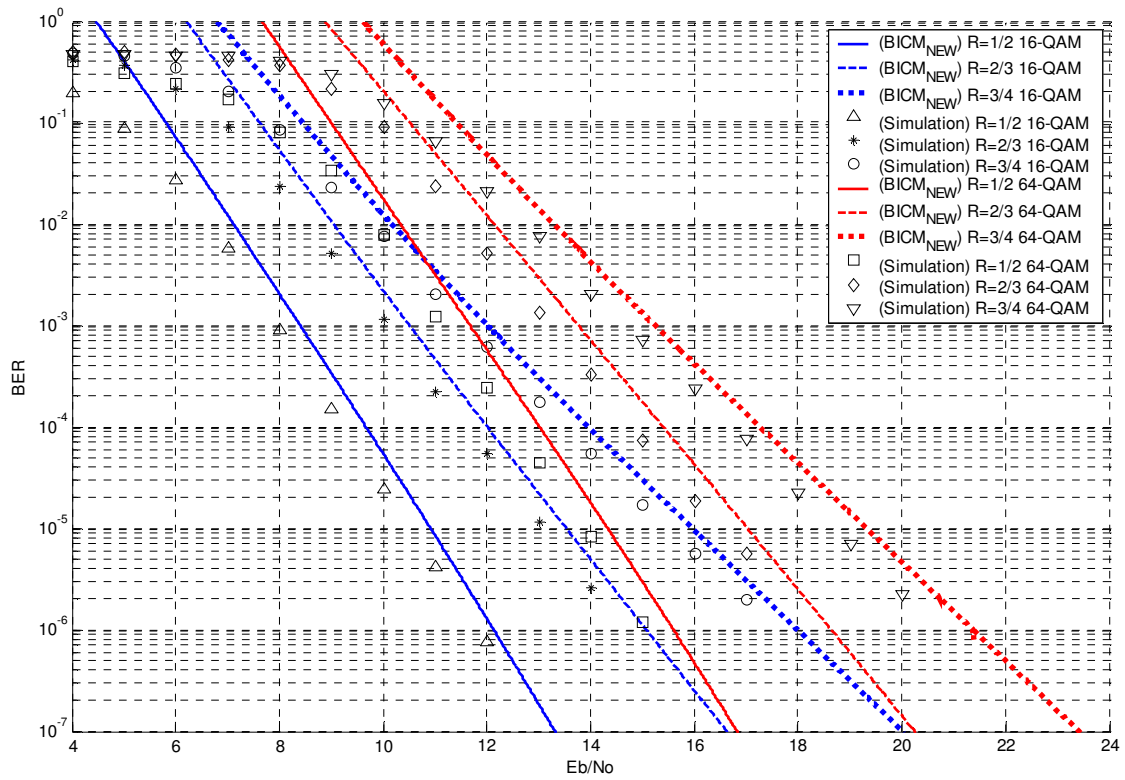


Fig.25 Performance of BICM-FLP in Rayleigh fading channels ($\kappa = 7$, 16,64 QAM).



4.4.2 (2,1,2) Convolutional code

Numerical results for BICM-FLP based on (2,1,2) convolutional code are given in this section. Fig.26 and Fig.27 compares $BICM_{UB}$, $BICM_{EX}$ and $BICM_{NEW}$ for 16QAM systems over AWGN and Rayleigh fading channels, respectively. Similar results are observed: $BICM_{UB}$ is a loose bound, $BICM_{EX}$ provides a good approximation, and $BICM_{NEW}$ is a very tight bound. More numerical results for this case are shown in Fig.28 and Fig.29.

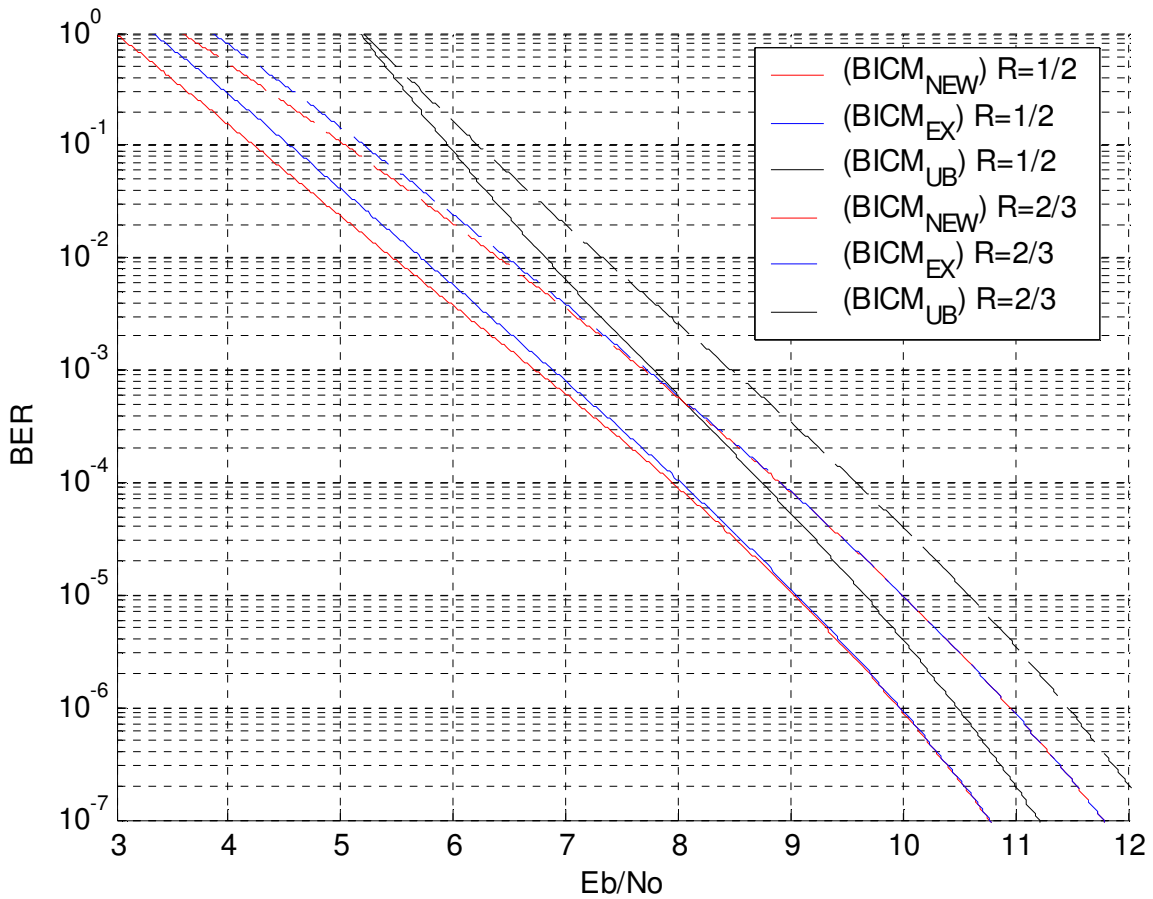


Fig.26 Performance of BICM-FLP in AWGN channels ($\kappa = 3$, 16QAM)

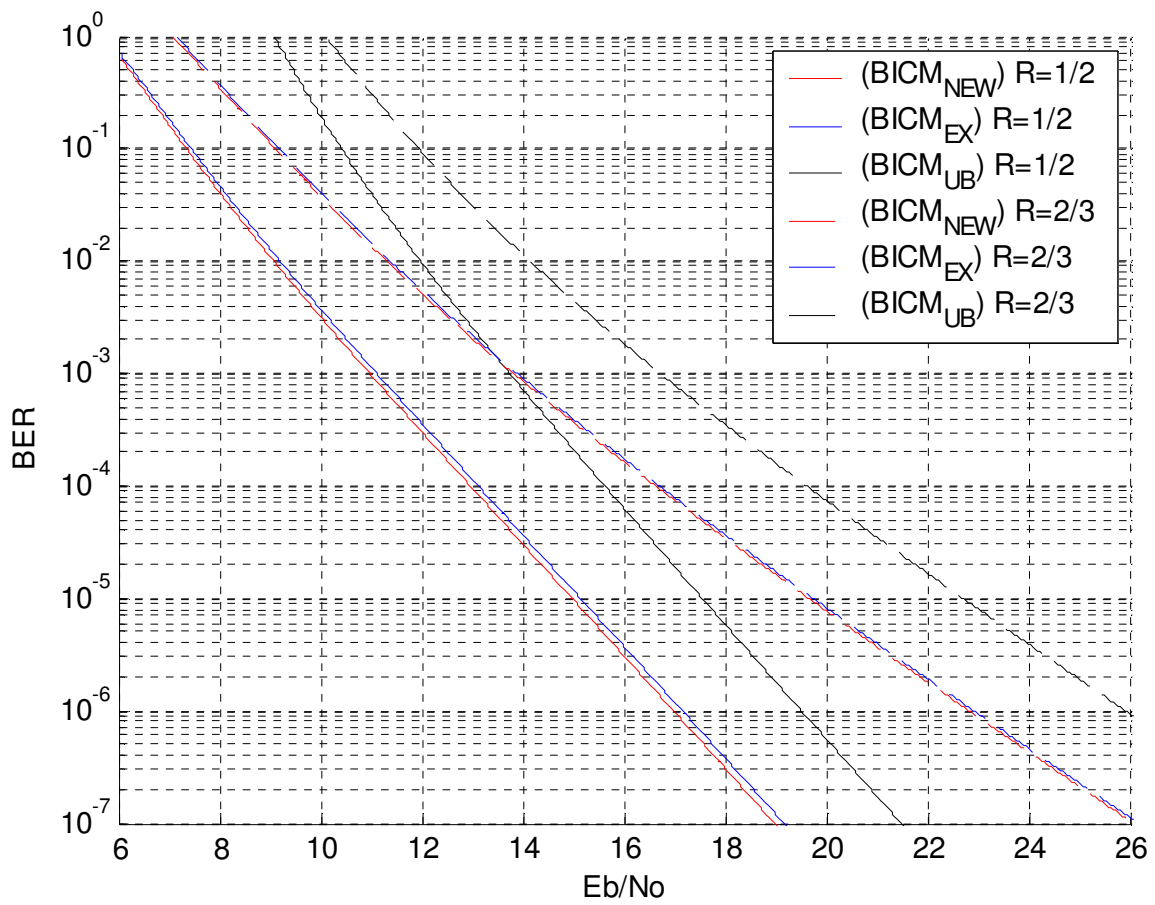


Fig.27 Performance of BICM-FLP in Rayleigh fading channels ($\kappa = 3$, 16QAM)

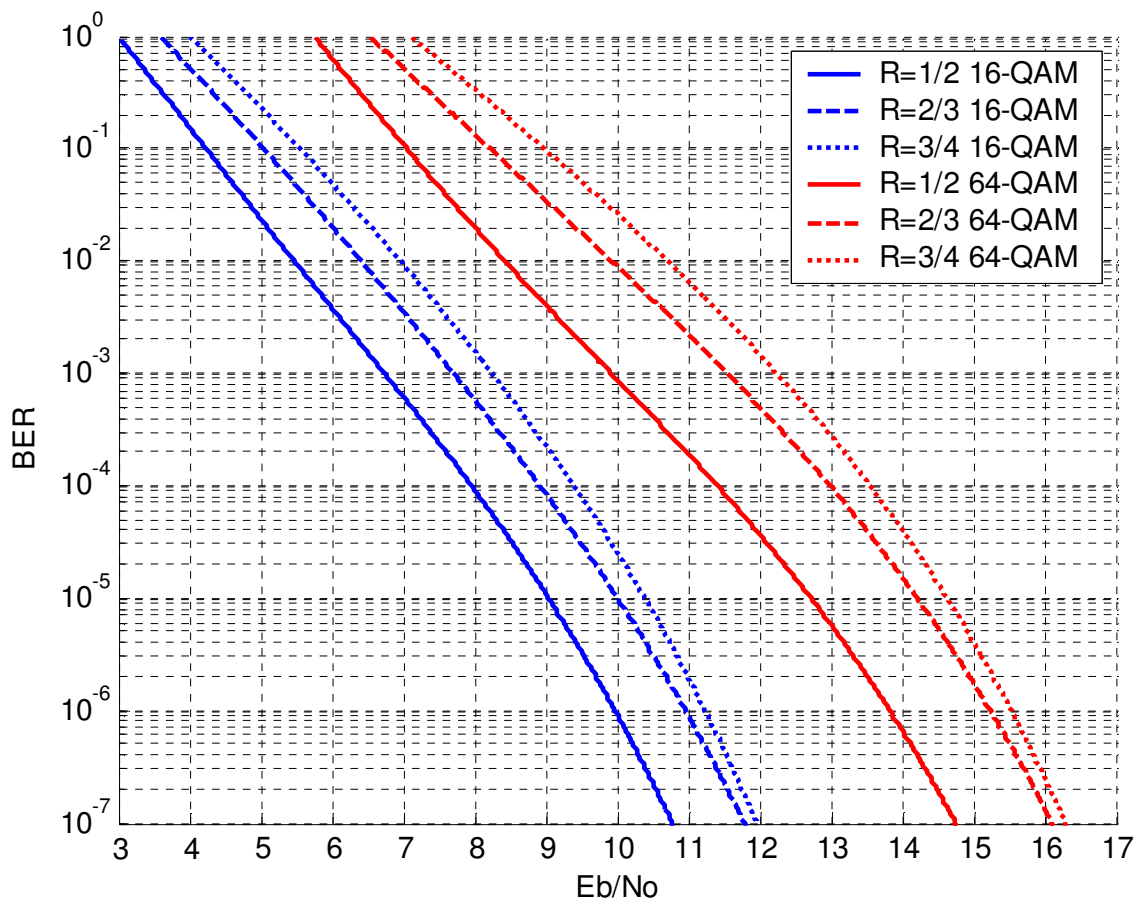


Fig.28 Performance of BICM-FLP in AWGN channels ($\kappa = 3, 16, 64$ QAM)

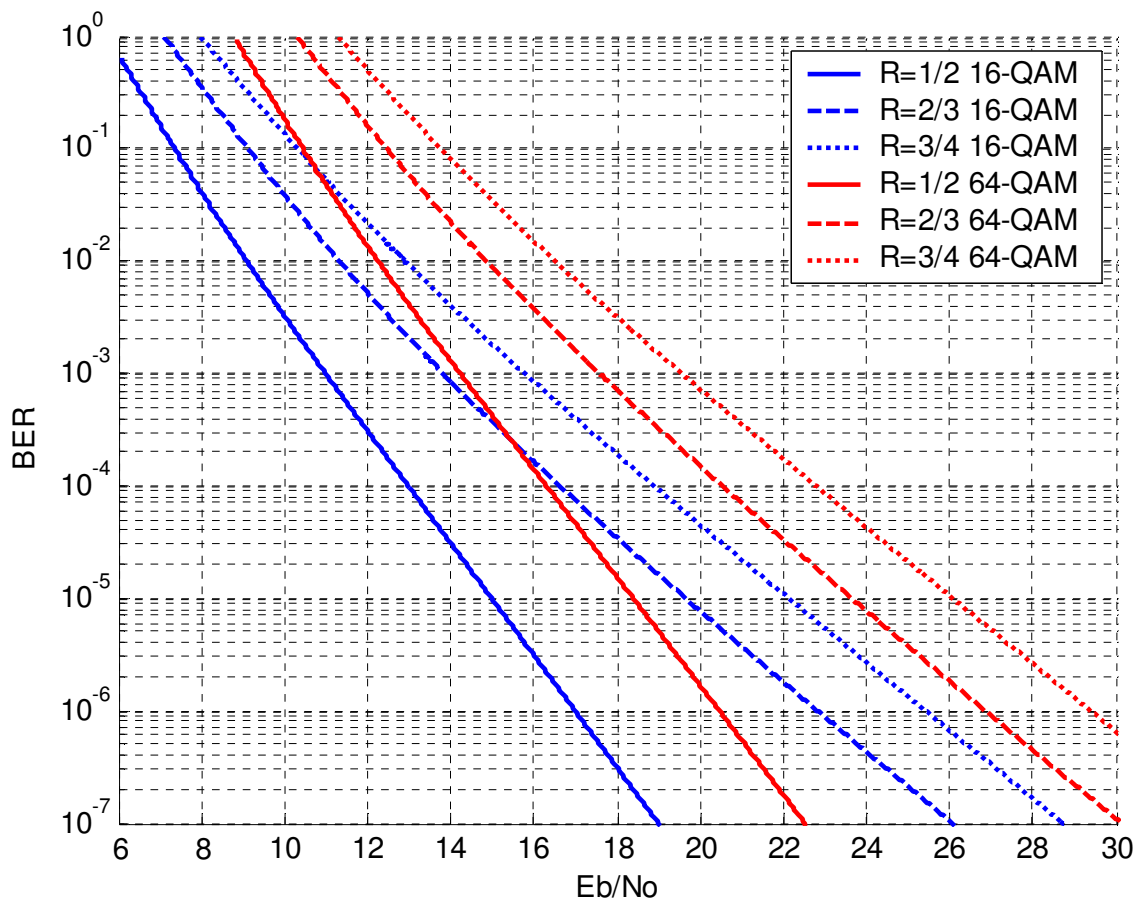


Fig.29 Performance of BICM-FLP in Rayleigh fading channels ($\kappa = 3$, 16,64 QAM).

4.4.3 Comparison of BICM-RLP and BICM-FLP

Figs.30, 31, and 32 show the performance comparisons between BICM-RLP and BICM-FLP for different channel conditions and system parameters. BICM-FLP has a slight better performance than BICM-RLP for all cases. This might be attributed to the fact that for BICM-RLP, a long runs of the coded sequence may be mapped to the less significant label bits of the m -bit label, and that degrades the system performance.

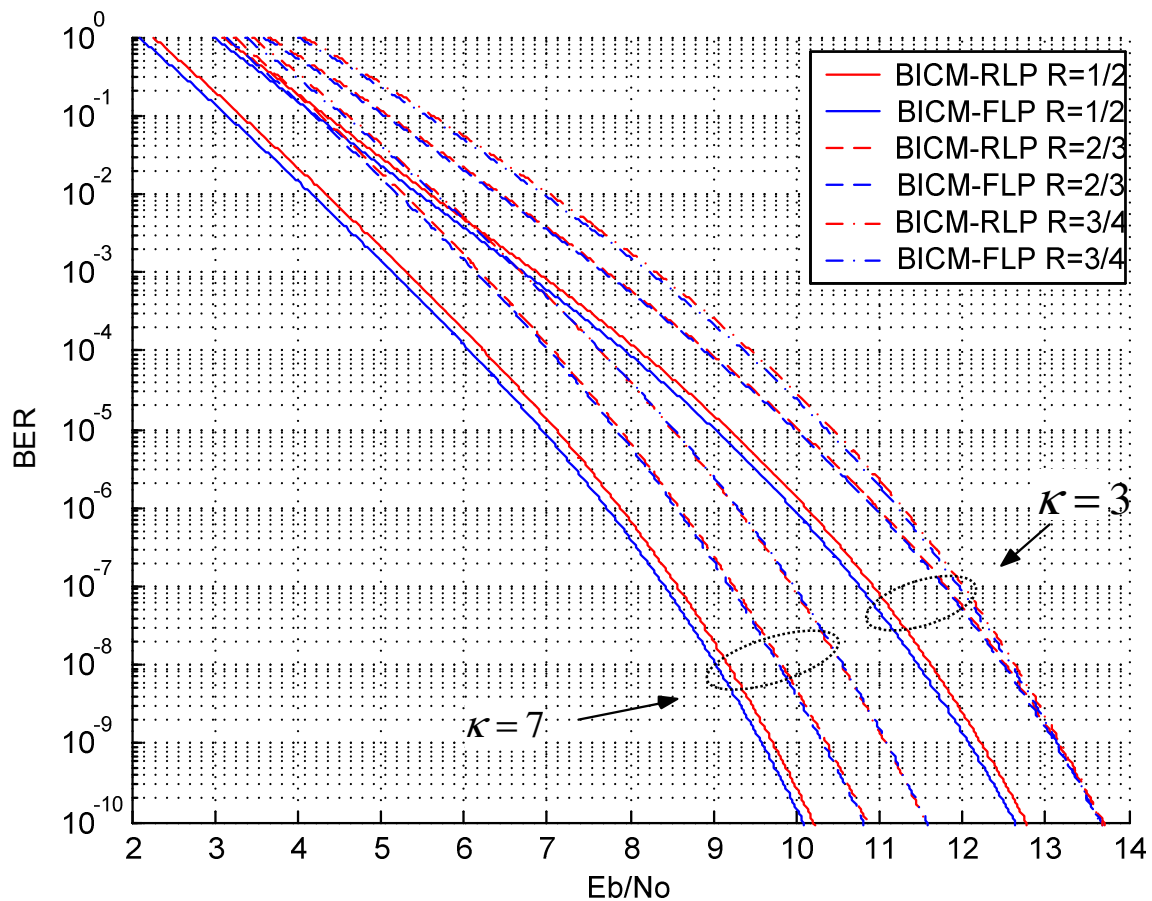


Fig.30 Performance comparison between BICM-RLP and BICM-FLP systems in AWGN channels ($\kappa = 3, 7, 16$ QAM)

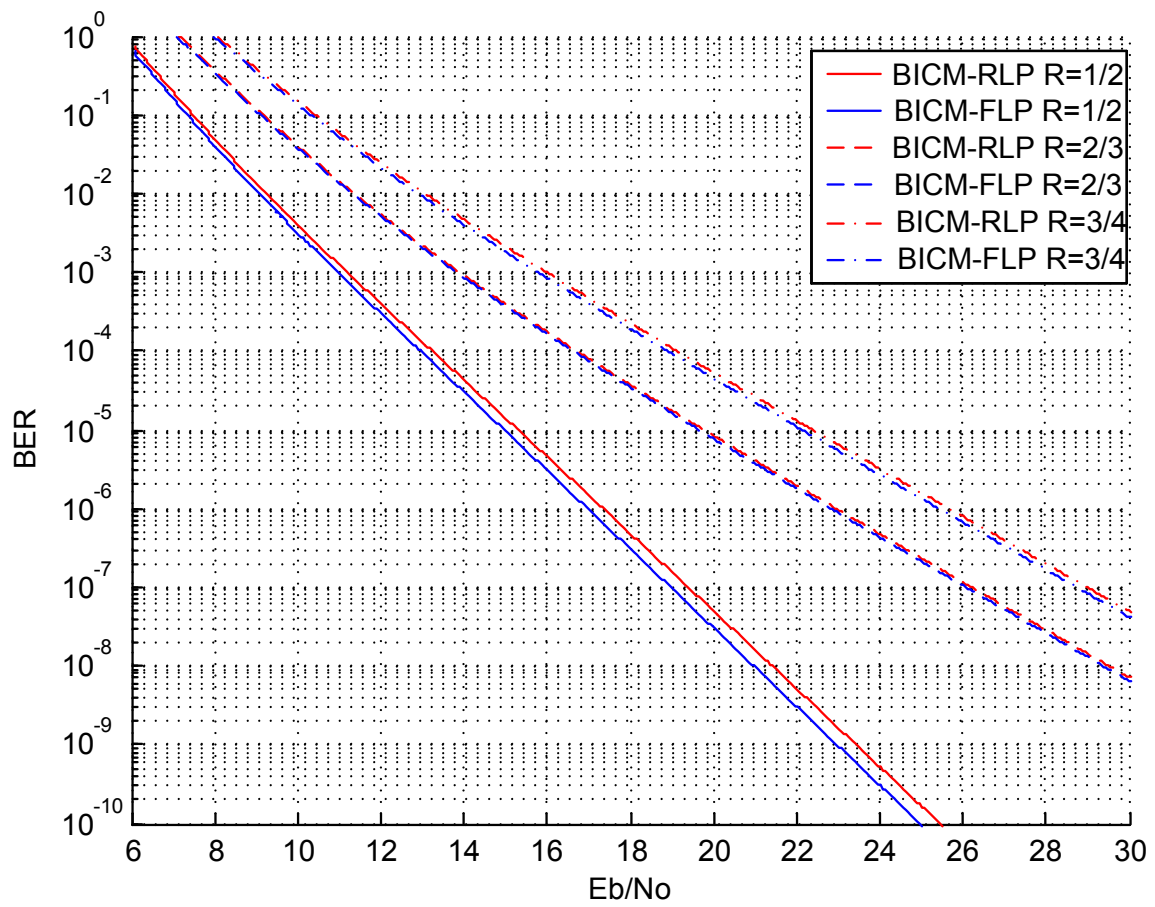


Fig.31 Performance comparison between BICM-RLP and BICM-FLP systems in Rayleigh fading channels ($\kappa = 3$, 16-QAM).

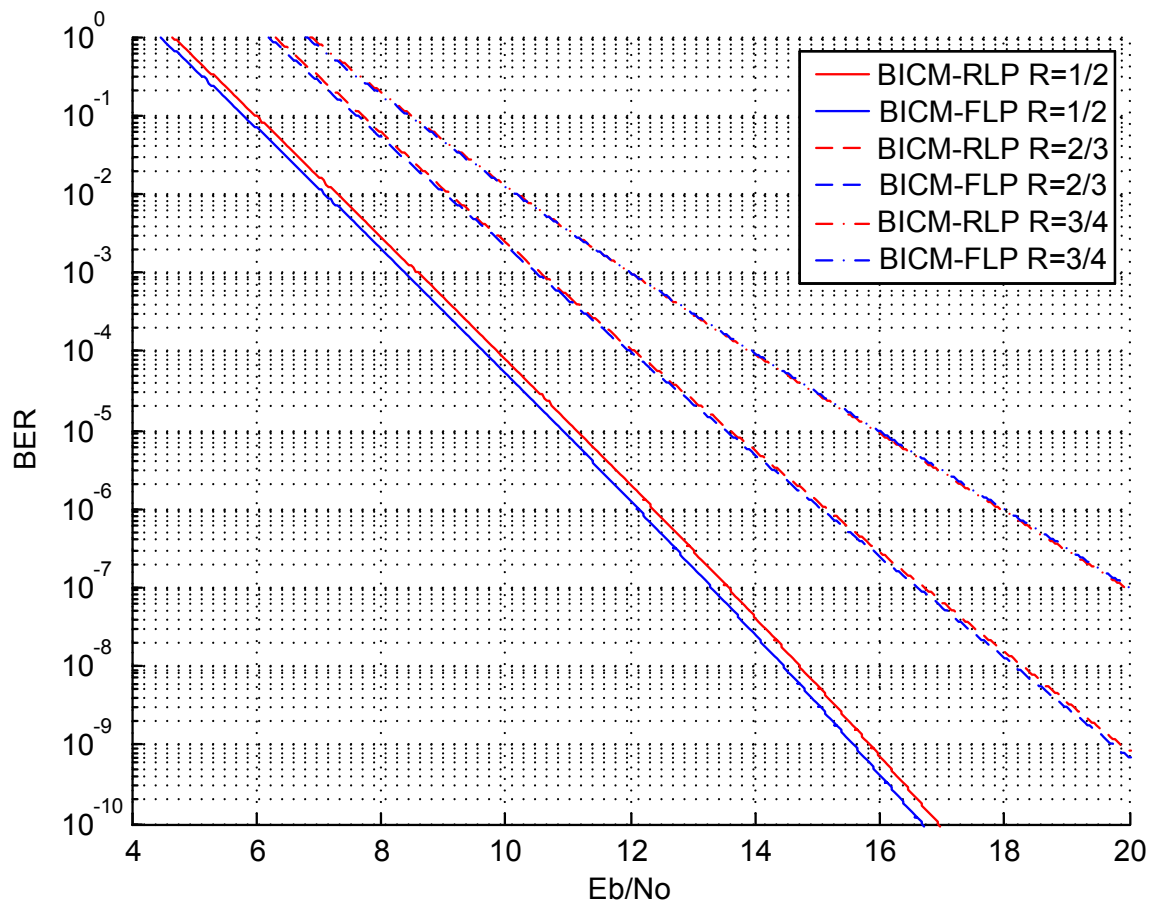


Fig.32 Performance comparison between BICM-RLP and BICM-FLP systems in Rayleigh fading channels ($\kappa = 7$, 16-QAM).

Chapter 5: Conclusions

In this thesis, we analyze the bit error rate performance of punctured bit-interleaved coded modulation systems with random label-position mapping (BICM-RLP) and fixed label-position mapping (BICM-FLP). New tighter BER bounds are proposed for QAM modulation with gray labeling over additive white Gaussian noise and Rayleigh fading channels. Both cases of soft and hard decoding are considered. For BICM-RLP with soft decoding, the new upper bound is tighter than the well-known BICM Union and the Expurgated Bound proposed in [4]. The tight upper bounds for hard decision and for BICM-FLP with soft decision are newly derived results.



Appendix A

BER Upper Bounds for BICM with hard decision

A. System model of BICM with hard decision

The system model for BICM system with hard decision is in Fig.33, where we replace bit metric calculation block with demodulation block. The coded bit error probabilities after demodulation are shown in Table.4 and Table.5. In AWGN channel and in Rayleigh fading channel, Table.5 and Table.6 shows the bit error probabilities from different constellation points with 16-QAM and 64-QAM modulation, which can be modeled as a combination of two orthogonal PAM signals.

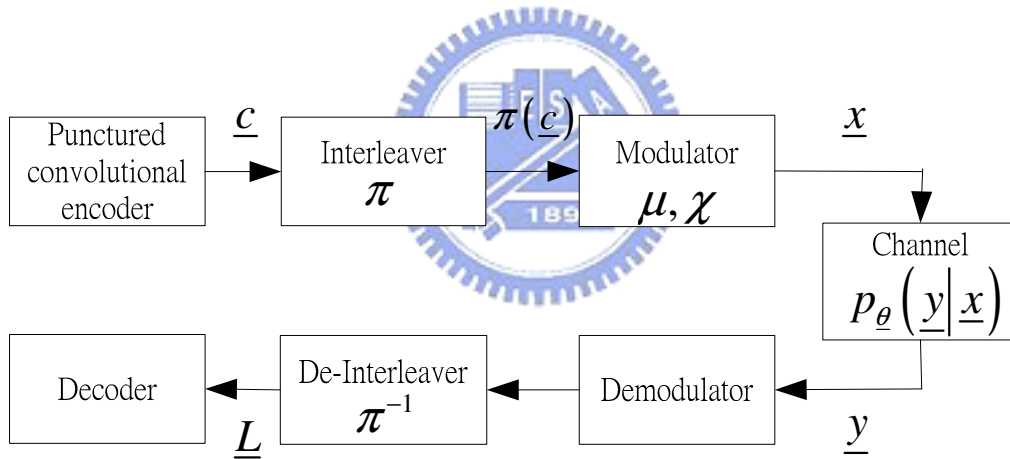


Fig.33 A block diagram of general BICM systems with hard decoding

B. Analytical model of BICM system with hard decision

We replace bitmetric calculation block with demodulation block in analytical model. The analytical models of BICM with random label-position and BICM with fixed label-position are shown in Fig.34 and Fig.35.

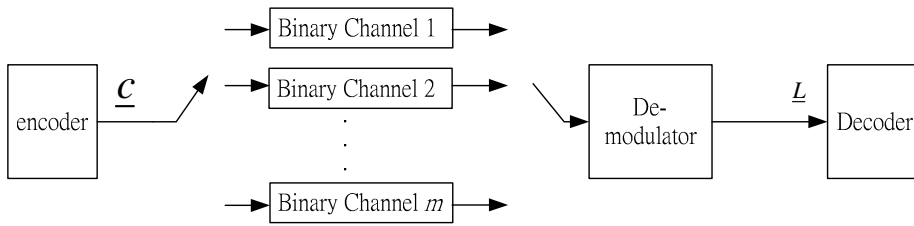


Fig.34 BICM with random label-position mapping with hard decoding .

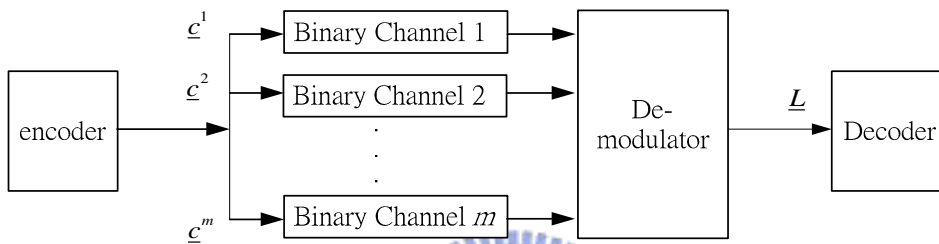


Fig.35 BICM with fixed label-position mapping with hard decoding

C. Decoding Rule

For total distinct coded bits, d , between the error sequence \underline{w} and the correct sequence \underline{x} , the pairwise error probability is that one-half or more of d bits are in error. Therefore, the correct path is abandoned.

D. Pairwise Error Probability of BICM-SI with hard-decision

The upper bound of BICM with random label position is

$$p_b \leq \frac{1}{k} \sum_{d=d_{\min}}^{\infty} W_l(d) f_{new}(d, u, \chi) \quad (66)$$

And, the upper bound of BICM with fixed label position is

$$p_b \leq \frac{1}{k \cdot K} \sum_{i,j,k} W_l(i, j, r) f_{new}(i, j, r, u, \chi) \quad (67)$$

Using 16-QAM with hard decision decoding, the PEP is that one-half or more of

d transmitted bits are in error. Therefore, the correct path is abandoned. Thus, the PEP with random label-position is shown in (68) and the PEP with fixed label-position is shown in (69)

$$\begin{aligned}
& f_{new}(d, u, \chi) \\
&= 2^{-d} \sum_{i=0}^d \binom{d}{i} \cdot \\
& \begin{cases} \sum_{h=(d+1)/2}^d \sum_{v=u(h-i)^*(h-i)}^{\min\{j,h\}} \binom{i}{h-v} \binom{j}{v} p_M^{h-v} (1-p_M)^{i-h+v} p_L^v (1-p_L)^{j-v} & \text{as } d \text{ odd} \\ \frac{1}{2} \sum_{v=u(d/2-i)^*(d/2-i)}^{\min\{j,d/2\}} \binom{i}{d/2-v} \binom{j}{v} p_M^{d/2-v} (1-p_M)^{i-d/2+v} p_L^v (1-p_L)^{j-v} + \\ \sum_{h=d/2+1}^d \sum_{v=u(h-i)^*(h-i)}^{\min\{j,h\}} \binom{i}{h-v} \binom{j}{v} p_M^{h-v} (1-p_M)^{i-h+v} p_L^v (1-p_L)^{j-v} & \text{as } d \text{ even} \end{cases} \quad (68)
\end{aligned}$$

$$\begin{aligned}
& f_{new}(i, j, r, u, \chi) \\
&= \begin{cases} \sum_{h=(d+1)/2}^d \sum_{v=u(h-i)^*(h-i)}^{\min\{j,h\}} \binom{i}{h-v} \binom{j}{v} p_M^{h-v} (1-p_M)^{i-h+v} p_L^v (1-p_L)^{j-v} & \text{as } d \text{ odd} \\ \frac{1}{2} \sum_{v=u(d/2-i)^*(d/2-i)}^{\min\{j,d/2\}} \binom{i}{d/2-v} \binom{j}{v} p_M^{d/2-v} (1-p_M)^{i-d/2+v} p_L^v (1-p_L)^{j-v} + \\ \sum_{h=d/2+1}^d \sum_{v=u(h-i)^*(h-i)}^{\min\{j,h\}} \binom{i}{h-v} \binom{j}{v} p_M^{h-v} (1-p_M)^{i-h+v} p_L^v (1-p_L)^{j-v} & \text{as } d \text{ even} \end{cases} \quad (69)
\end{aligned}$$

where $u(x) = \begin{cases} 1 & \text{if } x \geq 0 \\ 0 & \text{if } x < 0 \end{cases}$, $P_M = \frac{P_{M-1} + P_{M-2}}{2}$, and $P_L = \frac{P_{L-1} + P_{L-2}}{2}$.

The distinct coded bits $d = i + k$ between error sequence \underline{w} and correct sequence \underline{x} are with $\binom{d}{i}$ combinations of such distinct coded bits with i coded bits of MSB and j coded bits of LSB. For each case, we calculate h errors, which consist of $\binom{i}{h-v}$ combinations of i MSB with $h-v$ errors and $\binom{j}{v}$ combinations of j LSB with v errors. Table.4 shows the parameters of BER in AWGN channel and in Rayleigh fading channel.

Using hard decision decoding with 64-QAM, the PEP with random label-position is in (70) and the PEP with fixed label-position is in (71).

$$\begin{aligned}
f_{new}(d, u, \chi) &= 3^{-d} \sum_{i=0}^d \sum_{j=0}^{d-i} \binom{d}{i} \binom{d-i}{j}. \\
&\left\{ \begin{aligned} &\sum_{h=(d+1)/2}^d \sum_{v=u(h-i-j)^*(h-i-j)}^{\min\{r,h\}} \sum_{s=u(h-v-i)^*(h-v-i)}^{\min\{j,h-v\}} \binom{i}{h-v-s} \binom{j}{s} \binom{r}{v} \\ &\quad P_M^{h-v-s} (1-P_M)^{i-h+v+s} P_C^s (1-P_C)^{j-s} P_L^v (1-P_L)^{r-v} \quad \text{as } d \text{ odd} \\ &\frac{1}{2} \sum_{v=u(d/2-i-j)^*(d/2-i-j)}^{\min\{r,d/2\}} \sum_{s=u(d/2-v-i)^*(d/2-v-i)}^{\min\{j,d/2-v\}} \binom{i}{d/2-v-s} \binom{j}{s} \binom{r}{v} \\ &\quad P_M^{d/2-v-s} (1-P_M)^{i-d/2+v+s} P_C^s (1-P_C)^{j-s} P_L^v (1-P_L)^{r-v} \\ &+ \sum_{h=d/2+1}^d \sum_{v=u(h-i-j)^*(h-i-j)}^{\min\{r,h\}} \sum_{s=u(h-v-i)^*(h-v-i)}^{\min\{j,h-v\}} \binom{i}{h-v-s} \binom{j}{s} \binom{r}{v} \\ &\quad P_M^{h-v-s} (1-P_M)^{i-h+v+s} P_C^s (1-P_C)^{j-s} P_L^v (1-P_L)^{r-v} \quad \text{as } d \text{ even} \end{aligned} \right. \quad (70)
\end{aligned}$$

$$\begin{aligned}
f_{new}(i, j, r, u, \chi) &= \left\{ \begin{aligned} &\sum_{h=(d+1)/2}^d \sum_{v=u(h-i-j)^*(h-i-j)}^{\min\{r,h\}} \sum_{s=u(h-v-i)^*(h-v-i)}^{\min\{j,h-v\}} \binom{i}{h-v-s} \binom{j}{s} \binom{r}{v} \\ &\quad P_M^{h-v-s} (1-P_M)^{i-h+v+s} P_C^s (1-P_C)^{j-s} P_L^v (1-P_L)^{r-v} \quad \text{as } d \text{ odd} \\ &\frac{1}{2} \sum_{v=u(d/2-i-j)^*(d/2-i-j)}^{\min\{r,d/2\}} \sum_{s=u(d/2-v-i)^*(d/2-v-i)}^{\min\{j,d/2-v\}} \binom{i}{d/2-v-s} \binom{j}{s} \binom{r}{v} \\ &\quad P_M^{d/2-v-s} (1-P_M)^{i-d/2+v+s} P_C^s (1-P_C)^{j-s} P_L^v (1-P_L)^{r-v} \\ &+ \sum_{h=d/2+1}^d \sum_{v=u(h-i-j)^*(h-i-j)}^{\min\{r,h\}} \sum_{s=u(h-v-i)^*(h-v-i)}^{\min\{j,h-v\}} \binom{i}{h-v-s} \binom{j}{s} \binom{r}{v} \\ &\quad P_M^{h-v-s} (1-P_M)^{i-h+v+s} P_C^s (1-P_C)^{j-s} P_L^v (1-P_L)^{r-v} \quad \text{as } d \text{ even} \end{aligned} \right. \quad (71)
\end{aligned}$$

where $P_M = \frac{P_{M-1} + P_{M-2} + P_{M-3} + P_{M-4}}{4}$, $P_C = \frac{P_{C-1} + P_{C-2} + P_{C-3} + P_{C-4}}{4}$, and

$P_L = \frac{P_{L-1} + P_{L-2} + P_{L-3} + P_{L-4}}{4}$. The distinct coded bits $d = i + j + r$ between error

sequence \underline{w} and correct sequence \underline{x} are with $\binom{d}{i} \binom{d-i}{j}$ combinations of such

distinct coded bits with i coded bits of MSB, j coded bits of center bit, and r coded

bits of LSB. For each case, we calculate h errors, which consist of $\binom{i}{h-v-s}$ combinations of i MSB with $h-v-s$ errors, $\binom{j}{s}$ combinations of j LSB with s errors, and $\binom{r}{v}$ combinations of r LSB with v errors. Table.5 shows the parameters of BER in AWGN channel and in Rayleigh fading channel.

	Transmitted PAM signal	AWGN channel	Rayleigh Fading channel
P_{L_1}	MSB ± 3 00 01	$Q\left(\sqrt{\frac{4RE_b}{5N_0}}\right) - Q\left(5\sqrt{\frac{4RE_b}{5N_0}}\right)$	$\frac{1}{2}\left(1 - \sqrt{\frac{2RE_b/5N_0}{1+2RE_b/5N_0}}\right) - \frac{1}{2}\left(1 - \sqrt{\frac{10RE_b/N_0}{1+10RE_b/N_0}}\right)$
P_{L_2}	MSB ± 1 11 10	$Q\left(\sqrt{\frac{4RE_b}{5N_0}}\right) + Q\left(3\sqrt{\frac{4RE_b}{5N_0}}\right)$	$\frac{1}{2}\left(1 - \sqrt{\frac{2RE_b/5N_0}{1+2RE_b/5N_0}}\right) + \frac{1}{2}\left(1 - \sqrt{\frac{18RE_b/5N_0}{1+18RE_b/5N_0}}\right)$
P_{M_1}	LSB ± 3 00 01	$Q\left(3\sqrt{\frac{4RE_b}{5N_0}}\right)$	$\frac{1}{2}\left(1 - \sqrt{\frac{18RE_b/5N_0}{1+18RE_b/5N_0}}\right)$
P_{M_2}	LSB ± 1 11 10	$Q\left(\sqrt{\frac{4RE_b}{5N_0}}\right)$	$\frac{1}{2}\left(1 - \sqrt{\frac{2RE_b/5N_0}{1+2RE_b/5N_0}}\right)$

Table.4 Coded bit error probabilities table of 16-QAM modulation

	Transmitted PAM signal	AWGN channel	Rayleigh Fading channel
P_{M-1}	MSB ± 7 100 000	$Q\left(7\sqrt{\frac{2RE_b}{7N_0}}\right)$	$\frac{1}{2}\left(1-\sqrt{\frac{7RE_b/N_0}{1+7RE_b/N_0}}\right)$
P_{M-2}	MSB ± 5 101 001	$Q\left(5\sqrt{\frac{2RE_b}{7N_0}}\right)$	$\frac{1}{2}\left(1-\sqrt{\frac{25RE_b/7N_0}{1+25RE_b/7N_0}}\right)$
P_{M-3}	MSB ± 3 111 011	$Q\left(3\sqrt{\frac{2RE_b}{7N_0}}\right)$	$\frac{1}{2}\left(1-\sqrt{\frac{9RE_b/7N_0}{1+9RE_b/7N_0}}\right)$
P_{M-4}	MSB ± 1 110 010	$Q\left(\sqrt{\frac{2RE_b}{7N_0}}\right)$	$\frac{1}{2}\left(1-\sqrt{\frac{RE_b/7N_0}{1+RE_b/7N_0}}\right)$
P_{C-1}	Center bit ± 7 100 000	$Q\left(3\sqrt{\frac{2RE_b}{7N_0}}\right)-Q\left(11\sqrt{\frac{2RE_b}{7N_0}}\right)$	$\frac{1}{2}\left(1-\sqrt{\frac{9RE_b/7N_0}{1+9RE_b/7N_0}}\right)-\frac{1}{2}\left(1-\sqrt{\frac{121RE_b/7N_0}{1+121RE_b/7N_0}}\right)$
P_{C-2}	Center bit ± 5 101 001	$Q\left(\sqrt{\frac{2RE_b}{7N_0}}\right)-Q\left(9\sqrt{\frac{2RE_b}{7N_0}}\right)$	$\frac{1}{2}\left(1-\sqrt{\frac{RE_b/7N_0}{1+RE_b/7N_0}}\right)-\frac{1}{2}\left(1-\sqrt{\frac{81RE_b/7N_0}{1+81RE_b/7N_0}}\right)$
P_{C-3}	Center bit ± 3 111 011	$Q\left(\sqrt{\frac{2RE_b}{7N_0}}\right)+Q\left(7\sqrt{\frac{2RE_b}{7N_0}}\right)$	$\frac{1}{2}\left(1-\sqrt{\frac{RE_b/7N_0}{1+RE_b/7N_0}}\right)+\frac{1}{2}\left(1-\sqrt{\frac{49RE_b/7N_0}{1+49RE_b/7N_0}}\right)$
P_{C-4}	Center bit ± 1 110 010	$Q\left(3\sqrt{\frac{2RE_b}{7N_0}}\right)+Q\left(5\sqrt{\frac{2RE_b}{7N_0}}\right)$	$\frac{1}{2}\left(1-\sqrt{\frac{9RE_b/7N_0}{1+9RE_b/7N_0}}\right)+\frac{1}{2}\left(1-\sqrt{\frac{25RE_b/7N_0}{1+25RE_b/7N_0}}\right)$
P_{L-1}	LSB ± 7 100 000	$Q\left(\sqrt{\frac{2RE_b}{7N_0}}\right)+Q\left(9\sqrt{\frac{2RE_b}{7N_0}}\right)$ $-Q\left(5\sqrt{\frac{2RE_b}{7N_0}}\right)-Q\left(13\sqrt{\frac{2RE_b}{7N_0}}\right)$	$\frac{1}{2}\left(1-\sqrt{\frac{RE_b/7N_0}{1+RE_b/7N_0}}\right)+\frac{1}{2}\left(1-\sqrt{\frac{81RE_b/7N_0}{1+81RE_b/7N_0}}\right)$ $-\frac{1}{2}\left(1-\sqrt{\frac{25RE_b/7N_0}{1+25RE_b/7N_0}}\right)-\frac{1}{2}\left(1-\sqrt{\frac{169RE_b/7N_0}{1+169RE_b/7N_0}}\right)$
P_{L-2}	LSB ± 5 101 001	$Q\left(\sqrt{\frac{2RE_b}{7N_0}}\right)+Q\left(3\sqrt{\frac{2RE_b}{7N_0}}\right)$ $+Q\left(11\sqrt{\frac{2RE_b}{7N_0}}\right)-Q\left(7\sqrt{\frac{2RE_b}{7N_0}}\right)$	$\frac{1}{2}\left(1-\sqrt{\frac{RE_b/7N_0}{1+RE_b/7N_0}}\right)+\frac{1}{2}\left(1-\sqrt{\frac{9RE_b/7N_0}{1+9RE_b/7N_0}}\right)$ $+\frac{1}{2}\left(1-\sqrt{\frac{121RE_b/7N_0}{1+121RE_b/7N_0}}\right)-\frac{1}{2}\left(1-\sqrt{\frac{49RE_b/7N_0}{1+49RE_b/7N_0}}\right)$
P_{L-3}	LSB ± 3 111 011	$Q\left(\sqrt{\frac{2RE_b}{7N_0}}\right)+Q\left(3\sqrt{\frac{2RE_b}{7N_0}}\right)$ $+Q\left(9\sqrt{\frac{2RE_b}{7N_0}}\right)-Q\left(5\sqrt{\frac{2RE_b}{7N_0}}\right)$	$\frac{1}{2}\left(1-\sqrt{\frac{RE_b/7N_0}{1+RE_b/7N_0}}\right)+\frac{1}{2}\left(1-\sqrt{\frac{9RE_b/7N_0}{1+9RE_b/7N_0}}\right)$ $+\frac{1}{2}\left(1-\sqrt{\frac{81RE_b/7N_0}{1+81RE_b/7N_0}}\right)-\frac{1}{2}\left(1-\sqrt{\frac{25RE_b/7N_0}{1+25RE_b/7N_0}}\right)$
P_{L-4}	LSB ± 1 110 010	$Q\left(\sqrt{\frac{2RE_b}{7N_0}}\right)+Q\left(3\sqrt{\frac{2RE_b}{7N_0}}\right)$ $-Q\left(5\sqrt{\frac{2RE_b}{7N_0}}\right)-Q\left(7\sqrt{\frac{2RE_b}{7N_0}}\right)$	$\frac{1}{2}\left(1-\sqrt{\frac{RE_b/7N_0}{1+RE_b/7N_0}}\right)+\frac{1}{2}\left(1-\sqrt{\frac{9RE_b/7N_0}{1+9RE_b/7N_0}}\right)$ $-\frac{1}{2}\left(1-\sqrt{\frac{25RE_b/7N_0}{1+25RE_b/7N_0}}\right)-\frac{1}{2}\left(1-\sqrt{\frac{7RE_b/N_0}{1+7RE_b/N_0}}\right)$

Table.5 Coded bit error probabilities table of 64-QAM modulation

E. Numerical Results

Numerical results for BICM-FLP and BICM-RLP with hard decoding are presented in this section.

E.1 (2,1,6) Convolutional code

Numerical results for BICM-RLP based on (6,1,2) convolutional code are given in Fig.36 and Fig.37, which includes simulation results and BICM_{NEW} over AWGN and Rayleigh fading channels, respectively. BICM_{NEW} is a very tight bound. The same numerical results for BICM-FLP are shown in Fig.38 and Fig.39. We can find that the coding gain of soft decision contrasting with hard decision is about 3dB with 16-QAM modulation, and about 3.5 dB with 64-QAM modulation.

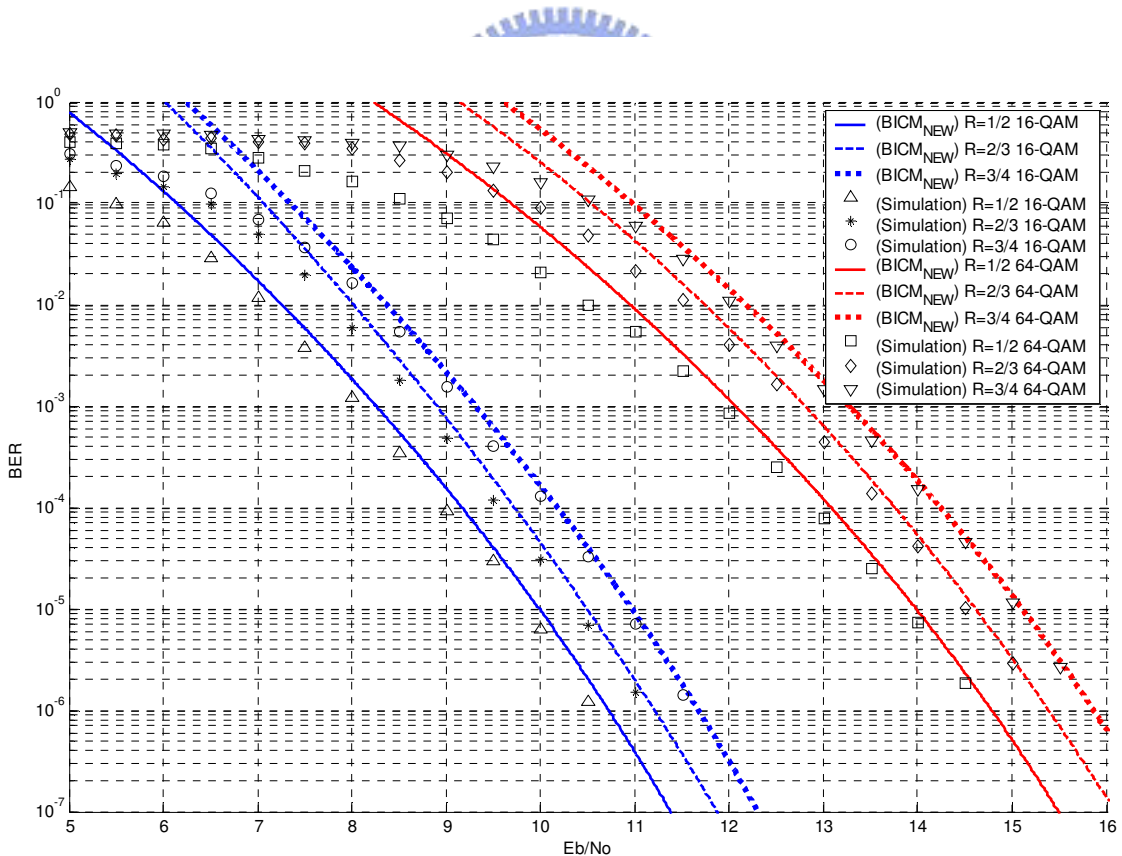


Fig.36 Performance of BICM-RLP with hard decoding in AWGN channels ($\kappa = 7$, 16,64 QAM).

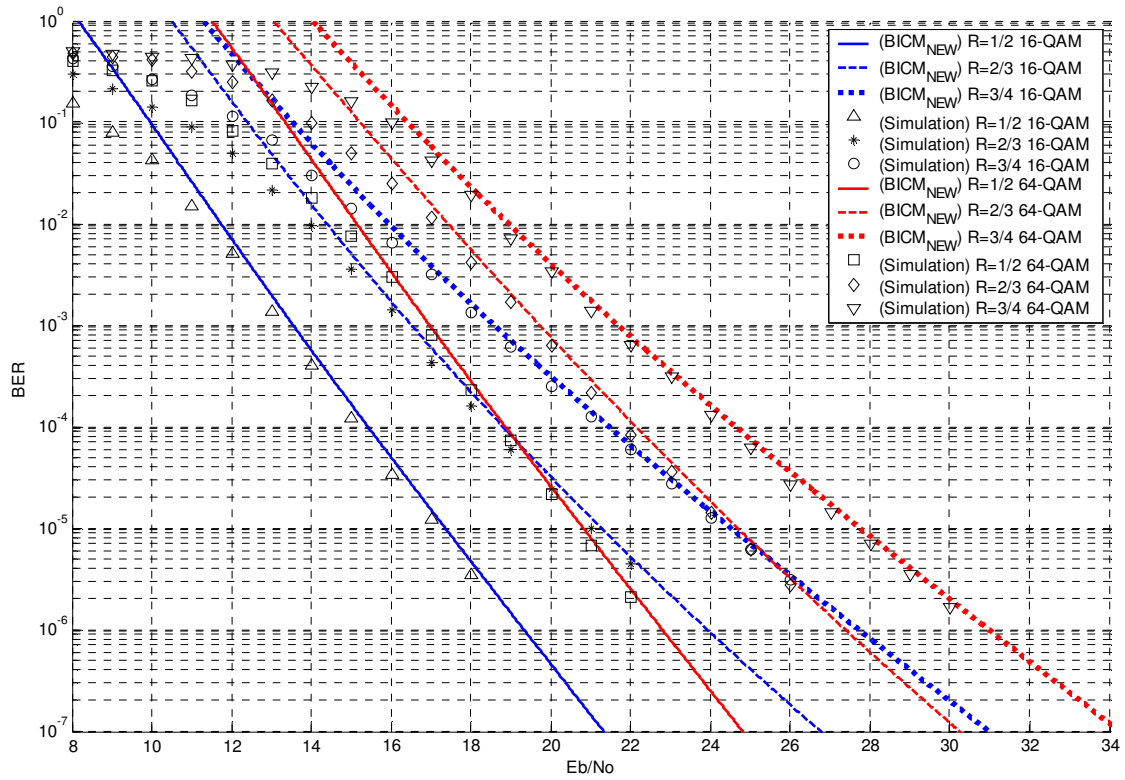


Fig.37 Performance of BICM-RLP with hard decoding in Rayleigh fading channels ($\kappa = 7, 16, 64$ QAM).



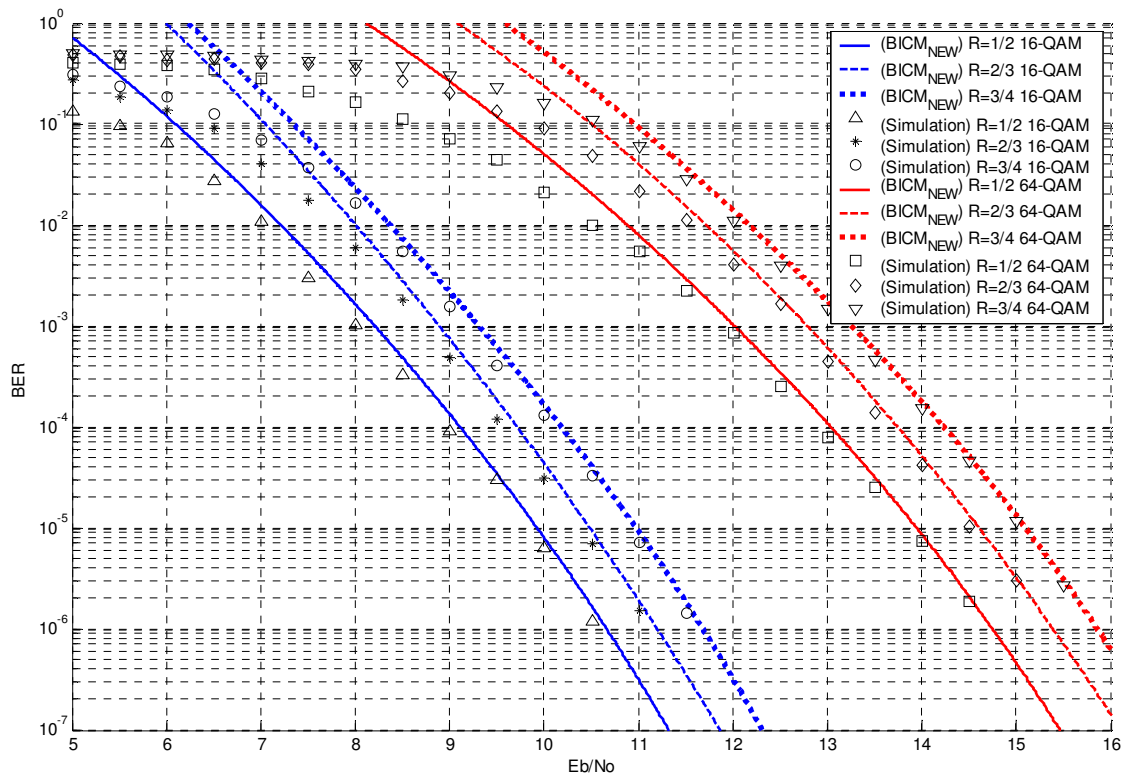


Fig.38 Performance of BICM-FLP with hard decoding in AWGN channels ($\kappa = 7$, 16,64 QAM).



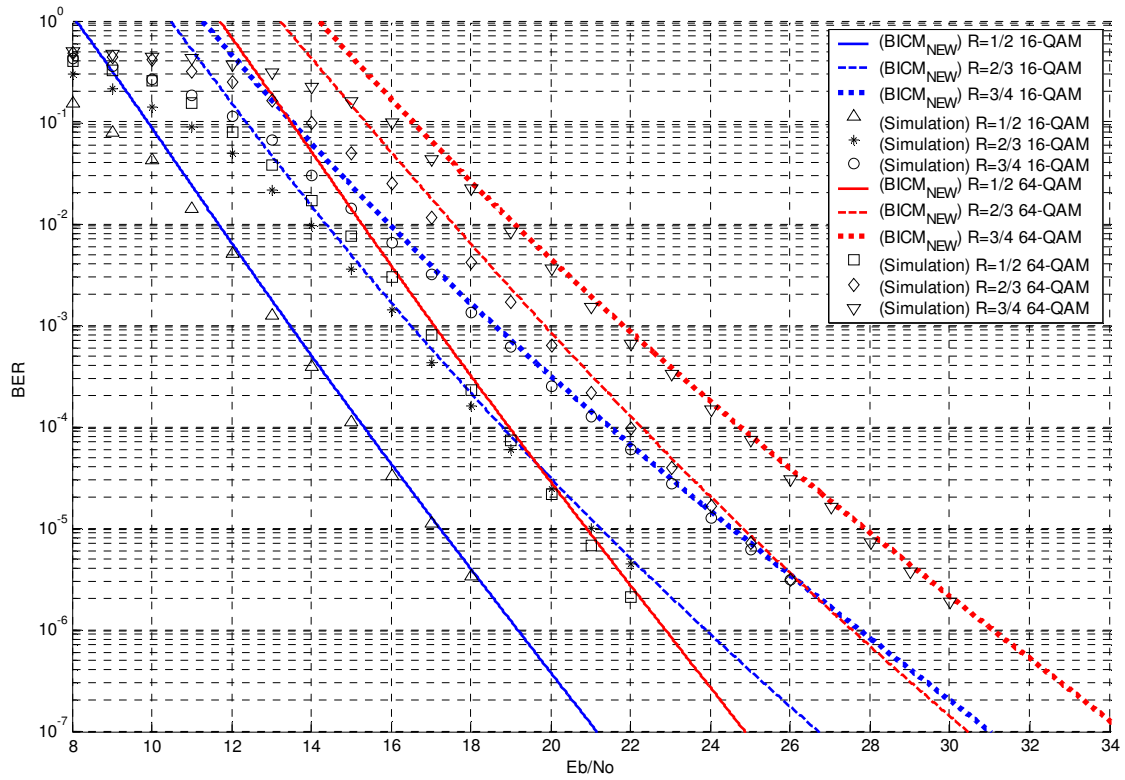


Fig.39 Performance of BICM-FLP with hard decoding in Rayleigh fading channels
 ($\kappa = 7, 16, 64$ QAM).



E.2 (2,1,2) Convolutional code

Numerical results for BICM-RLP based on (6,1,2) convolutional code are given in Fig.40 and Fig.41, which includes BICM_{NEW} over AWGN and Rayleigh fading channels, respectively. BICM_{NEW} is a very tight bound. The same numerical results for BICM-FLP are shown in Fig.42 and Fig.43.

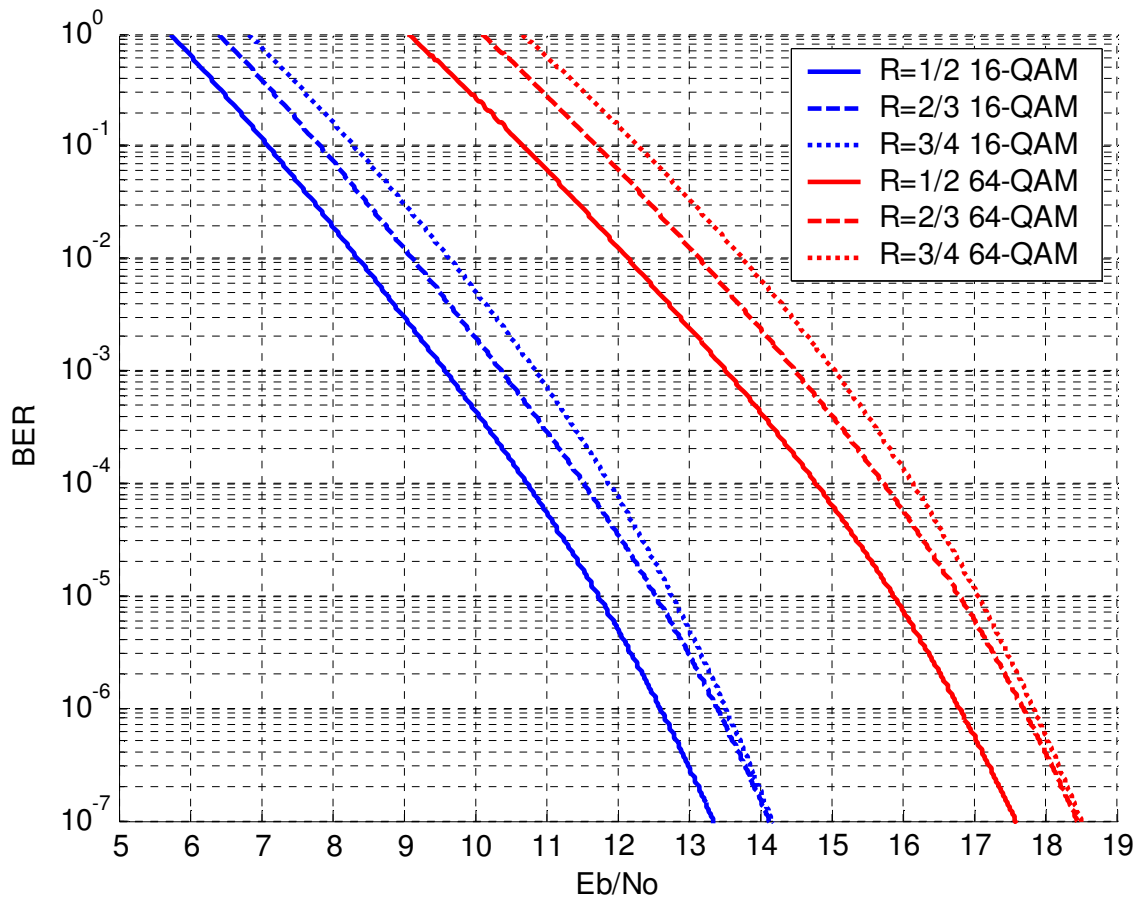


Fig.40 Performance of BICM-RLP with hard decoding in AWGN channels ($\kappa = 3$, 16,64 QAM).

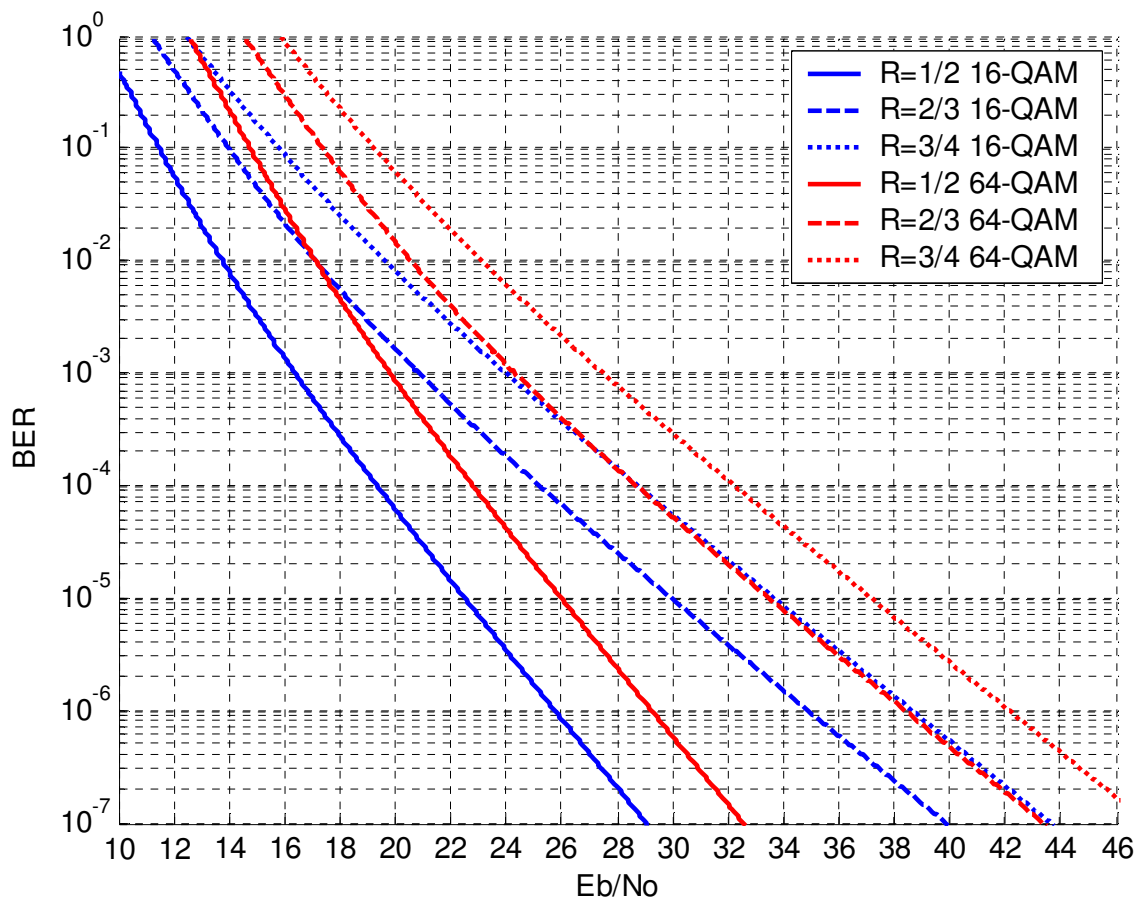


Fig.41 Performance of BICM-RLP with hard decoding in Rayleigh fading channels
 ($\kappa = 3$, 16,64 QAM).

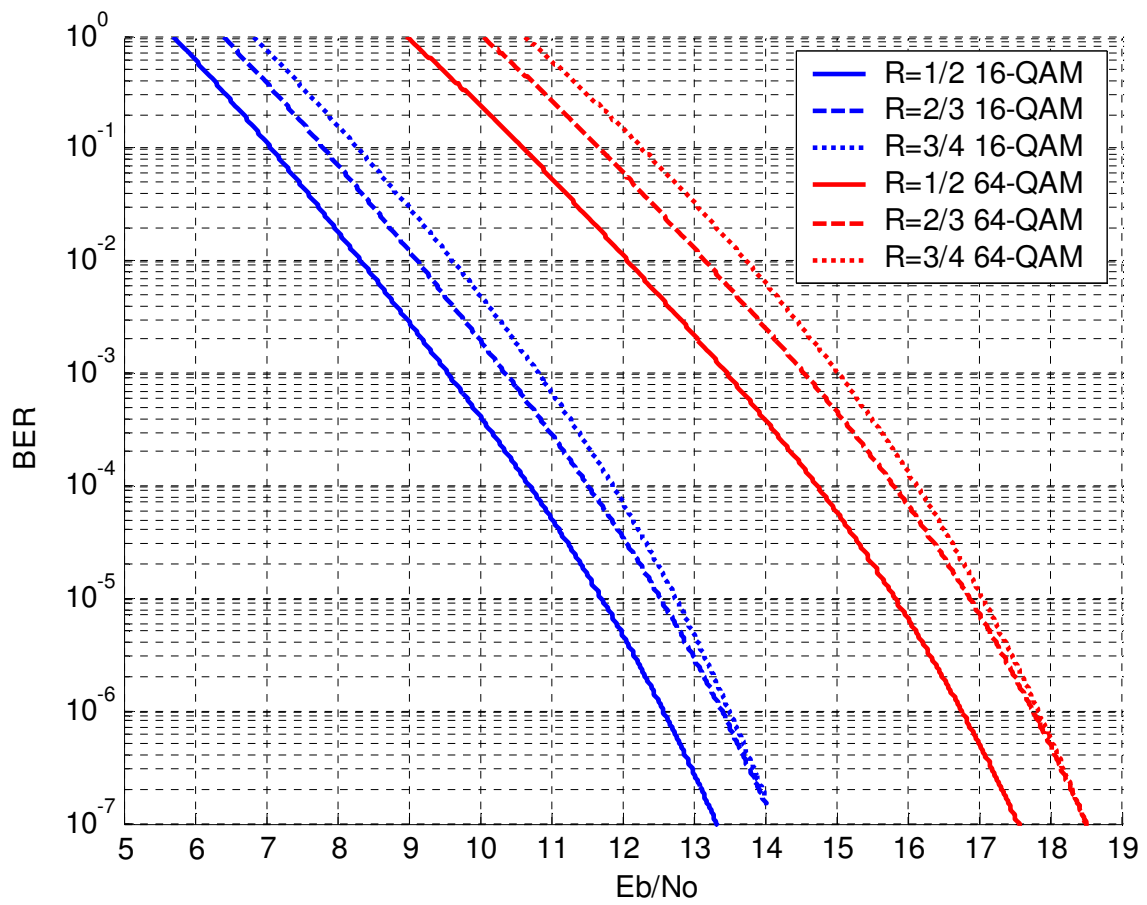


Fig.42 Performance of BICM-FLP with hard decoding in AWGN channels ($\kappa = 3$, 16,64 QAM).

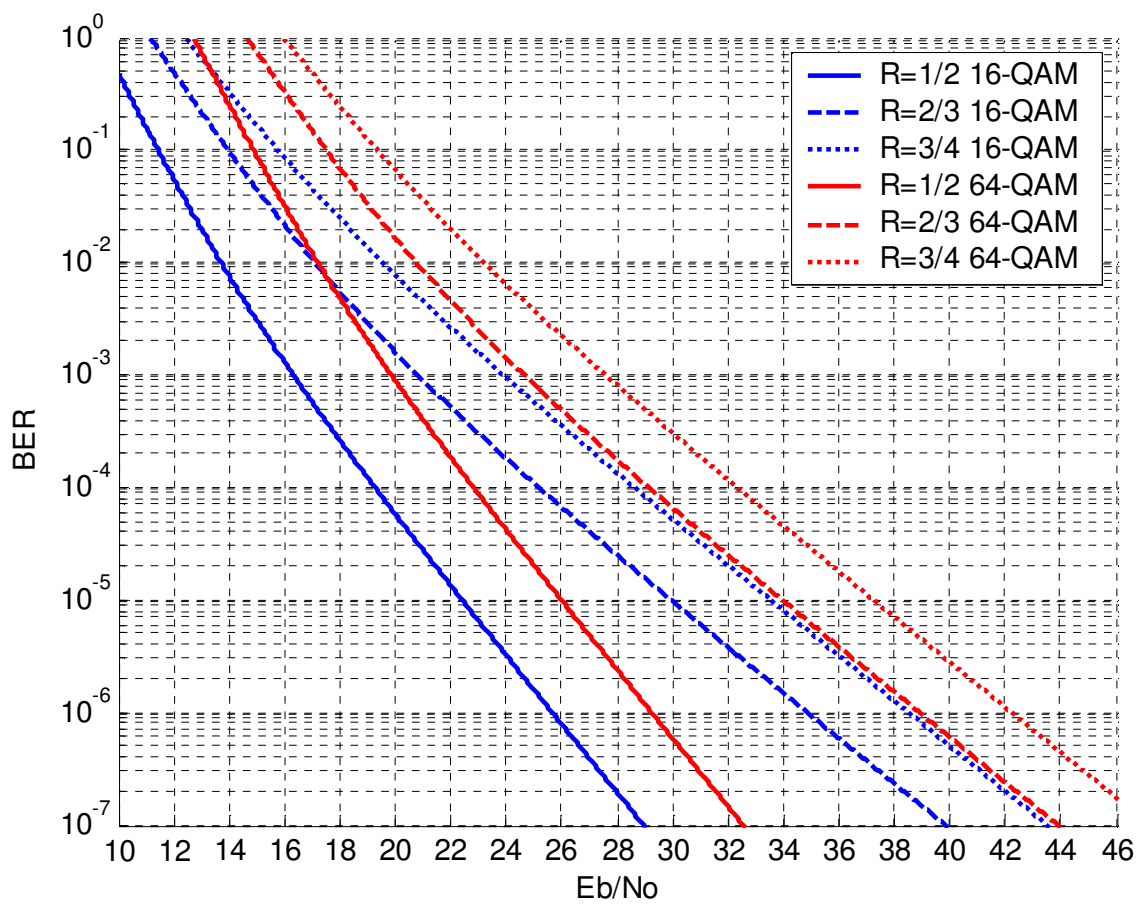


Fig.43 Performance of BICM-FLP with hard decoding in Rayleigh fading channels ($\kappa = 3$, 16,64 QAM).

References

- [1] G. Ungerboeck, "Channel coding with multilevel/phase signals," *IEEE Transactions on Information Theory*, vol. IT-28, pp. 56–67, Jan. 1982.
- [2] D. Divsalar, M. Simon, "The design of trellis coded MPSK for fading channel: Performance criteria," *IEEE Transactions on Communications*, vol. 36, pp. 1004–1012, Sept. 1988.
- [3] E. Zehavi, "Eight-PSK trellis codes for a Rayleigh channel," *IEEE Transactions on Communications*, vol. 40, pp. 873–884, May 1992.
- [4] G. Caire, G. Taricco, E. Biglieri, "Bit-interleaved coded modulation," *IEEE Transactions on Information Theory*, vol. 44, pp. 927–945, May 1998.
- [5] S.X. Ng, T.H. Liew, L.L. Yang, L. Hanzo, "Comparative study of TCM, TTCM, BICM and BICM-ID schemes," *IEEE Vehicular Technology Conference*, vol. 4, pp. 2450-2454, May 2001.
- [6] C.S. Lee, S.X. Ng, L. Piazzo, L. Hanzo, "TCM, TTCM, BICM and iterative BICM assisted OFDM-based digital video broadcasting to mobile receivers," *IEEE Vehicular Technology Conference*, vol.1, pp.732-736, May 2001.
- [7] A. Chindapol, J.A. Ritcey, "Design, analysis, and performance evaluation for BICM-ID with square QAM constellations in Rayleigh fading channels," *IEEE Journal on Selected Areas in Communications*, vol. 19, pp. 944-957, May 2001.
- [8] Li Xiaogdong, J.A. Ritcey, "Bit-interleaved coded modulation with iterative decoding using soft feedback," *Electronics Letters*, vol. 34, pp. 942-943, May 1998.
- [9] Li Xiaogdong, J.A. Ritcey, "Bit-interleaved coded modulation with iterative decoding," *IEEE International Conference on Communications*, vol. 2, pp. 858 – 863, June 1999.
- [10] Yih Chi-Hsiao, E. Geraniotis, "Performance optimization of bit-interleaved

- coded modulation with iterative decoding,” *MILCOM*, vol.1, pp. 737-742, Oct. 2002.
- [11] A. Chindapol, J.A. Ritcey, “Bit-interleaved coded modulation with signal space diversity in Rayleigh fading,” *Conference Record of the Thirty-Third Asilomar Conference on Signals, Systems, and Computers*, vol. 2, pp. 1003-1007, Oct. 1999.
- [12] H. Yuheng, J.A. Ritcey, “16-QAM BICM-ID in fading channels with imperfect channel state information,” *IEEE Transactions on Wireless Communications*, vol. 2, pp. 1000-1007, Sept. 2003.
- [13] J.S.K. Tee, D.P. Taylor, “A generalised performance bounding technique for bit interleaved coded modulation systems in the Rayleigh fading channel,” *IEEE International Conference on Communications*, vol. 3, pp. 1342 – 1346, April 2002.
- [14] J. B. Cain, G. C. Clark, J. M. Geist, “Punctured convolutional codes of rate $(n-1)/n$ and simplified maximum likelihood decoding,” *IEEE Transactions on Information Theory*, vol. IT-25, pp. 97–100, Jan. 1974.
- [15] J. Hagenauer, N. Seshadri, C.-E.W. Sundberg, “The performance of rate-compatible punctured convolutional codes for digital mobile radio,” *IEEE Transactions on Communications*, vol. 38, pp. 966 - 980, July 1990.
- [16] D. Haccoun, G. Begin, “High-rate punctured convolutional codes for Viterbi and sequential decoding,” *IEEE Transactions on Communications*, vol. 37, pp. 1113-1125, Nov. 1989.
- [17] E. Biglieri, D. Divsalar, P.J. McLane, M.K. Simon, *Introduction to Trellis-coded modulation with applications*. New York: Macmillan Publishing company, 1991.
- [18] E. Malkamaki, H. Leib, “Evaluating the performance of convolutional codes over block fading channels,” *IEEE Transactions on Information Theory*, vol. 45, pp. 1643 - 1646, July 1999.
- [19] S.B. Slimane, T. Le-Ngoc, “Tight bounds on the error probability of coded modulation schemes in Rayleigh fading channels,” *IEEE Transactions on Vehicular*

Technology, vol. 44, pp. 121-130, Feb. 1995.

[20] C. Tellambura, "Evaluation of the exact union bound for trellis-coded modulations over fading channels," *IEEE Transactions on Communications*, vol. 44, pp.1693-1699, Dec. 1996.

[21] IEEE Std 802.11a-1999, *Part 11: Wireless LAN Medium Access Control (MAC) and Physical Layer (PHY) specifications: High-speed Physical Layer in the 5 GHz band*, Sept. 1999.

[22] IEEE Draft 802.11g, *Part 11: Wireless LAN Medium Access Control (MAC) and Physical Layer (PHY) specifications: Further Higher Data Rate Extension in the 2.4 GHz band*, Draft 8.2, Apr. 2003.

